Master's degree in Aerospace Engineering

Formation-Flying of Picosatellites using Differential Drag as a Control Methodology

Supervisor(s):
Prof. Fabrizio STESINA, Politecnico di Torino
Prof. Stefano SPERETTA, TU Delft

Candidate:
Simona CUNDARI

Politecnico di Torino

A.Y. 2023/2024

To the moon.

Acronyms / Abbreviations

ADCS Attitude Determination and Control System.

AFF Autonomous Formation-Flying.

AI Artificial Intelligence.

ARES Assessment of Risk Event Statistics.

AU Astronomical Unit.

CDMA Code Division Multiple Access.

COEs Classical Orbital Elements.

COTS Commertial Off-The-Shelf.

CPO Close Proximity Operations.

CROC Cross Section of Complex Bodies.

DOP Diluition of Position.

DRAMA Debris Risk Assessment and Mitigation Analysis.

ECEF Earth-Centered Earth-Fixed.

ECI Earth-Centered Inertial.

ESA European Space Agency.

FA Formulation Agreement.

FCA First Close Approach.

FDMA Frequency Division Multiple Access.

GNC Guidance Navigation and Control.

GNSS Global Navigation Satellite System.

GPS Global Positioning System.

HCW Hill, Clohessy and Wiltshire.

HIL Hardware-In-The-Loop.

HPOP Horizontal Dilution of Position.

IADC Inter-Agency Space Debris Coordination Committee.

LEO Low-Earth Orbit.

LLA Latitude Longitude Altitude.

LS Leap Seconds.

MIDAS MASTER-baased Impact Flux and Damage Assessment Software.

NMEA National Aeronautics and Space Administration.

NNSS Navy Navigation Satellite System.

OSCAR Orbital SpaceCraft Active Removal.

PNT Position, Navigation and Timing.

POD Precise Orbit Determiation.

PQ PocketQube.

RF Radio Frequency.

RIC Radial/In-Track/Cross-Track.

ROEs Relative Orbital Elements.

RTK Real Time Kinematics.

RTN Radial/Tangential/Normal.

SARA Re-entry Survival and Risk Analysis.

SNR Signal-to-Noise Ratio.

SSA Space Situational Awereness.

SSO Sun-Synchronous Orbit.

STK System Tool Kit.

STM State Transition Matrix.

TAI International Atomic Time.

TDMA Time Division Multiple Access.

TTFF Time to First Fix.

Tudat TU Delft Astrodynamics Toolbox.

UTC Coordinated Universal Time.

WGS World Geodetic System.

Acknowledgements

At the end of a journey, that has led me through these years, to all the people with whom I have grown and become the person I am today, I offer my deepest gratitude.

My most sincere thanks to Prof. Stefano Speretta, for having the patience to guide me through the writing of this thesis, and to Prof. Fabrizio Stesina, for making all this possible. Thank you to all the people at the Space Systems Department for welcoming and integrating me from day one.

My gratitude goes to my family, for always believing I could reach even the Moon, silencing my fears and insecurities, and especially to my sister Sarah, for leaving footprints for me to follow and for giving me the love I sometimes don't deserve. To my parents, I dedicate every single word of this work, for making sacrifices, and for giving me the chance to be here.
To the family I've found all over the world, to all the people I've met in this journey, I say thank you because from you I have learned more than any book could ever teach. For my family in Turin, and for the PoliTo Sailing Team, I reserve a special place in my heart.
To all the people that I've spent my adolescence with, to those who decide, day after day, to continue being part of my life, wherever it may lead. To those who are no longer here, but in a certain way will always exist.

Now I bid farewell to Turin, my city of peace, my adopted home, with an emptiness in my chest, in view of my upcoming departure. Now, that I've perhaps grown enough, that I am maybe more mature, Rome, I come to you.

Torino, July 25^{th}, 2024

Abstract

The rise of small satellites offers a cost-effective, faster, and more reliable alternative to traditional large satellites. They have made space missions more accessible, particularly for educational purposes, enabling more frequent launches and hands-on scientific experiments for students and researchers.
As space debris continues to pose a global challenge, the Inter-Agency Space Debris Coordination Committee (Inter-Agency Space Debris Coordination Committee (IADC)) published its Space Debris Mitigation Guidelines in 2002 to establish baseline technical standards. The introduction of smaller satellite systems has significantly impacted space traffic. Low Earth Orbit (Low-Earth Orbit (LEO)) has become increasingly crowded due to its higher accessibility, reflecting an exponential growth trend. Very small satellites present challenges in terms of Precise Orbit Determination (Precise Orbit Determiation (POD)), necessitating enhanced collision avoidance strategies.
The Delfi Program at Delft University of Technology focuses on demonstrating innovative small space technology developed in collaboration with both TU Delft and external partners in the space sector. The program has an educational purpose, preparing students for careers in the space industry by providing hands-on experience and training in cutting-edge space technologies.
This thesis builds upon a previous mission analysis, primarily focusing on demonstrating the formation of two satellites in LEO using differential drag to maintain their required relative distance. The new mission draws inspiration from the earlier Delfi-PQ mission, which re-entered the atmosphere in early 2024, continuing the concept of satellite formation. These satellites will be launched together as a single unit and then separated in orbit to function as two independent twin satellites.
The TU Delft Astrodynamics Toolbox (TU Delft Astrodynamics Toolbox (Tudat)) has facilitated the construction of the proposed scenarios, analyzing different phases of the mission, from detachment to in-orbit control, demonstrating the feasibility of Delfi-Twin in terms of Space Situational Awareness (Space Situational Awereness (SSA)). Investigations on the mission's lifetime have been fundamental in defining the final mission concept and understanding how differential drag control influences it.
The validation of an analytical method used to propagate the relative orbit of one satellite with respect to the other has also allowed for a comparison of two methodologies in terms of processing time, which impacts the mission's safety as well.
The last part of this work includes experimentation with a Global Navigation Satellite System

(Global Navigation Satellite System (GNSS)) receiver to assess the possible errors encountered when using an emulator for small satellites in LEO.
The overall research presented will help define not only the mechanical control system that will allow for the relative motion control of the twin satellites but can also serve as a basis for further analysis regarding strategies for Close Proximity Operations (Close Proximity Operations (CPO)).

Contents

List of Figures

List of Tables

Acronyms / Abbreviations

ADCS Attitude Determination and Control System.

AFF Autonomous Formation-Flying.

AI Artificial Intelligence.

ARES Assessment of Risk Event Statistics.

AU Astronomical Unit.

CDMA Code Division Multiple Access.

COEs Classical Orbital Elements.

COTS Commertial Off-The-Shelf.

CPO Close Proximity Operations.

CROC Cross Section of Complex Bodies.

DOP Diluition of Position.

DRAMA Debris Risk Assessment and Mitigation Analysis.

ECEF Earth-Centered Earth-Fixed.

ECI Earth-Centered Inertial.

ESA European Space Agency.

FA Formulation Agreement.

FCA First Close Approach.

FDMA Frequency Division Multiple Access.

GNC Guidance Navigation and Control.

GNSS Global Navigation Satellite System.

GPS Global Positioning System.

HCW Hill, Clohessy and Wiltshire.

HIL Hardware-In-The-Loop.

HPOP Horizontal Dilution of Position.

IADC Inter-Agency Space Debris Coordination Committee.

LEO Low-Earth Orbit.

LLA Latitude Longitude Altitude.

LS Leap Seconds.

MIDAS MASTER-baased Impact Flux and Damage Assessment Software.

NMEA National Aeronautics and Space Administration.

NNSS Navy Navigation Satellite System.

OSCAR Orbital SpaceCraft Active Removal.

PNT Position, Navigation and Timing.

POD Precise Orbit Determiation.

PQ PocketQube.

RF Radio Frequency.

RIC Radial/In-Track/Cross-Track.

ROEs Relative Orbital Elements.

RTK Real Time Kinematics.

RTN Radial/Tangential/Normal.

SARA Re-entry Survival and Risk Analysis.

SNR Signal-to-Noise Ratio.

SSA Space Situational Awereness.

SSO Sun-Synchronous Orbit.

STK System Tool Kit.

STM State Transition Matrix.

TAI International Atomic Time.

TDMA Time Division Multiple Access.

TTFF Time to First Fix.

Tudat TU Delft Astrodynamics Toolbox.

UTC Coordinated Universal Time.

WGS World Geodetic System.

Chapter 1

Introduction

The focus of this thesis is the analysis of the movement of satellites involved in the new space mission being developed in collaboration with Delft University of Technology. Building on the requirements previously defined in a mission analysis study and considering previous space missions of TU Delft, the movement of the two PocketQubes will be analyzed to demonstrate the feasibility of the mission as it has been defined.
In particular, this chapter presents a general introduction to the world of space miniaturization, followed by an introduction to the Delfi Project, providing an overview of the timeline and the high-level requirements.
At the end of this chapter, the outline of the thesis will be presented, briefly explaining the contents that will be discussed.

1.1 Pico-Satellites

1.1.1 Why that small?

When people think about space, it is common to visualize big rockets and giant spaceships. Nowadays, the rise of nanosatellites in the space industry changed, or better say, increased once again the differentiation that exists, and always will, in this particular market of science. It is, somehow, controversial, since society addresses "better" to "bigger": a bigger house, a bigger car, and so on. However, the space industry works in slightly different ways, always looking for cheaper, faster in time (which is still a huge variable in space missions), lighter, and more reliable solutions. Every kilogram in LEO, for example, costs thousands of dollars, a cost that thanks to the accomplishments of notable companies and the progress of technology decreased, but still, it's a significant investment.
Distances have shortened, daily supplies are more accessible, and time in general seems to pass faster. By defining smaller systems that will supposedly have those characteristics, the idea of an increasing number of launches for educational purposes and scientific experiments grows.

It is a fact that this "space fever" is making society feel closer to this world and, consequently, invest more money in a community that depends on it to survive and progress.

1.1.2 PocketQubes Standard

But how small are they? According to the State-of-the-Art of Small Spacecraft [4] these are generally classified as follows:

Type of Satellite	Total Spacecraft Mass (kg)
Minisatellites	100 – 180
Microsatellites	10-100
Nanosatellites	1 – 10
Picosatellites	1 – 0.01
Femtosatellites	0.01 – 0.09

Table 1.1 Satellite Classes and Mass Ranges

CubeSats, on the other hand, are defined as a common form of nanosatellites, based on a form factor of a 10 centimeters square cube, called unit (U). The CubeSat concept was developed after a collaboration between the Department of Aeronautics and Astronautics at Stanford University and the Aerospace Department at California State Polytechnic University in 1999 [5]. The first CubeSat was composed of a single unit (1U), nowadays these are usually combined to form 3U, 6U and so on.
Following a similar concept, PocketQubes were developed almost 10 years later, by the same Prof. Robert J. Twiggs who proposed the CubeSat idea in 1999. The first launched PocketQube was through the UniSat5 mission, from a collaboration within GAUSS s.r.l. and Morehead State University, marking a historic event in November, 13th 2013, boarding and then deploying four CubeSats and four PocketQubes, for the first time ever.
In 2018 Alba Orbital, Delft University of Technology, and GAUSS s.r.l., published the specifications with respect to this new class of spacecraft, stipulated to help universities in performing space applications using this type of classes [6]: picosatellite platforms based on a cubic-shaped form factor (approximately 50x50x50 mm per unit, (1P)) with each side one-half smaller than a CubeSat (100x100x100 mm per unit). Unlike the CubeSat standard, which specifies a deployment along the long-side edges, the PocketQube (PQ) uses a sliding backplate for ejection, thus one side of the platform has slightly different dimensions.

1.2 The Novel Mission

1.2.1 Delfi Program

The Delfi Program started in November 2004 at Delft University of Technology, as a technological demonstration of small innovative space technology within TU Delft itself and external partners in the space sector. The program aims to prepare students for careers in the space industry through hands-on educational experiences. Since its inception, TU Delft has successfully developed and launched three missions: Delfi-C^3 in 2008, Delfi-n3Xt in 2013, and Delfi-PQ in 2022 [7]. Delfi-PQ is notable for being the first PocketQube developed by TU Delft, positioning the university as a pioneer in this emerging market. Each Delfi project builds upon the achievements of its predecessors; thus, Delfi-PQ's objectives were informed by the successes of earlier satellite projects [8]. This iterative approach ensures that Delfi-PQ will play a critical role in shaping the goals and direction of future missions, such as Delfi-Twin.

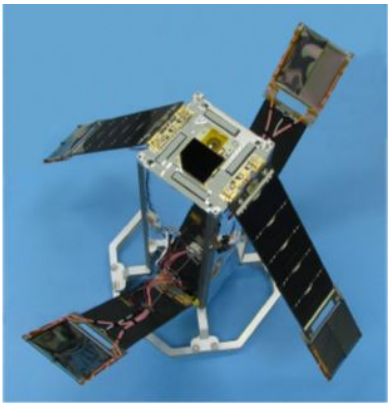

Fig. 1.1 Delfi-C^3

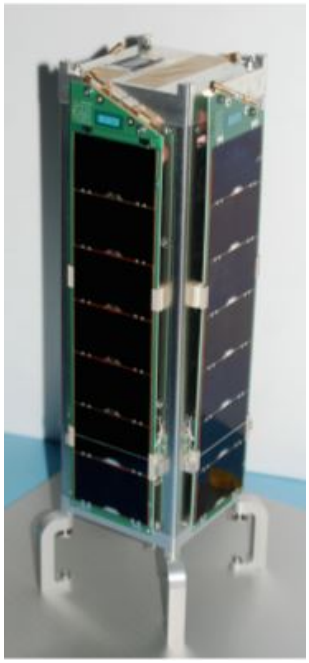

Fig. 1.2 Delfi-n3Xt

Fig. 1.3 Delfi-PQ

Fig. 1.4 Delfi Satellites

1.2.2 Delfi-Twin Mission Description

Mission planning is one of the key components in the development of a space mission, especially when involving complex systems like multiple spacecraft. Increased autonomy in mission planning can significantly reduce operational costs and enhance efficiency. Over the years, several solutions have been developed to address the challenges of mission planning. For example, the SPIKE scheduling system, designed for NASA's Hubble Space Telescope, has been used for

various missions since 1990 [9].
Small satellites have proven to be traceable in space, and a range of Guidance Navigation and Control (GNC) solutions have been developed to support their operations. These include orbit maintenance solutions, such as the PROBA series which is part of European Space Agency (ESA)'s In-orbit Technology Demonstration Programme. All these missions are dedicated to demonstrating innovative technologies [10]. Additionally, Proximity Operations (PO) for multiple spacecraft, such as those demonstrated by the PRISMA mission, show the capability of precise maneuvers and cooperative control between spacecrafts [11].
Effective mission planning also involves the integration of advanced algorithms and Artificial Intelligence (AI) to manage and optimize the scheduling of tasks, resource allocation, and conflict resolution among multiple satellites. This is increasingly important as the number of small satellite constellations grows, necessitating sophisticated coordination and communication strategies to maximize mission success and data collection efficiency. Furthermore, the adoption of modular and scalable software architectures allows for the rapid adaptation and customization of mission planning systems to meet specific mission requirements and objectives.

With the successful launch of the first PocketQube and the project's aim to advance cutting-edge space technologies, the new mission concept envisions a constellation of satellites engaged in Formation Flying. This novel mission developed at TU Delft is currently in the definition phase, and this thesis project will document the entire process of its creation from inception. By collaborating with various students and researchers, a new product will be conceptualized and developed.
The primary goal of systems engineering is to ensure that a system is designed, built, and operated to effectively achieve its objectives in the most cost-effective manner, taking into account performance, cost, schedule, and risk considerations. During Pre-Phase A, a wide range of mission concepts and alternatives are evaluated, leading to the selection of a viable mission architecture during Phase A. This phase includes defining program expectations, requirements, and constraints. Phase B focuses on advancing technology development, engineering prototyping, assessing heritage hardware and software, and conducting other risk-mitigation activities outlined in the project Formulation Agreement (FA). As a project progresses through its life cycle, delays in identifying and addressing issues become increasingly costly.
Since Sputnik 1 was launched by the Soviet Union in 1957, the number of satellites in orbit has increased rapidly, justifying an increased number of space debris. According to the ESA's Annual Space Environment Report [2] less than the 10% of the objects in space are active: the rest are debris. Space debris is, here, defined as all artificial objects including fragments and elements thereof, in Earth orbit or re-entering the atmosphere, that are non-functional, some of those, classified as unidentified objects as well. This newest report shows the evolution in all orbits of objects in space, as reported in Figure 1.6, distinguishing unidentified objects (UI), from rocket (R) and payload (P/PL) mission-related objects (M), fragmentation debris (F), debris (D), and bodies (B).

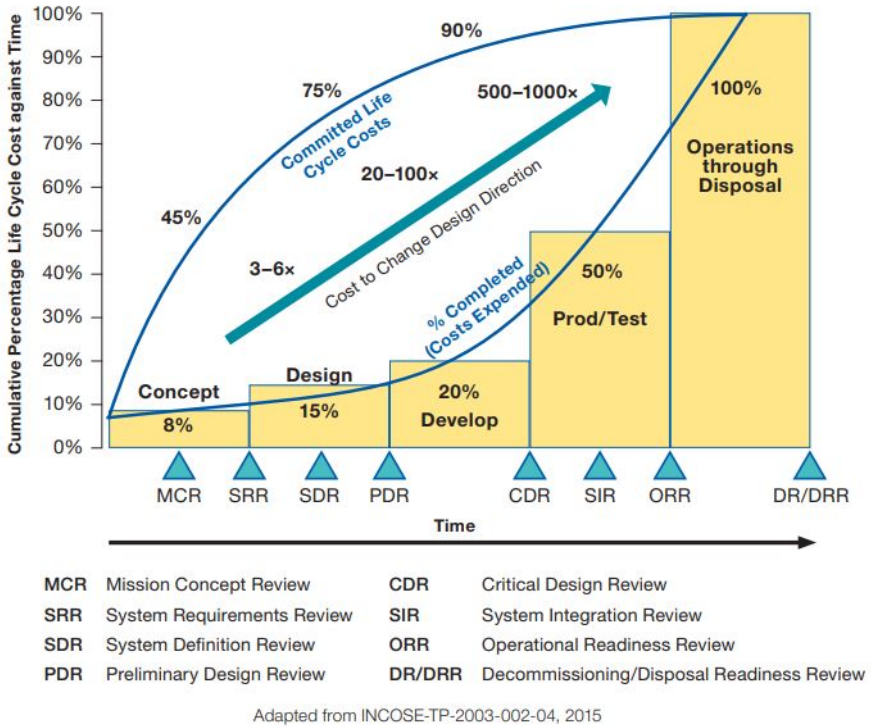

Fig. 1.5 Life-Cycle Cost Impacts from Early Phase Decision-Making [1]

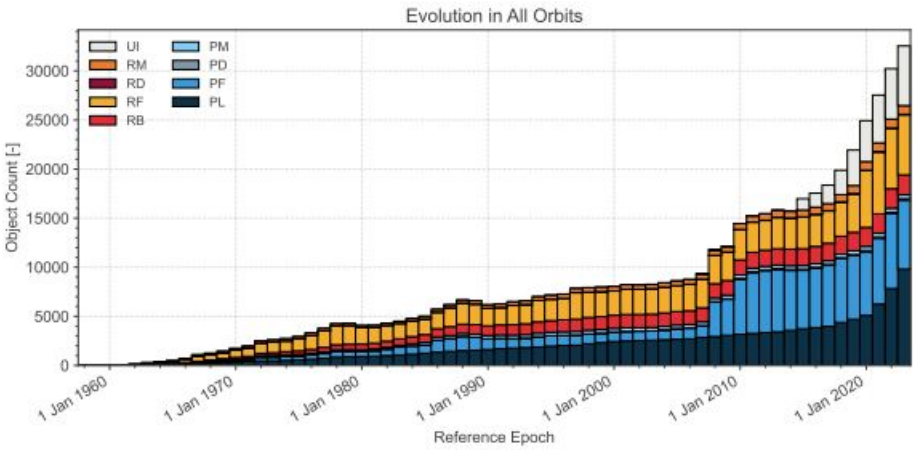

Fig. 1.6 Evolution of the number of objects in geocentric orbit by object class [2]

As space debris poses a problem on a global scale, in 2002 the Inter-Agency Debris Committee (IADC) published its Space Debris Mitigation Guidelines, as a baseline for the definition of technical standards. The new downsized systems also marked a notable change in space traffic. For its higher accessibility, LEO has the greater traffic density with almost 20 thousand objects registered until the end of 2022, marking an exponential trend over the years.
Very small satellites present Precise Orbit Determination (POD) issues, which increases the need for collision avoidance strategies. Indeed, in this thesis, a sensibility analysis is carried out in order to improve Space Situational Awareness (SSA), which, again, relies on the first main goal to fulfill.
Delfi-Twin began in early 2022, while Delfi-PQ was still operational in space, with a preliminary 0/A phase now already defined. Each subsequent step of Delfi-Twin's development will be based on the analyses and findings from these initial phases. Indeed, during the previous study, several critical needs were identified. As a result, feasibility studies were conducted, and specific mission requirements were established. These studies provided essential insights into the technical and operational aspects necessary for the successful implementation of the mission, ensuring that all defined requirements align with the overall mission objectives and constraints.
Moving towards Phase B in the space project life cycle signifies a transition to a more technical phase of development. By the end of this work, the baseline of the mission analysis will be defined. This includes confirming the technical solution, system architecture, and operational concepts, and ensuring their feasibility within the constraints of the mission. This phase involves detailed design and analysis, validating that the proposed solutions meet the mission's objectives, technical requirements, and budgetary limitations.
This phase specifically focuses on the orbital analysis of two satellites within the constellation. The characteristics of these satellites have been meticulously defined, encompassing everything from deployment and detachment strategies to the implementation of a sophisticated control methodology to manage them under differential drag conditions. This analysis is crucial for ensuring precise orbital positioning and operational efficiency throughout the mission.
So far, the main goals of the Delfi-Twin mission referenced throughout the development of this thesis comprehend:

- The demonstration of differential drag formation control.
- The demonstration of relative navigation for two spacecraft, specifically focusing on the precise orbit determination of both using GNSS receivers.

1.2.3 Mission Architecture and High-Level Requirements

This thesis follows a structured approach: as of early 2024, a final mission concept had not yet been established, but initial investigations into payload prototypes and their specific requirements were conducted. A significant focus will be placed on developing a miniaturized GNSS receiver, crucial for the experimental aspects detailed in the last Chapter 5. Notably, the satellites are

Configuration item	Category	ID	Requirements	Verification Method
Mission	Mission	MIS-100	The initial Relative Separation Velocity shall be equal to 10 cm/s.	RoD, A
Mission	Mission	MIS-110	The Drag Area shall be increased and decreased by a factor of two.	RoD, A
Mission	Mission	MIS-120	The Drag area Variation shall be managed by a control strategy that takes into account at least relative distance and velocity.	RoS, A
Mission	Mission	MIS-130	The satellite separation shall occur within the region of space bounded by a cone centered in one of the satellite centers of mass and with a maximum half-aperture angle of 52.7	RoD, A

Table 1.2 High-Level Mission System Requirements [3]

not planned to be equipped with a propulsion mechanism or an Attitude Determination and Control System (ADCS). Therefore, the primary method for controlling the satellites' position and velocity will involve adjusting their drag area.
Initial high-level requirements were defined during Phase 0-A. Table 1.2 outlines the technical system requirements that served as a foundational framework at the outset of this work. These requirements guided the construction of simulation scenarios, facilitated the analysis of critical aspects, and addressed issues identified during the mission definition study.

Every one of these mission requirements, regarding different phases, will be further analyzed throughout this work and used as a starting point in the definition of some crucial aspects of the mission scenario.

1.2.4 Mission time-line

As of 2024, different possible payloads to be carried out within the mission goals have been selected and a final mission concept defined. The different team members are currently working on a more detailed analysis regarding the satellites, together with the Delfi-PQ heritage, which re-entered the atmosphere in February 2024. Finally, the mission is expected to be launched no earlier than 2025.

1.3 Research Framework and Goals

The decision to treat this thesis sequentially rests on logical-structural and comprehensive reasons. As this is a work that follows a detailed study done previously, several references will be made in the course of the work. From now on, the objectives covered by this work will refer to the *TwinSat Mission*, developed by members of the Delfi team.

1.3.1 Differential Drag Formation Control

Delfi-PQ orbit has been considered as a starting point for the Twin-Sat mission definition. Two satellites, initially docked together, in a nominal 500 km range Sun-Synchronous near-circular orbit, are separated using a spring mechanism and controlled autonomously via differential drag. The initial mission and system design study was able to define the safest directions of separation and analyses for plausible values of relative separation velocities were carried out [3]. The direction of the release chosen guarantees a stable formation acquisition and a double control, relating a maximum distance for CPO and a maximum relative velocity, has been chosen to maximize the formation's lifetime.

Fig. 1.7 Graphical representation of the Differential Drag Control intending to show the relative movement of two satellites.

The aerodynamic force encountered in low orbit constitutes a valuable element only in terms of drag, acting in the opposite direction of the satellite movement. Here, the drag coefficient will be considered constant for the purpose of the work. However, parallel to this framework, studies will be conducted on the variation of this coefficient in a range of altitudes, thanks to the results of the control itself. J2 perturbations will be included as a second valuable parameter in the means of the formation control. Drag isn't here indeed considered a perturbation, but the deviation it causes from the initial Kepler orbit is instead used as the driver of the formation maintenance, using the mechanical movement of some panels.
One of the primary challenges in designing a control system utilizing atmospheric effects is

the real-time management of these panels, alongside the non-instantaneous response to motion induced by differential acceleration. In fact, the two satellites should maintain a maximum distance of 100 km to allow for an inter-satellite link to remain operational. The first aspect will be optimally addressed within the scope of this thesis. Furthermore, the detailed description of relative motion will be thoroughly explored, aligning closely with the objectives set forth in this thesis.

1.3.2 Relative Navigation for Small Satellites

Relative movement in a satellite formation flight is calculated following the mission requirements. A numerical method is used to calculate the absolute trajectory. It generally provides good accuracy, while having, on the contrary, a high computational load for the complexity of the dynamical models used can be a time-consuming process. The simulation starts with the detachment of the two satellites, using a spring-based separation system causing the satellites to drift apart. Using the drag control the drift is counterbalanced to re-group the satellites. At this point, differential drag is used to increase and decrease the separation and to continue the cycle maintaining within the maximum distance required for relative navigation assist to work.
An analytical model of the relative motion is less time-consuming than a numerical on-ground orbit reconstruction [12], being also necessary for autonomous in-orbit control.

1.3.3 Relative Navigation Emulator for Small Satellites

The primary mission goal is to demonstrate precise orbit determination for two spacecraft using GNSS, making accurate position measurements essential. The mission aims to establish the limits of achievable precision for small satellites utilizing commercial receivers, and it is expected to achieve high accuracy over multiple orbits.
Prior to this, various space-capable GNSS receivers that consume an acceptable amount of power relative to the total power available to the payloads were studied [3].
For the Delfi project, preference was given to Commertial Off-The-Shelf (COTS) receivers that have not yet flown to emphasize technology demonstration. The hardware will undergo testing, and the different types of errors generated will be analyzed and described.

1.4 Thesis Outline

The development of the thesis follows a temporal and logical flow, and its structure is briefly explained:

- **Chapter 2** deals with the fundamental concepts covered, from an introduction to Distributed Space Systems to the basics of Orbital Dynamics.
- **Chapter 3** introduces the tools for the performed simulations, with a focus on implementation and setup. Also, an insight into the definition of the mission concept is given, to better understand the requirements of such a mission.
- **Chapter 4** presents the simulations' results and evaluation of different aspects of the mission itself.
- **Chapter 5** is an overview of the experimental set-up for the tracking of the satellites using a GNSS signal emulator.
- **Chapter 6** will summarize the conclusion, with an overview of the total work, its future improvement, or recommendations for future analysis.

Chapter 2

Relative Navigation Basics

This chapter aims to briefly introduce all the fundamental concepts covered in this thesis. Since the mission at the center of this work is presented as a formation of multiple satellites, it will start from an overview of what is a Distributed Space System.
Then, a general overview of Cartesian Coordinate Systems and Reference Frames is given, moving with the basic notions of Orbital Dynamics necessary to understand what is pursued in this work.
To conclude, the Two-body Problem and notions about some of the orbital perturbations included in the model are presented here.

2.1 Distributed Space Systems

2.1.1 Formation-flying Guidance and Control

Distributed Space Systems usually comprehend multiple satellites working together to achieve a common goal, but depending on the scope of the mission different concepts are introduced:

- Rendezvous and Docking of spacecraft involves small distances and requires high control accuracy.
- Formation Flying spacecraft achieve their mission goals typically at distances of several to many kilometers.
- Constellations of spacecraft often fly at a distance of thousands of kilometers between individual spacecraft with low control accuracy demands.

Landsat 4 [13] was the very first civilian satellite to carry a spaceborne GPS receiver package and to use GPS signals to calculate its position. Nowadays satellites uses the Global Positioning

System (GPS) system (or other equivalent systems such as GLONASS, Galileo, BDS, etc...) for the determination of their positions and the stabilisation of their trajectory.

By definition, a spacecraft formation is a distributed space system where relative position and velocity are controlled in short distances in order to maintain these between preset boundaries. An Autonomous Formation-Flying (AFF) implies non-human interventions to compute a certain sequence of tasks. The formation geometry usually relies on Guidance, Navigation, and Control (GNC) functions:

- Relative Navigation: a model of the relative spacecraft dynamics is used for the estimation of the state.
- Guidance: based on the relative navigation results, spacecraft determines which path it should follow to reach a certain target.
- Control: The spacecraft generates and executes the actions needed to actuate the formation control actuators such as to comply with the guidance needs.

To demonstrate in-orbit tracking of small satellites in a formation requires some technical issues to be clarified. All satellites in order to be autonomous must be equipped with the necessary sensors, very small ones when using such small spacecraft. Studies on hardware components downsizing for nanosatellites and picosatellites are underway. Moreover, very small satellites present difficulties in POD and their uncertainty in the position becomes an issue for collision risks.

2.2 Reference Frames and Coordinate Systems

Earth-Centered Inertial Reference Frame

The Earth-Centered Inertial (ECI) Frame, or Cartesian Frame, is a frame having its origin at the center of the Earth. It commonly uses the vector (x, y, z), where:

- x_{ECI} is given by the intersection of the ecliptic with the equatorial plane during the Vernal equinox, thus the direction is such that, during the Vernal equinox the Earth sees the Sun in the Aries constellation.
- z_{ECI} is perpendicular to the equatorial plane with the direction toward the hemisphere that contains Polaris.
- y_{ECI} completes the right-handed triad.

The term "inertial" refers to a coordinate system non-rotating with the Earth, but fixed with respect to the stars.
The ECI Frame is used to describe the motion of satellites around the Earth.

Earth-Centered Earth-Fixed Reference Frame

The Earth-Centered Earth-Fixed (ECEF) Frame rotates with the Earth with respect to the stars, which makes it a non-inertial reference frame, rotating at an angular velocity equal to $\omega \approx 7.29218e5$ rad/s. The axes are defined as follows:

- x_{ECEF} points toward the Earth's prime meridian, lying in the equatorial plane.
- z_{ECEF} points toward the North Pole, being normal to the equatorial plane, overlapping with the z_{ECI}.
- y_{ECEF} completes the right-handed triad.

ECEF primary axis is always aligned with the Greenwich meridian as the principal direction, thus it's necessary to define an epoch: the J2000 will be the reference, based on the Earth position on January 1^{st} 2000 at 12:00:00.

Radial In-Track Cross-Track Coordinate System

When referring to a single satellite a coordinate system where the satellite itself is its center is often used. The Radial/In-Track/Cross-Track (RIC) Coordinate System is a local coordinate system used to describe the motion of one satellite with respect to the other, where:

- R points in the radial direction, which is from the center of the Earth (its central body) toward the satellite.
- I points in the general direction of the satellite's velocity vector but perpendicular to the radial axis (the velocity usually is not aligned with the radial axis).
- C completes the right-handed triad.

The RIC frame is here used when studying the satellite in close proximity, while the Hill, Clohessy and Wiltshire (HCW) equations describe their motion as a chaser and a target in two-body dynamics, under specific requirements to retrieve valid results (as it will be presented later in this chapter). In this thesis we will also refer to the RIC reference frame as the RSW reference frame.

2.3 Orbital Elements Definition

An orbit can be univocally described as a set of Classical Orbital Elements (COEs). A Kepler trajectory is defined by 6 parameters, where 4 of them are necessary in a two-dimensional problem (perifocal plane), and three of them describe the size, shape, and direction of the line

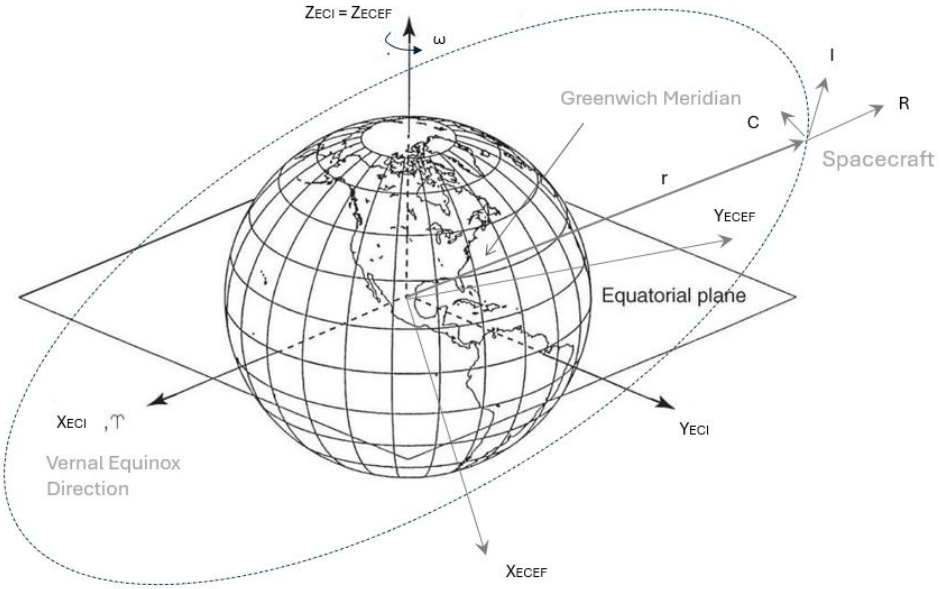

Fig. 2.1 ECI and ECEF Reference Frames. RIC Coordinate System.

of apses, while the fourth is required to pinpoint the spacecraft position along the orbit at a particular time. The remaining 2 parameters describe the orientation of the orbital plane.

- *Semi-major axis (a)*: defines the size of the orbit.
- *Eccentricity (e)*: defines the shape of the conic.
- *Inclination (i)*: refers to the tilt of the orbital plane, so its orientation as the angle between the equatorial plane and the orbit plane, or as the angle between the North Pole (z-axis) and the normal to the orbital plane (direction of $\bar{h}$).
- *Right Ascension of Ascending Node (Ω)*: describes the location of the ascending node with respect to the x-axis in the ECI frame.
- *Argument of Perigee (ω)*: is the angle between the ascending node and the direction of perigee given by the eccentricity vector.
- *True Anomaly at Epoch (ν)*: the angle, in the plane of the spacecraft's orbit, between the perigee, the eccentricity vector, and the position vector of the satellite at a particular time, called "epoch".

To sum up, the position and the velocity vectors at a certain time completely describe the two-body orbit, since they can be converted into six orbit elements, and similarly, if the orbital elements are given, there are corresponding position and velocity vectors at a specified time.

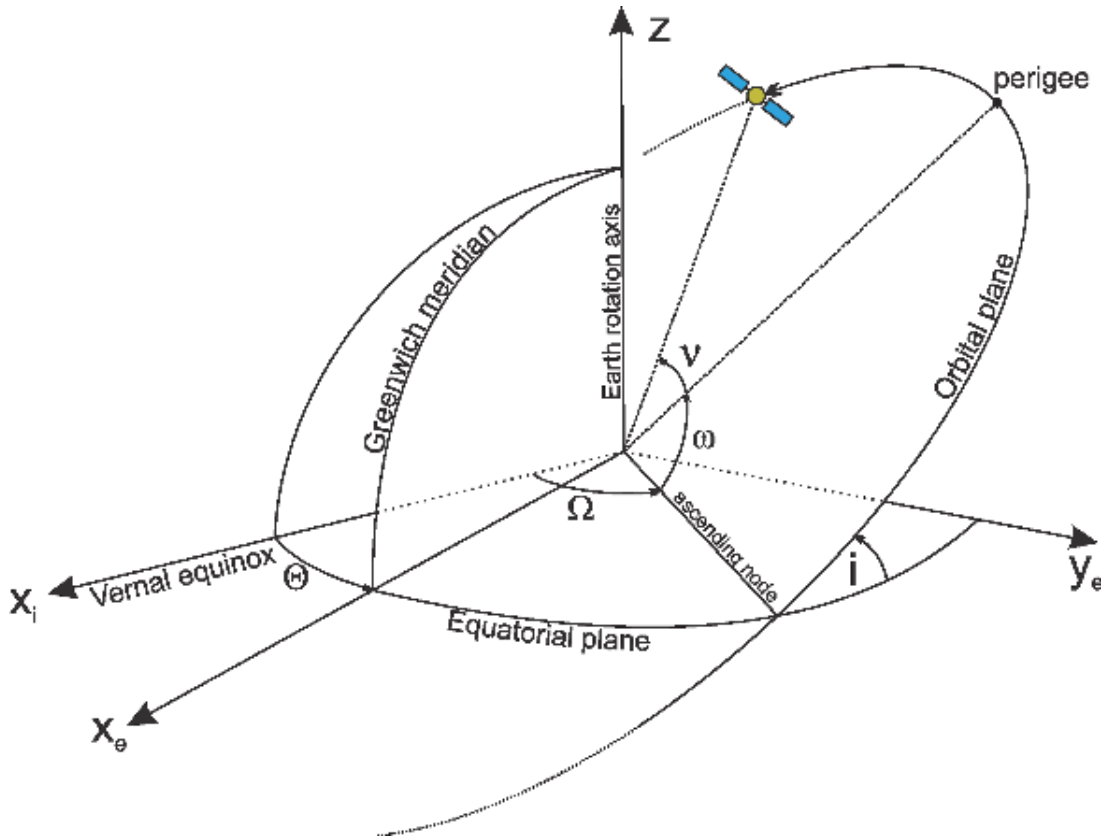

Fig. 2.2 Kepler Orbital Elements in the inertial frame IJK.

2.4 Motion in Space

2.4.1 The Two-body Problem

Kepler's laws are a description of the orbits but do not explain the planetary motion. The classic problem of the two bodies was solved by Newton, repeated later on for celestial bodies. The Two-Body Problem is used to describe the motion of two bodies in space under specific assumptions:

- The system is composed of two masses where one of the two (m) is much less than the main body (M).
- The two bodies are considered to have a spherical symmetry.
- No other forces are included other than the gravitational force acting on the bodies.

In our case, the secondary mass would be the artificial mass of the satellite orbiting around a central body, that is the Earth. The Universal Gravitation Law is used to express the forces acting on each mass so that the second law of dynamics can be used to describe the motion of

each mass, which by the subtraction of the two, leads to:

$$\ddot{\mathbf{r}} = -G\frac{m+M}{r^3}\mathbf{r} \tag{2.1}$$

By defining a gravitational parameter $\mu = GM$, and noting that $(m+M) \approx M$, the equation of the relative motion becomes:

$$\ddot{\mathbf{r}} + \frac{\mu}{r^3}\mathbf{r} = 0 \tag{2.2}$$

where r is the position vector obtained from the central body measured in the ECI frame.

2.4.2 Unperturbated Relative Motion

The parameterization of the absolute orbit in the ECI reference frame is expressed by a set of classical Keplerian Orbital elements $\alpha = (a, e, i, \omega, \Omega, u)$, where $u = M + \omega$ is the spacecraft mean argument of latitude.
The classical representation of the Keplerian orbital elements is modified to express the motion of the chaser with respect to the chaser avoiding also the singularities for near-circular orbits:

$$\delta\alpha = \begin{pmatrix} \delta a \\ \delta\lambda \\ \delta e_x \\ \delta e_y \\ \delta i_x \\ \delta i_y \end{pmatrix} = \begin{pmatrix} (a_c - a_t)/a \\ (u_c - u_t) + (\Omega_d - \Omega_t)cos(i_t) \\ e_{x_d} - e_{x_t} \\ e_{y_d} - e_{y_t} \\ i_c - i_t \\ (\Omega_d - \Omega_t)sin(i_t) \end{pmatrix} \tag{2.3}$$

where the subscript c indicates the chaser's orbit and t the target one. Apart from the relative semi-major axis δa and the relative mean longitude $\delta\lambda$, the other components constitute the relative eccentricity and inclination vectors whose Cartesian and polar notations are:

$$\delta\mathbf{e} = \begin{pmatrix} \delta e_x \\ \delta e_y \end{pmatrix} = \delta e \begin{pmatrix} cos\phi \\ sin\phi \end{pmatrix} \tag{2.4}$$

$$\delta\mathbf{i} = \begin{pmatrix} \delta i_x \\ \delta i_y \end{pmatrix} = \delta i \begin{pmatrix} cos\theta \\ sin\theta \end{pmatrix} \tag{2.5}$$

i.e. determined by the relative perigee ϕ and the relative ascending node θ.
The absolute orbit motion about a central body is usually described using the Cartesian coordinates state vector $\mathbf{x} = (r_x, r_y, r_z, v_x, v_y, v_z)$, which contains the position and velocity of the spacecraft in the ECI frame. Similarly, the relative motion can be expressed using the Hill

coordinates as:

$$\delta \mathbf{x} = \begin{pmatrix} \delta r_r \\ \delta r_t \\ \delta r_n \\ \delta v_r \\ \delta v_t \\ \delta v_n \end{pmatrix} = \begin{pmatrix} \Delta \mathbf{r} \cdot \mathbf{o}_r \\ \Delta \mathbf{r} \cdot \mathbf{o}_t \\ \Delta \mathbf{r} \cdot \mathbf{o}_n \\ \Delta \mathbf{v} \cdot \mathbf{o}_r + \Delta \mathbf{r} \cdot \dot{\mathbf{o}}_r \\ \Delta \mathbf{v} \cdot \mathbf{o}_t + \Delta \mathbf{r} \cdot \dot{\mathbf{o}}_t \\ \Delta \mathbf{v} \cdot \mathbf{o}_n + \Delta \mathbf{r} \cdot \dot{\mathbf{o}}_n \end{pmatrix} \tag{2.6}$$

2.4.3 Relative Orbital Elements as C-W integration

One of the most used analytical processes for relative navigation relies on the HCW equations (Hill, 1878; Clohessy and Wiltshire, 1960). However, some assumptions need to be made in order to correctly implement it:

- The orbits must be fully Keplerian orbits
- The reference spacecraft must follow a circular or near-circular orbit
- The relative position vector magnitude must be small, compared to the reference satellite absolute position vector

The linearized unperturbed dynamics is described by these HCW equations and the introduced in the previous subsection and is formulated as follows:

$$a\delta\dot{\alpha} = Aa\delta\alpha + B\mathbf{f}_u \tag{2.7}$$

also referenced in 4.4, where:

$$A = \begin{bmatrix} 0 & 0 & 0 & 0 & 0 & 0 \\ -\frac{3}{2}n & 0 & 0 & 0 & 0 & 0 \\ 0 & 0 & 0 & 0 & 0 & 0 \\ 0 & 0 & 0 & 0 & 0 & 0 \\ 0 & 0 & 0 & 0 & 0 & 0 \\ 0 & 0 & 0 & 0 & 0 & 0 \end{bmatrix} \tag{2.8}$$

and

$$B = \begin{bmatrix} 0 & 2 & 0 \\ -2 & 0 & 0 \\ sin(u) & 2cos(u) & 0 \\ -cos(u) & 2sin(u) & 0 \\ 0 & 0 & cos(u) \\ 0 & 0 & sin(u) \end{bmatrix} \tag{2.9}$$

The motion is obtained through the State Transition Matrix (STM), which in the case of unperturbed orbits is as follows:

$$a\delta\alpha(t) = \Phi(t_0,t)a\delta\alpha_0 \tag{2.10}$$

The change between the ROE state and the Cartesian state is computed as:

$$\delta x = T(t)a\delta\alpha \tag{2.11}$$

where:

$$T(t) = \begin{bmatrix} 1 & 0 & -cos(nt) & -sin(nt) & 0 & 0 \\ 0 & 1 & 2sin(nt) & -2cos(nt) & 0 & 0 \\ 0 & 0 & 0 & 0 & sin(nt) & cos(nt) \\ 0 & 0 & nsin(nt) & -ncos(nt) & 0 & 0 \\ -(3n)/2 & 0 & 2ncos(nt) & 2nsin(nt) & 0 & 0 \\ 0 & 0 & 0 & 0 & ncos(nt) & nsin(nt) \end{bmatrix} \tag{2.12}$$

where, again position and velocity are expressed in the Radial/Tangential/Normal (RTN) frame.

2.5 Orbital Perturbations

2.5.1 Earth Oblateness J2 perturbation

The actual motion differs from what has been presented as C-W equations for unperturbed orbits. The deviation of the Earth's gravity field from radial symmetry under the assumption of a spherical central celestial body, causes additional, and non-perturbations, influencing especially a satellite formation in LEO. Referring to the J2 gravity term, Keplerian elements osculates causing periodic and secular variations. In this case, for close proximity, the short-periodic perturbations are canceled, leaving the satellites under long-periodic and secular changes of the relative orbital elements. The main effect is precisely caused by a second-order zonal coefficient J2. This means that the oblateness of the Earth causes a regression of the line of odes, a rotation of the line of apsides along with a change of the mean anomaly. Low-orbiting satellites, having short orbital periods, are not sensitive to longitudinal or tesseral variations because, being periodic, they do tend to average it to zero. On the other hand, high-orbiting satellites with long periods do not justify such an averaging assumption but are too high to be significantly influenced by what are, after all, very small effects. A geoid is defined as the ideal surface that, at any point, is perpendicular to the direction of the gravity force.

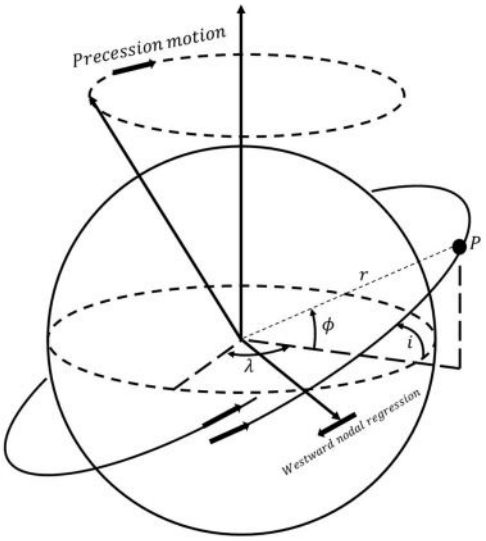

Fig. 2.3 Synthetic figure representing the regression of the line of nodes caused by the zonal harmonics for earth-orbiting spacecraft

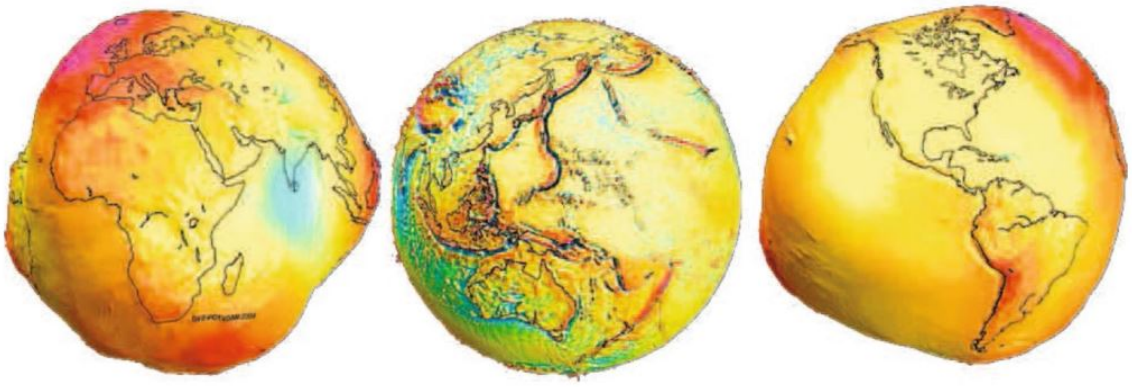

Fig. 2.4 The equipotential surfaces of the gravity field are not spherical but rather elliptical with several irregularities

2.5.2 Differential Drag and Solar Radiation Pressure

Low-orbiting satellites are also subject to differential forces caused mainly by differential drag. The differential terms is the result of differences in the ballistic coefficient $\frac{m}{C_D S}$ and the attitude motion of the spacecraft.
The effect of the atmosphere can be expressed as follows:

$$a_D = -\frac{1}{2}\rho \frac{SC_D}{m} V_r^2 \tag{2.13}$$

A study that directly implies this coefficient will be presented in chapter 3: the orbital lifetime depends on it, directly influencing the mission architecture definition. In fact, the higher this value is, the longer the objects are going to exist in orbit.
While the atmospheric lift component is perpendicular to the direction of the relative velocity and judged irrelevant for the case, the atmospheric drag component exists along the direction of the velocity component and in this mission used as a control strategy to maintain the satellites in an autonomous formation-flying, with the difficulties accounting to very small satellites.
In general, a perturbation is a force causing a deviation from the ideal Keplerian motion. Two major contributions have been presented, but a further analysis has been made to justify this choice.
Lastly, for a satellite orbiting this altitude the Sun causes disturbances in the form of electromagnetic radiation in the wavelength range of the entire electromagnetic spectrum, transferring a momentum, with a resulting effect averaged nearly to zero, but generally not confined to only variations in the eccentricity and semi-major axis, as for the aerodynamic drag. The solar pressure is experienced as a radiation pressure on the effective surface:

$$p_S = \frac{I_S}{c} = 4.510^{-6} Pa \tag{2.14}$$

where $I_S = 1361 W/m^2$ is the mean solar constant intensity observed at a distance of 1 Astronomical Unit (AU), measured on a surface perpendicular to the rays, and c refers to the speed of light.

2.5.3 Gravitational Perturbation: Third-Body Effect

The simplification of the Two-Body Problem is such that the only gravitational forces included are coming from the bodies considered. the perturbation caused by the presence of third bodies depends on the distance of the latter. The three-body problem describes the motion of three-point mass particles under their mutual gravitational interactions. An instance of such a situation is the motion of the Moon about the Earth under the influence of the Sun. However, this problem does not have a general solution and thus we usually consider simplified formulations justified

by physical reasoning.
In the consideration of a three-body system, the attraction forces are, by definition:

- Satellite - Main body
- Satellite - Perturbated body
- Main body - Perturbated body

Defining the distance from the main body to the orbiting satellite ar $r = \rho_0 - R_0$, where ρ_0 and R_0 are, respectively, the distances from an inertial frame to the satellite and the main body, it is possible to write the equilibrium forces as:

$$\begin{cases} m\ddot{\bar{\rho}}_0 = -G\frac{Mm}{r^3}\bar{r} - G\frac{M_p m}{\rho^3}\bar{\rho} \\ M\ddot{\bar{R}}_0 = -G\frac{Mm}{r^3}\bar{r} - G\frac{M_p m}{\rho^3}\bar{\rho} \end{cases} \tag{2.15}$$

The net effect of this system is computed:

$$\ddot{\bar{r}} = -\frac{\mu}{r^3}\bar{r} - \frac{\mu_p}{\rho^3}\bar{\rho} + \frac{\mu_p}{R^3}\bar{R} \tag{2.16}$$

and these last two terms are re-grouped into the perturbing acceleration a_p. Before defining the mission scenario, some of these perturbative accelerations are studied to assess their actual influence and determine which terms can be disregarded.

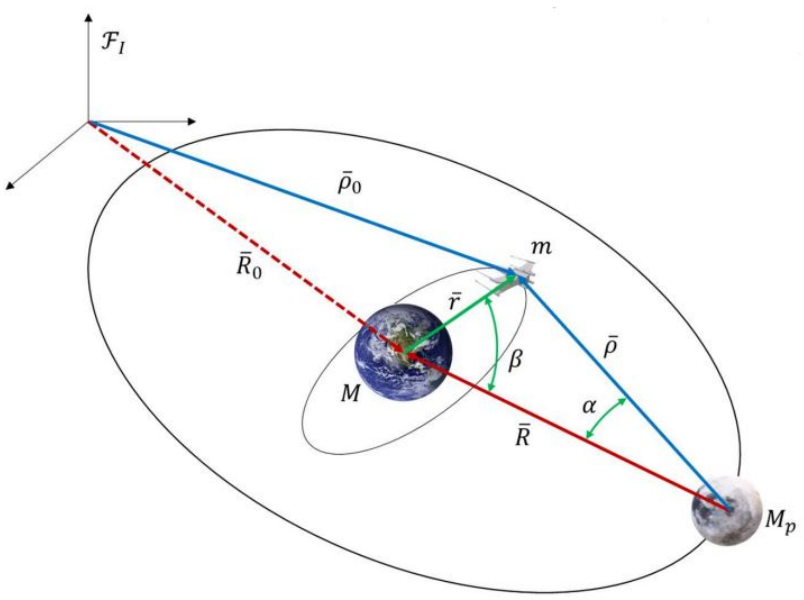

Fig. 2.5 Third body effect perturbations: a representation of a three-body system

Chapter 3

Mission Analysis

This chapter focuses on the mission concept of Twin-Sat. Starting with the description of the software implementation and the scenario defined, thus explaining what there is behind each segment and sequence. In particular, Tudat will be presented as the propagator used for this work.
Consequently, an insight into the geometrical configuration of the satellite will be discussed, as well as the choices that rely on the differential drag control methodologies. Along with it, the ESA's Debris Risk Assessment and Mitigation Analysis (DRAMA) tool is presented as an important instrument concerning both the cross-section calculation and the orbital lifetime.

3.1 Scenario Definition and Implementation

3.1.1 Mission Architecture Concept

As previously introduced the Twin-Sat Mission will comprehend multiple satellites, so far counted as a couple of two identical 3P PocketQubes, that will here be named *FirstQube* and *SecondQube*.
Each of the two won't be a proper chaser or target, but the lead will change according to the control actions given while chasing each other.
They're meant to stay not only within a safe zone while reaching each other, but also to maintain a maximum distance, thus staying in close proximity in order to fulfill relative navigation purposes.
The two spacecraft will contain their core buses and payloads, some of them still to be defined, and they will proceed in orbit for as much time as possible.

After splitting the single body at deployment into two orbiting bodies the satellites keep moving one with respect to the other, maintaining their distance always below a certain maximum value. At this point, they keep moving in a cyclic manner.

As a brief graphical recap, the following figure has the purpose of summing and further analyzing the mission concept developed throughout this work.

After the first detachment reaches the maximum distance set to 100 km, the satellites begin their cycle starting from an action on FirstQube. After the spring impulse is given, FirstQube will gain altitude while SecondQube will consequently lose altitude because of the direction of the impulse itself. In the previous phase of the mission, a double control was judged to be an improved and optimized strategy aiming to increase the lifetime of the bodies in orbit. Each phase within a control cycle is described as follows:

- Arc1. FirstQube's drag area is increased, continuously increasing the relative velocity of the satellite up to a value of 10 cm/s, which is exactly the value given by the spring impulse.
- Arc2. FirstQube's drag area is decreased again thus maintaining the satellite at the same relative velocity until they reach the minimum distance.
- Arc3. SecondQube's drag area is increased, generating again an increase of the absolute value of the relative velocity up to the stated value.
- Arc4. SecondQube's drag area is decreased again thus maintaining the satellite at the same relative velocity until they reach again the maximum distance set to be 100 km.

Software implementation and set up

The TU Delft Astrodynamics Toolbox (Tudat) is constructed as a set of libraries implemented in C++: a Python interface, called Tudatpy, has been used for the purpose of this thesis [14]. This was judged to be a more suitable propagator than the Ansys System Tool Kit (STK), thanks to its flexibility in creating multiple simulation scenarios. The simulation is written in a Python environment and propagated using Tudat modules.
The workflow presented in 3.2 shows how the mission is designed from the in-orbit injection of the satellites as a single-body, to the detachment into multi-body, to the differential drag control.

Launching the simulation: input modules

The simulation is created to be as flexible and interchangeable as possible. To be so, a set of modules is listed in main file to be launched as the control sequences work in a cyclic manner: each body increases and decreases its drag area computing like this all four control actions needed to complete one cycle.
The simulation ends at the specified ending epoch, saving the state and the dependent variable chosen. When launching the simulation it is also possible to decide the multiplication factor used for the differential drag control, given as an input for the simulation, together with the

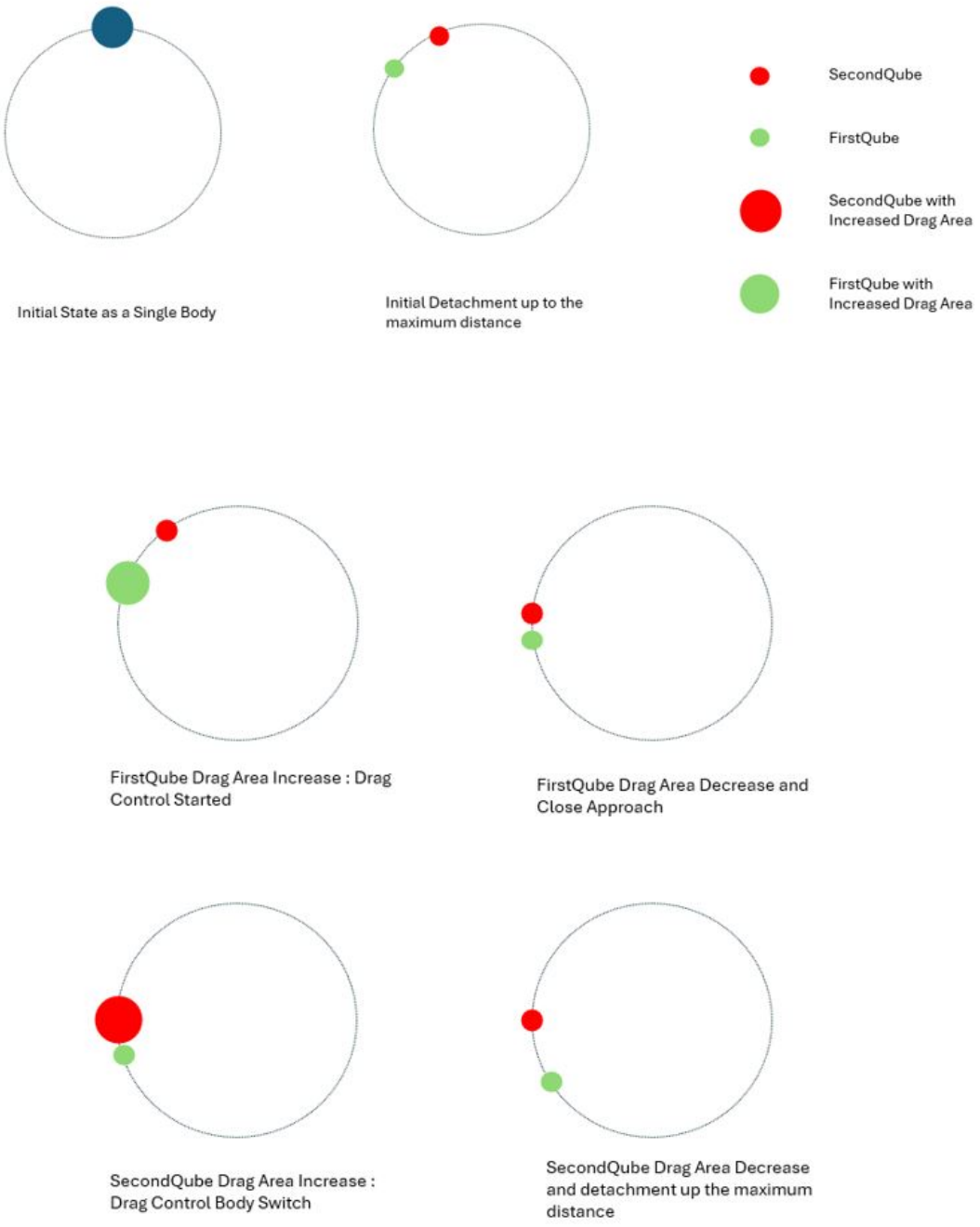

Fig. 3.1 Graphical representation of the mission concept, independent of time and not in scale, ideally showing the relative position of the satellites throughout each phase and control actions

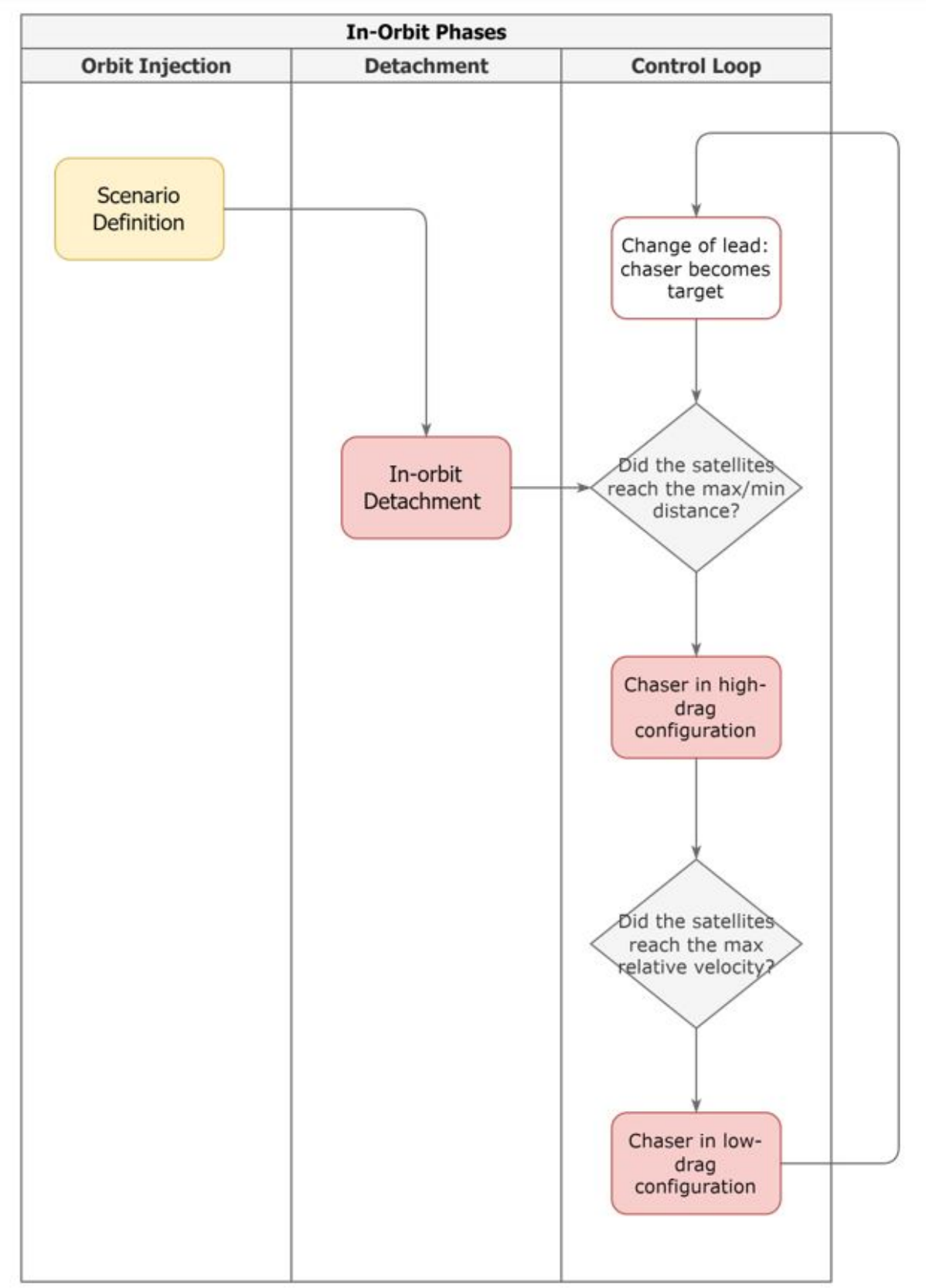

Fig. 3.2 Simulation workflow depicting the different phases within the mission concept.

initial and final time, and the step size used for the propagation.
The simulation starts a propagation for a period equal to two orbital periods with the bodies still existing as a single satellite, then proceeding with the detachment phase, causing the satellites to drift apart from one another.
The spring force is idealized as a directional impulse given in the velocity values: adding or subtracting in the state the velocity component values computed for an impulse magnitude of 0.05 m/s at the specified azimuth and elevation angles. A maximum distance is set to be the termination condition for this module, after which the control loop is started.
The modules are created as separate files reproducing the sequences of the mission concept, described in the previous section:

- Arc1 $\rightarrow$ *Sim_2Sat_IncreasedAreaSeq_body*1.*py*
- Arc2 $\rightarrow$ *Sim_2Sat_DecreasedAreaSeqCA_body*1.*py*
- Arc3 $\rightarrow$ *Sim_2Sat_IncreasedAreaSeq_body*2.*py*
- Arc4 $\rightarrow$ *Sim_2Sat_DecreasedAreaSeq_body*2.*py*

Every time one of these modules is launched, the environment is updated modifying the acceleration settings, directly depending on the aerodynamic coefficient settings of the case. Every one of these modules is initialized with the ending state of the previous module, ending at specified termination conditions: when the drag area of one body is increased the termination condition specifies the relative velocity to reach before decreasing the drag area again, then proceeding until the minimum or maximum distance specified is reached, considering an overshoot, dependently of the nature of the differential acceleration control and the promptness of the movement. These termination conditions have been created and inserted into a hybrid termination list: when a single condition is fulfilled, the phase reaches its final stage.

Simulation Environment Description and Initialization

The final stage of the orbit injection brings the satellites into a nominal sun-synchronous orbit and then causes a separation velocity of $0.1 m/s$ in the direction of separation considered optimal in terms of collision avoidance, for their First Close Approach (FCA). Ideally, a spring mechanism simulates two impulse maneuvers: a prograde and a retrograde burn, respectively, for FirstQube and SecondQube.
Each body is initialized together with the Earth to introduce J2 perturbations, while both the Sun and the Moon are introduced in the environment as point masses. In particular, an analysis regarding the perturbations to introduce into the model has been done and will be presented in the next chapter.
The simulation is set to use a global frame using the Earth in its center and J2000 model for its inertial orientation.

a [km]	**e** [-]	**i** [°]	**RAAN** [°]	ω [°]
6878.14	1.0×10^{-6}	97.4	0	0

Table 3.1 Initial Orbital Elements of the spacecraft

Mass [kg]	C_d [-]	**Drag Area** [m^2]
0.545	2.2	0.008

Table 3.2 Spacecraft characteristics

The equations of motion are integrated to predict the satellite's state over time in the J2000 global frame centering the Earth. The chosen numerical method uses the Runge-Kutta fixed-step integrator, with the higher-order (8th-order) of the two embedded propagators of the RKF7(8) method.

3.2 Cross-section evaluation and Satellite configuration model

3.2.1 DRAMA Tool

A spacecraft re-entering the atmosphere is a potential risk for human life on-ground [15]. The European Space Agency decided to write down its own rules regarding space debris mitigation, considering various aspects of the mission. It is stated that, before a launch, simulation with an ESA-approved software is mandatory.
These guidelines and standards stipulated aim to preserve the orbital environment and the project's current space assets. DRAMA contains a list of different software modules:

- Assessment of Risk Event Statistics (ARES). The *Assessment of Risk Event Statistics* tool provides information about a series of collision types of events between the spacecraft and other orbiting objects existing in space.
- MASTER-baased Impact Flux and Damage Assessment Software (MIDAS). The *MASTER-based Impact Flux and Damage Assessment Software* is used to model the collision flux and damage statistics within a mission.
- Orbital SpaceCraft Active Removal (OSCAR). The *Orbital SpaceCraft Active Removal* helps addressing disposal maneuvers at end-of-life (EOL) and calculating the orbital lifetime of one orbital body.
- Cross Section of Complex Bodies (CROC). The *Cross Section of Complex Bodies* is used to compute the cross-section of the orbital object.

- Re-entry Survival and Risk Analysis (SARA). The *Re-entry Survival and Risk analysis* is a combination of two tools for the re-entry in the Earth's atmosphere (SESAM) and the risk assessment on-ground of the same object (SERAM).

To proceed with an accurate analysis regarding, not only the value of the cross-sectional area of the satellites but also the validation of the number of factors chosen to create the differential drag control, the CROC tool was used, before proceeding with the specific calculation of the orbital life variation using OSCAR. Finally, the overall mission architecture was defined, by modifying one important detail introduced as an important mission aspect to further improve in the previous thesis work [3]. This aspect will be introduced soon, right after the cross-sectional analysis.

3.2.2 Satellite Model and Cross-Section Evaluation

CROC calculates the cross-section of a satellite with respect to defined aspect angles. The area calculated defines the surface to be taken into consideration when perturbations such as drag, solar radiation, albedo, etc, act on a body [15].
In this case, the goal was to calculate the area projected into the along-track direction to justify the lifetime of the satellite that uses aerodynamic drag as a control methodology, changing in fact his cross-section when a control action is called.
On CROC, the computation of the cross-section from a point of view is made by a composition of elements (such as spheres, boxes, cylinders, and cones) on a 3D Coordinate Space. The projected view of a drawn model is defined using the set of angles theta θ and phi ϕ that represents the direction from which the projection should be made, defining two different cases: a case in which the cross-section is calculated as a unique step being $\bar{R}$ parallel to $\bar{V}$, and a case in which these latter are not parallel and the cross-section is computed as the average of the areas for a set of cases defined as steps on the rotation of the satellite around the rotation axis. Figure 3.3 shows the defined view directions used.

As it can be seen from the *Component List* in the figure just mentioned, apart from a scratch of the model, the solar panels used for the control actions have been added to the proposed configuration: in the context of these analyses, just the solar panel used for the mechanical movement to introduce differential drag are inserted. In fact, the surface of the satellite will also contain solar panels, in order to improve its power generation of it. Figure 3.4 shows two configurations of the same satellite: the first one was chosen to be more efficient in terms of power generation, accepting a higher average cross-sectional area.

CROC has 3 different functionalities:

- F1. User-defined Aspect Angles
- F2. User-defined Aspect Angle and Rotation Axis

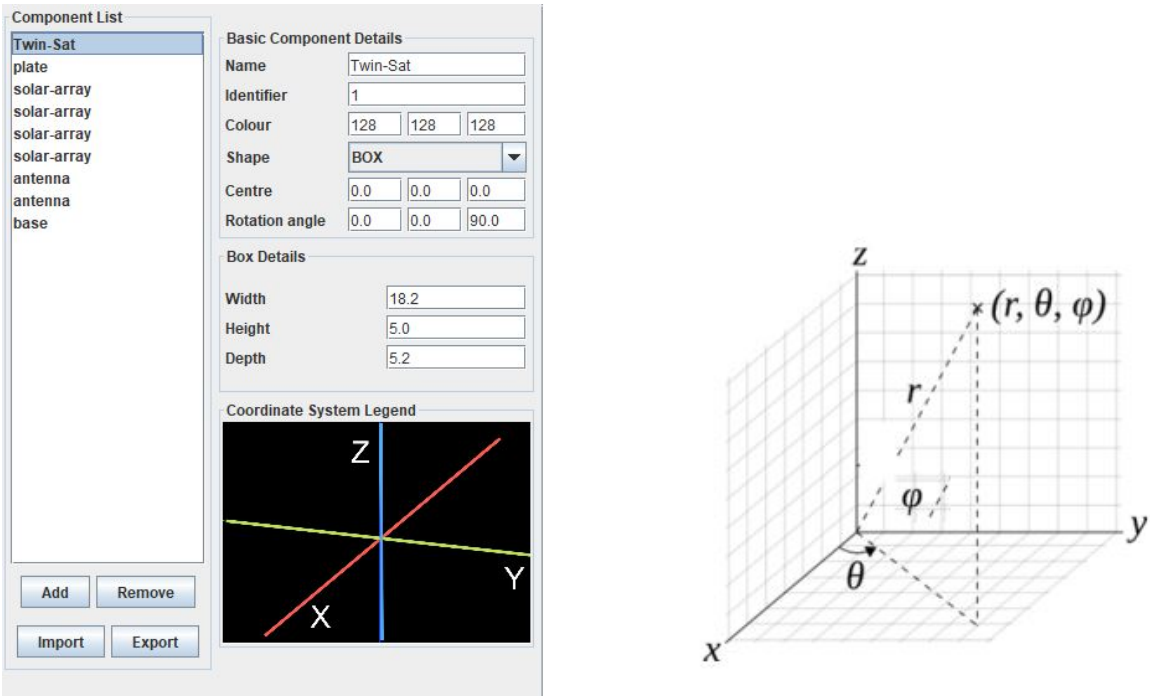

(a) CROC tool Settings

(b) Coordinate system

Fig. 3.3 Drama Settings and Coordinate System Legend

- F3. Randomly Tumbling Satellite

The average cross-section of a random tumbling satellite is based using some predefined points of view, equally speciated in a circumscribing sphere, then applying the computation defined in the basic case.
Figure 4.9 shows the results of the cross-sectional areas of these two cases. As expected there is an evident increase in this values, passing from an average of 118.04 cm^2 to an average of 203.25 cm^2.

However, to consider a randomly tumbling satellite means to overestimate its area, computing results that are far away from reality.
The satellite is considered to free tumble after the in-orbit injection when it still exists as a single-body. This study already considers two different bodies, whose control would make them drift from the direction of motion not more than a few degrees. The second step of this analysis was to compute these exact results, using another different functionality, under the assumption that the maximum drifting angle considered is 10 degrees. Finally, figure 4.9 is shown as proof of the reduced value introducing the angle constraint. During its motion, the satellite will stabilize and consequently adjust, causing random drifting from the direction of motion, so that the aspect angle is not more than the specified value, which again still brings to overestimated results, but in this case, valid within a safety factor.

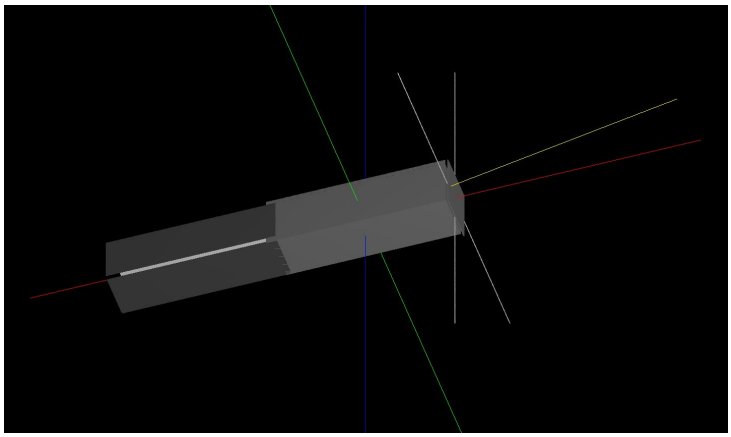

(a) Configuration 1. Twin-Sat pico-satellite.

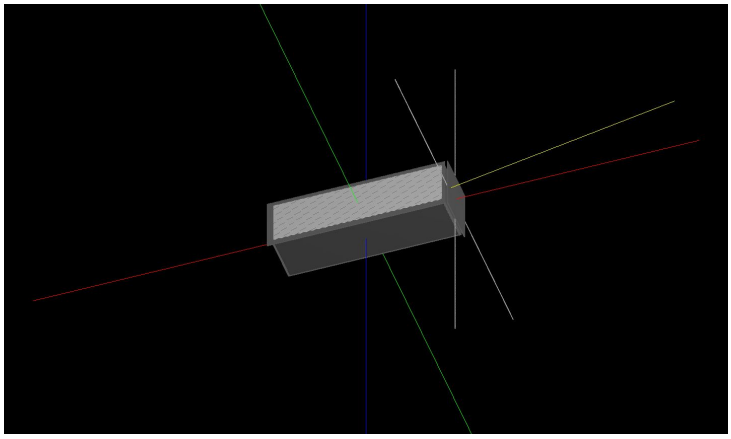

(b) Configuration 2. Twin-Sat pico-satellite.

Fig. 3.4 Twin-Sat different configurations studied, being Configuration 1 the optimized final design chosen for the mission.

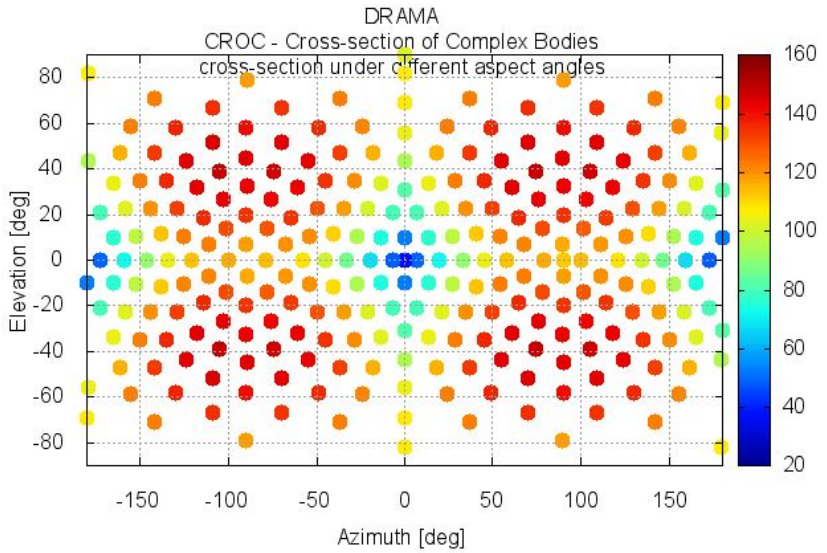

(a) Configuration 1. Twin-Sat pico-satellite.

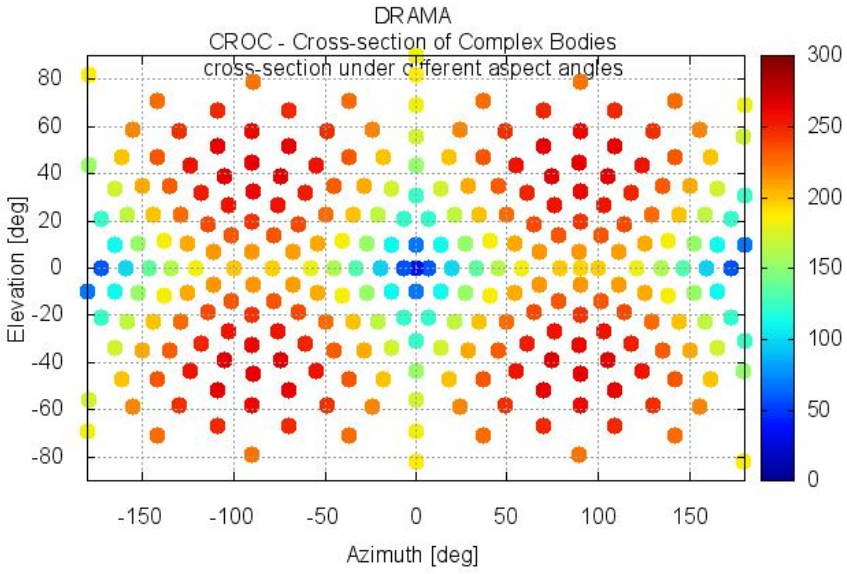

(b) Configuration 2. Twin-Sat pico-satellite.

Fig. 3.5 Cross-sections under different aspect angles for the two different configurations of a Twi-Sat pico-satellite

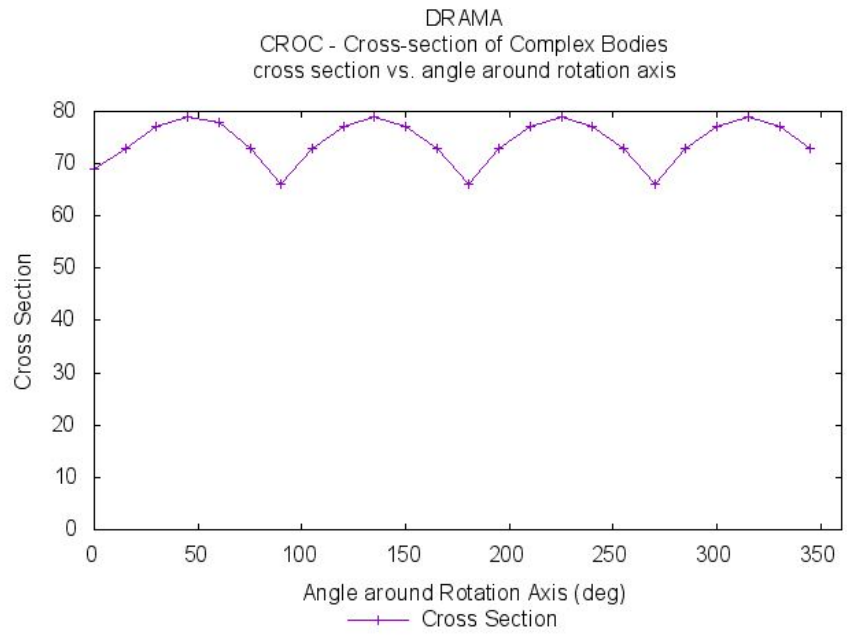

Fig. 3.6 Cross-sections vs. angle around rotation axis considering an aspect angle θ of 10 degrees.

3.2.3 Orbital Lifetime Variations

The OSCAR tool is here used to demonstrate a valid orbital lifetime for the mission. A first simulation out of a series considers the satellite in configuration 1 for the entire time of the mission, not considering the drag control, just to prove the value of the maximum in-orbit time that would spend such a satellite
Figure 3.7 shows these settings: the orbital elements used fit the initial conditions for the propagation and the description of the dynamics, taking into account Sun activity and geomagnetic predictions updated to the end of May 2024, and not considering any disposal options.

Again, this tool will be further used to justify the validity of the change made in the mission architecture and the control itself.
For an imperfection in the precision accuracy used by the software and the necessity to work with small numbers for the nature of the satellite itself, both the cross-sectional area and the mass were multiplied by a factor of 100, in order for the computation to not suffer of dangerous approximations.

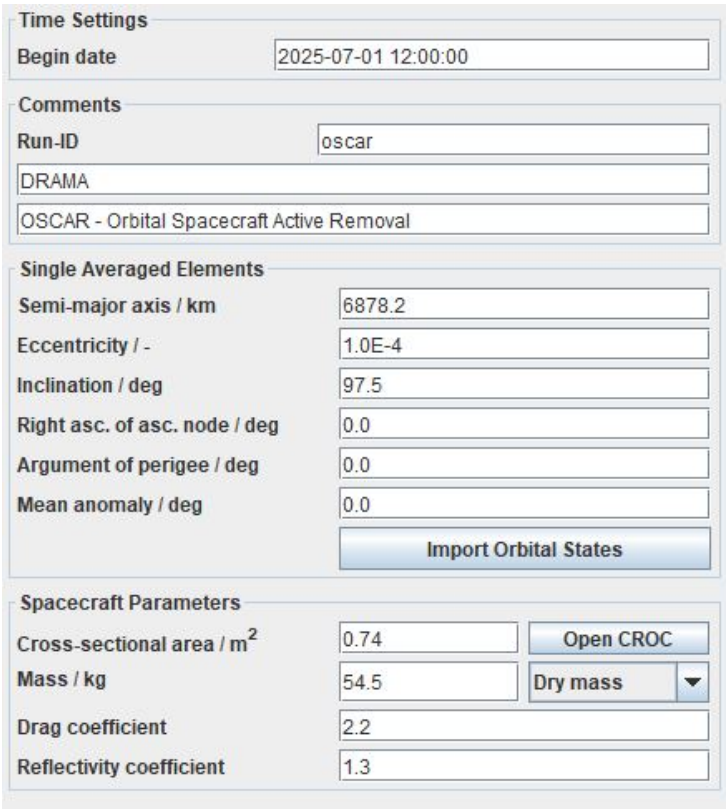

Fig. 3.7 DRAMA - OSCAR settings

Chapter 4

Simulation Results and Relative Motion Description Methodologies

This chapter aims to provide insight into the different phases of the mission.
Firstly, the optimal detachment point is studied using the basic orbital dynamics concepts. Secondly, the mission concept is defined and validated in terms of orbital lifetime and collision avoidance risks.
Throughout various simulations using DRAMA, a study of the multiplication factor used for the differential drag control is carried out to justify the final value and to define the limiting configuration and the limiting acceleration values defined by the relative velocity stopping condition used in the control.
Finally, the relative navigation model is presented: starting with a numerical validation using a test for the case, then inserting this model into the actual simulation environment.

4.1 Detachment Phase Solutions

4.1.1 Position and Direction of Detachment Analysis

The detachment phase was defined following the requirements in terms of impulse and direction of separation.
The detachment phase is modeled as a two-impulse maneuver given to both objects: prograde and retrograde burning assessed, respectively, to FirstQube and SecondQube. Performing a prograde thrust causes FirstQube (addressed as the current chaser) to move faster, which then gains altitude and starts falling behind the target (SecondQube). For that reason, it was necessary to avoid a hypothetical impact between the satellites in the short term. Basing the research on commercially available spring forces, a plausible value of 5 cm/s was given to both sides, for a detachment relative velocity of 10 cm/s as referenced in Chapter 1 [3], regulated also by the time the satellites need to reach the maximum distance after such an impulse.

An investigation using an epoch of 3 days, studying some possible angle combinations that guided the final decision for the mission architecture, was replicated to state such a requirement imposed. The satellites should be separated along the In-Track direction in order to avoid multiple collision risks at the beginning of the scenario. Secondly, since it has been decided to ensure at least 1 km distance for the first close approach (FCA), an iteration over combinations of Azimuth and Elevation angle spacing in the In-Track/Cross-Track and Radial/In-Track direction was carried out, finding that the satellite separation shall occur within the region of space bounded by a cone centered in one of the satellite's centers of mass and with a maximum half-aperture angle of 52.7 degrees. Since a pre-analysis was already made, one case has been taken as an example to justify the direction chosen, combining an azimuth angle of ca. 30 degrees with a vector containing an increasing value of the elevation angle. The angle with respect to the direction of motion was calculated using the following formula:

$$\theta = arcsin(\sqrt{sin(Az)^2 + sin(El)^2}) \tag{4.1}$$

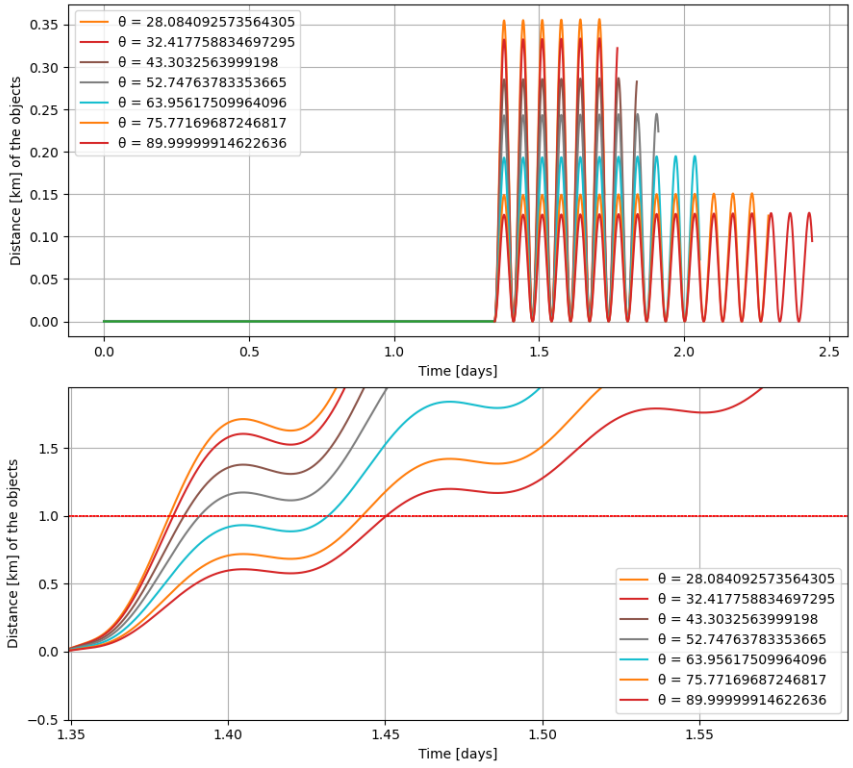

Fig. 4.1 Relative distance over an epoch of 3 days. Detachment after 1 orbit completed and zoom to highlight the points of minimum distance.

Due to orbital dynamics means, the orbital geometry is affected by the maneuvers in different ways depending to the orbital position of action.
It is important to conduct an analysis to understand how much it differ and which one is considered to be the optimal strategy to reduce the possibilities of a collision and increase the lifetime of the satellites in orbit. In order to do so, it was necessary to visualize the trend of

the orbital parameters in a certain time span (chosen to be 2 months), highlighting especially the time of detachment: in fact, after the first impulse the control exhibits repetitive behavior, recurring consistently at the same point in a cyclic manner.
A better insight into the orbital dynamics, presented in the form of the Gaussian equations, is given in order to guide the reader towards the final results of this analysis, proven in figure 4.2.

An impulse given in the direction tangent to the satellite trajectory at the apogee or at the perigee has effects on the geometry or the orbit in terms of semi-major axis and eccentricity:

$$\frac{da}{dt} = \frac{2a^2}{h}[esin(\nu)a_R + \frac{p}{r}a_T] \tag{4.2}$$

$$\frac{de}{dt} = \frac{p}{h}sin(\nu)a_R + [cos(\nu) + \frac{e + con(\nu)}{1 + ecos(\nu)}]a_T \tag{4.3}$$

A retrograde burn causes a loss of altitude if it happens near the perigee or a gain if near the apogee, and vice versa for the prograde burn. However, since the impulse is here given in a different direction than the pure along-track direction, every one of these cases will show combined effects due to both the tangential (a_T) and the radial (a_R) component of the spring mechanism.
In consideration to an orbit maintenance purpose, it is necessary to reduce combined effects, especially regarding the argument of perigee. In fact, a radial maneuver always causes a clockwise rotation if the impulse is given (positively) near the perigee, and a counterclockwise rotation if it is given near the perigee. Moreover, maneuvers far from the aspides cause the procession of the right ascension node as a secondary effect. The satellite position changes not only for its mean motion but also for how much those parameters vary.

$$\frac{d\omega}{dt} = \frac{1}{he}[-pcos(\nu)a_R + (p + r)sin(\nu)a_T] - \frac{d\Omega}{dt}cos(i) \tag{4.4}$$

Since the control mode switches the satellite lead from FirstQube to SecondQube sequentially, and since the spring-detachment is chosen to give a retrograde burn and a prograde burn, respectively, to SecondQube and FirstQube, in the respect of the orbital dynamics, valuable options for detachment are in an angle span of true anomaly of $[270 : 90]$ degrees (the other half of the circular angle span would be considered if the lead would be given to SecondQube first), for close-proximity to be maintained in certain requirements of relative velocity and to not diverge since the first actions.
An impulse given near the perigee not only reduces secondary effects but also reduces dangerously geometric configurations in terms of semi-major axis and eccentricity, which would cause unacceptable outputs, especially for the first close approach.
However, an analysis has been made to study the value of each close-approach and they were still judged unacceptable with the first simulation architecture under study. Instead of letting the satellites overlap, the control has been chosen to control both the maximum and the minimum distance, making the configuration safer in terms of collision avoidance.

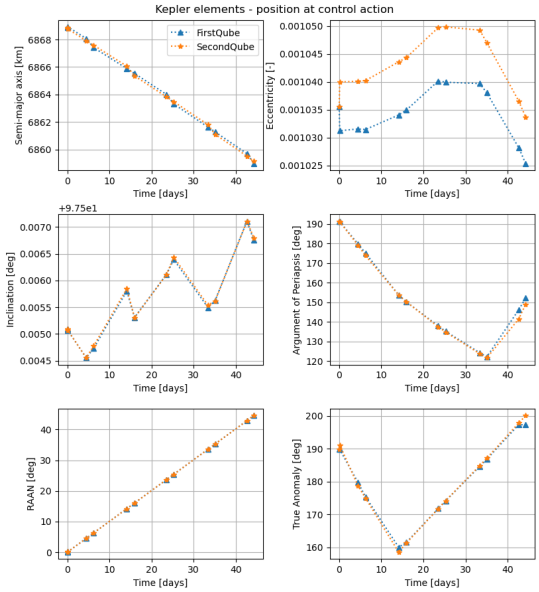

(a) Detachment at a true anomaly of 0 degrees (perigee)

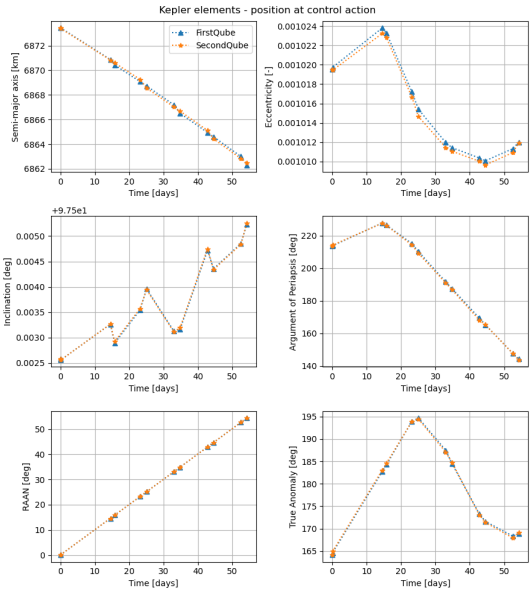

(b) Detachment at a true anomaly of 30 degrees

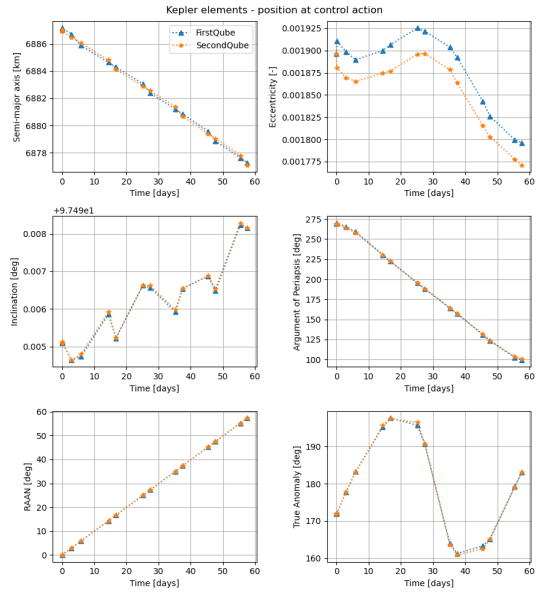

(c) Detachment at a true anomaly of 280 degrees

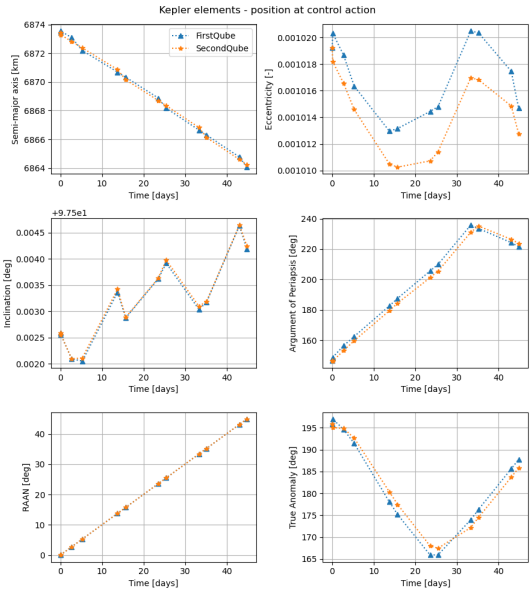

(d) Detachment at a true anomaly of 330 degrees

Fig. 4.2 Mean Kepler elements highlighting the position at each control action over a simulation epoch of a couple of months.

Figure 4.3 shows a zoom of the simulation detachment. Here, it is possible to see that the objects reach the maximum distance in less than one week, justifying in a way the choice of the spring impulse, given as a mission requirement.

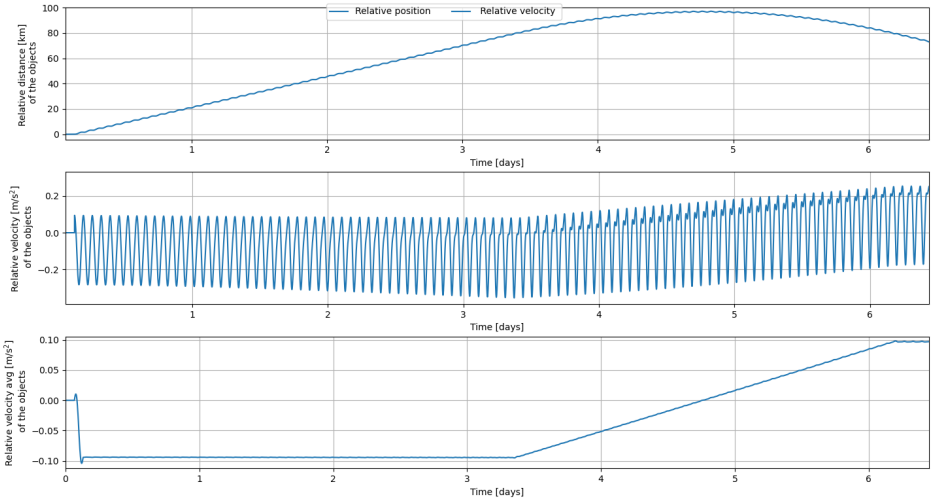

Fig. 4.3 Relative distance and velocity (also averaged with a moving average filter), over the complete simulation scenario of Twin-Sat.

Simulation results

Figure 4.4 shows the instantaneous variation of the semimajor-axis and the eccentricity of each of the two satellites, due to an impulse given at the perigee of the orbit when they are still together as a single body, after considering a certain time span of a couple of orbit. After this period, an impulse directed toward the most convenient direction (as it is explicitly explained in this chapter) is given to both bodies, and the differential drag control starts.

4.2 In-Orbit Control Solutions

4.2.1 Differential Drag Control: Control Actions

Since the satellites's control is not instantaneous due to the nature of a differential drag use, when reaching the maximum value set by the control, there is visible an overshoot depending on the value of the acceleration given, also depending on the multiplication factor. In this chapter a better insight is given regarding it: a minor value in the maximum distance is set in the control loop, thus considering this overshoot, maintaining the satellites in a close proximity zone within a margin. Figure 4.5 aims to highlight the moments of the control actions: the minimum and the maximum distance are set considering the overshoot, respectively under 100 km and above 0 km (since the overlap of the bodies is to avoid in this mission concept). These are the termination

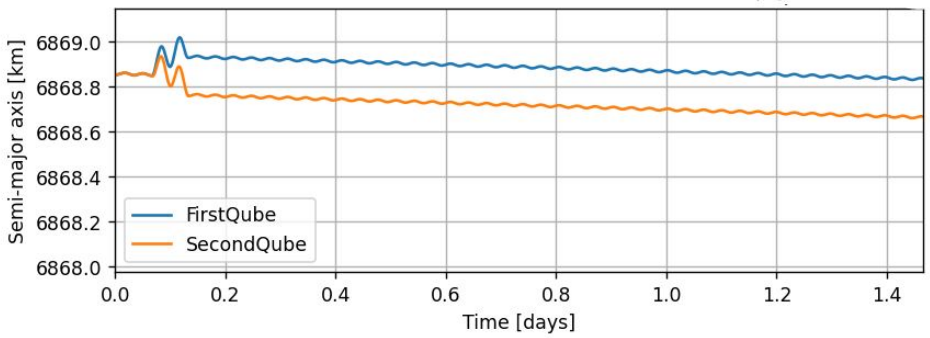

(a) Instantaneous change in the semi-major axes after detachment.

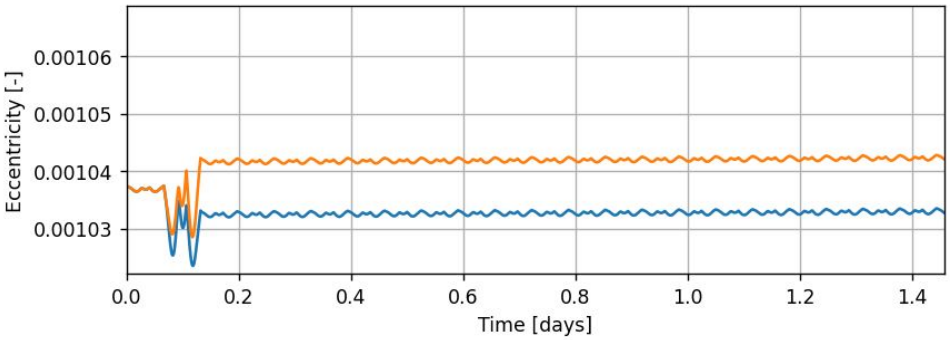

(b) Instantaneous change in the eccentricities after detachment.

Fig. 4.4 Semimajor axis and eccentricity trend before and after detachment, considering the averaged orbital parameters, by using a moving average filter.

conditions set after the second and fourth control action, hence switching at the end to the other body, starting with a termination condition made regarding the velocity.

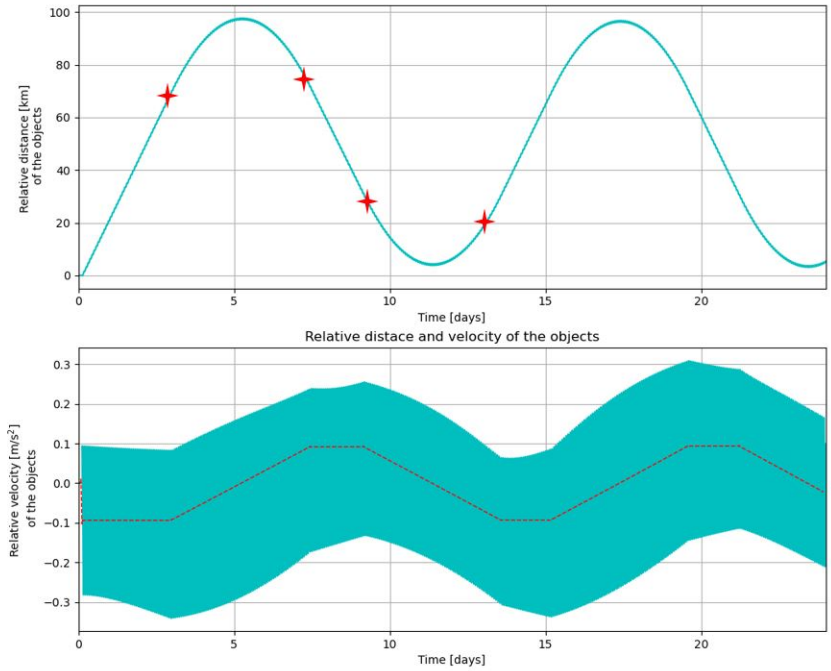

Fig. 4.5 Graphical representation of the mission phases description in terms of relative distance and relative velocity. The control actions are outlined by a red star, while the dotted line represents the average value of the relative velocity.

4.2.2 Differential Drag Control: Different Mission Concepts

The idealized description of the motion is obtained by assuming that only the gravitational forces exist, considering the bodies as spheres that are gravitationally equivalent to point masses, enabling the interpretation of the orbit as a simple geometrical figure. Numerical solutions to the perturbated equations of motion are now possible thanks to the increasing complexity of digital computers, that are able to solve complex differential equations with specific initial conditions. A satellite around the Earth experiences the gravitational attraction of the celestial bodies, such as the Sun, the Moon, and other bodies (which are not considered as their influence has been judged irrelevant for their distances and dimensions, as seen in Chapter 2). The nature of the Earth's oblateness is similar to the third-body effect which is the influence over the artificial body in orbit, corresponding to a secular variation in the satellite node, the argument of perigee, and mean anomaly. For such a reason, the orbital elements are subjected to periodic oscillations produced by the introduction of the J2 effect. The magnitude of relative accelerations for close near-circular formations has been analyzed. Figure 4.6 demonstrates the propagation of a body including multiple perturbing accelerations exerted by the central body as well as third bodies. This also justifies the choices made in defining the mission scenario. Here the Moon and the Sun are considered to be point masses because of the magnitude of the gravitational force that they

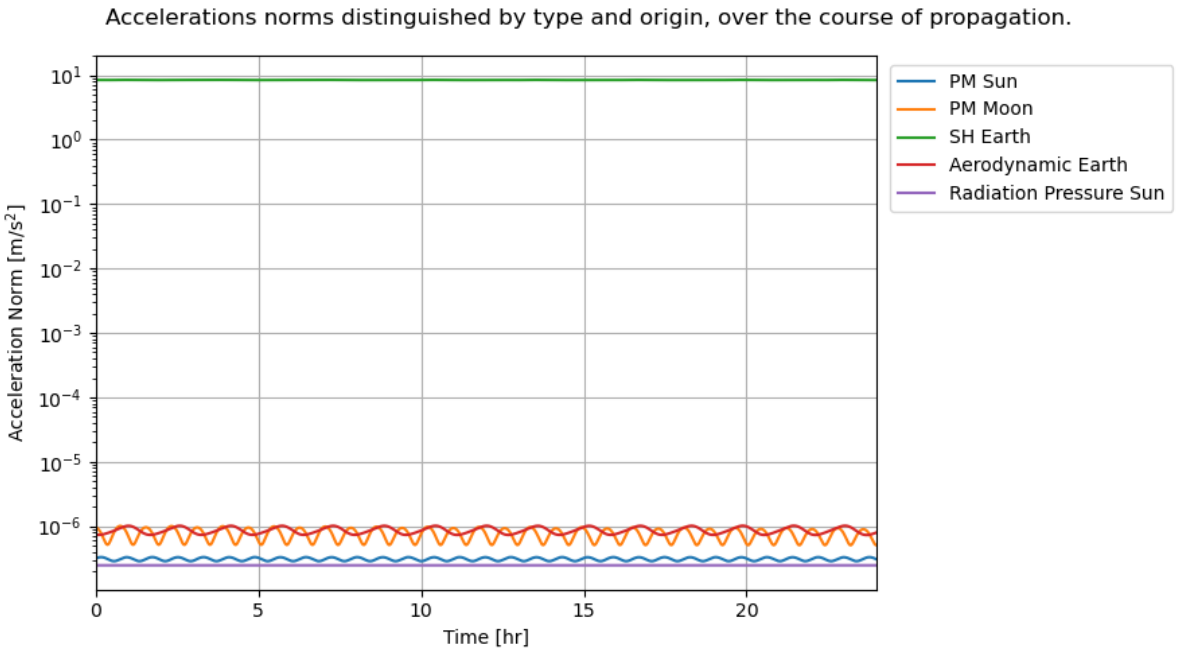

Fig. 4.6 Acceleration norms addressing the Earth, the Sun, and the Moon as point mass (PM), the spherical harmonic (SH) of the Earth, the aerodynamic contribution, and the solar pressure of the Sun on any orbiting satellites.

exert with respect to the one exerted by the Earth. The presence of other bodies is neglected, since irrelevant.
The ascending node and the argument of perigee exhibit significant linear variation, whereas the semi-major axis, the eccentricity, and the inclination do not.
As proof, the resultant orbital parameters for a simulation period of 24 days, thus containing two full cycles of the satellites approaching and drifting from one to the other are shown in figure 4.7.

As anticipated the mission concept was modified for collision avoidance risks. In fact, the first architecture studied the satellite proceeding in their motion until the maximum distance, without a stopping condition relative to the approach phase during conjunction. Instead, they would have proceeded to overlap during their motion until the maximum distance was reached again on the other side. In a previous study [3] it was evident that the relative distance decreased progressively.
Figure 4.8 gives an insight into these close approaches within the movement cycles of the bodies. The results of a previous mission design show the tendency of the satellite to reduce the minimum distance reducing its values until a collision, approximately every 3 cycles within a loop. To give a better overview of what happens in this case the simulation has been done considering a time span of at least three months. After one month the relative distance drops to almost zero, to later re-drop after a first detachment from the unsafe zone. Clearly, this tendency is very risky and judged unacceptable.

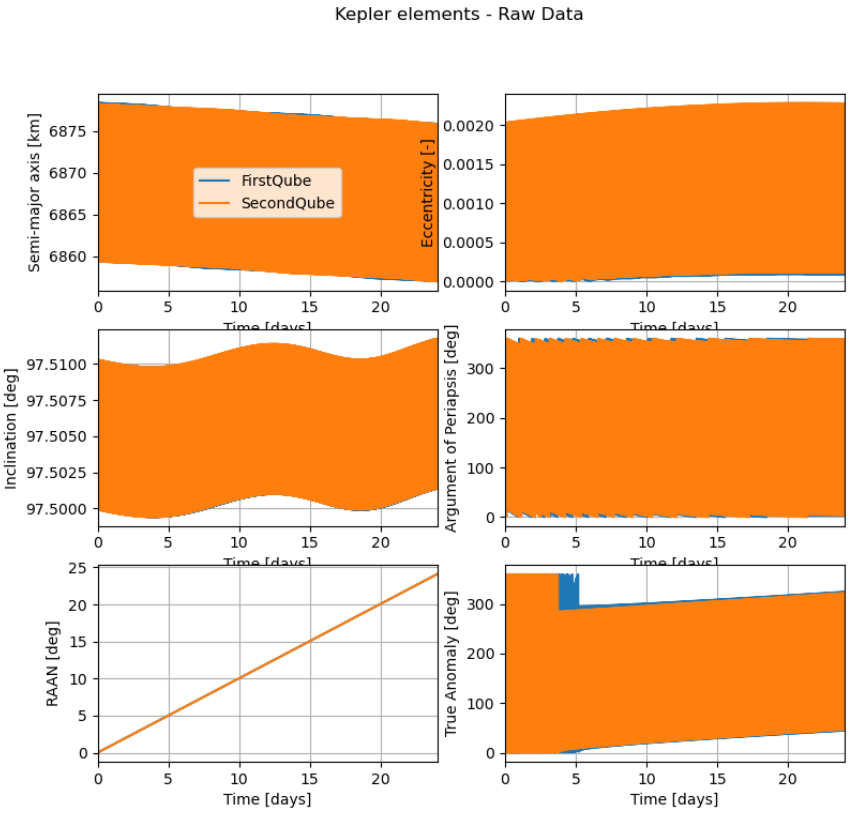

(a) Orbital elements variations produced for a simulation period of 24 days, containing 2 full cycles of the satellites, from detachment to the second close approach.

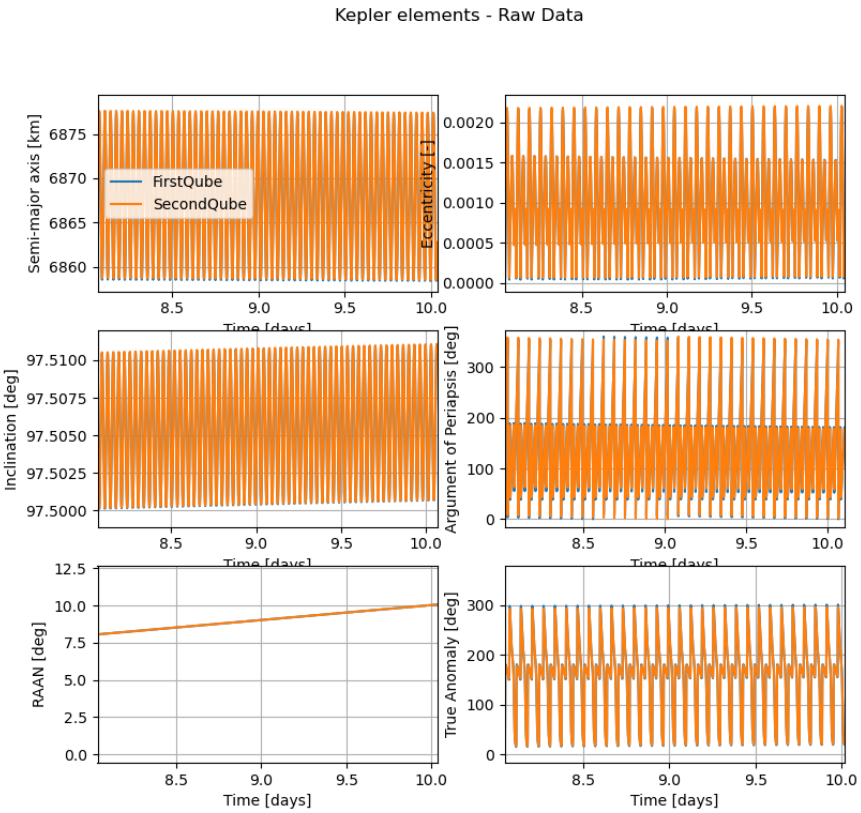

(b) Zoom into the variation of the keplerian parameters at the end of the control actions made on FirstQube, showing the actual osculating trend of the latters.

Fig. 4.7 Kepler Orbital Elements osculating over the simulation epoch set.

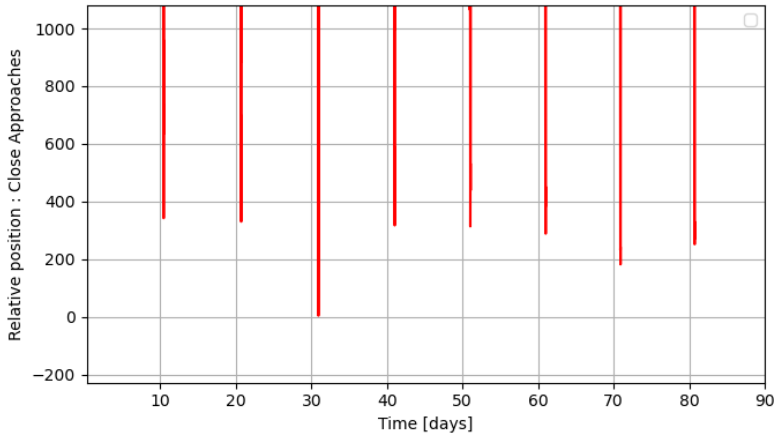

Fig. 4.8 Zoom into the close approaches of the satellites for a simulation epoch of approximately three months.

The direction of separation was defined and provided as a requirement to ensure safety during the First Close Approach (FCA). Initially, the separation distance, which was more than one kilometer, decreases rapidly until collision, and then increases again, resulting in a larger minimum distance.

To address this, the new control approach incorporates a stop condition at a certain minimum distance. This approach ensures that even if one or more control actions are skipped due to system errors, a minimum distance of almost 400 meters is maintained to avoid collisions. This result is valid for reasonably small satellites such as FirstQube and SecondQube.

This new solution involves considering the satellites in a "ping-pong" cycle during their motion. The downside of this choice is an increase in the number of control actions, which directly translates to more time spent in an increased-area configuration. Consequently, this leads to a reduction in orbital lifetime.

Specifically, this approach results in spending 36 % of the time within a cycle (where a cycle refers to the period needed to reach the maximum distance from conjunction) in a high-drag configuration, compared to the previous 22 %. The high-drag configuration corresponds to an area of $0.0148m^2$, while the rest of the time is spent in a low-drag configuration with an area of $0.0074m^2$.

Previously, a new control action was computed when the satellites reached their maximum relative distance. Now, the second satellite is prepared for a high-drag configuration before conjunction, reducing the time spent in a low-drag configuration.

The useful cross-section is computed as follows:

$$A_u = At_{d-a} + At_{i-a}F \tag{4.5}$$

where t_{d-a} indicates the time spent in the basic configuration and t_{i-a} the time spent in an increased area configuration, using F as a multiplication factor.

Two simulations were launched using OSCAR, using the cross-sectional value computed,

calculated to be, respectively, $0.009m^2$ and $0.01m^2$.
The altitude-over-time graphs show a loss of a couple of months using the new mission concept, corresponding to 2.7 years of total lifetime in the first one and approximately 2.6 years in the second one.

4.2.3 Multiplication Factor Study: Relative Velocity Limit

A factor of 2 was given as a requirement at the time that this work-study began. Since some things were modified and further analysis done, a study of this exact multiplication factor was made, right before transforming it into a configuration, defining different aperture angles referred to each different high-drag value.
The following tables aim to show, not only the increase in the percentage of time spent in high-drag but also the increase of the computed cross-sectional area which is translated into a decrease in orbital lifetime, while table 4.1 also depicts the time needed to span the total distance.

Factor	**Avg. t in high-drag [%]**	**Avg. t to reach max distance [days]**
1.5	46	18.5
1.75	44	14.2
2	36	13
2.5	32	10.1
3	25	9.4
3.5	20	8.9
4	17	8.4
4.5	14	8

Table 4.1 Average time (in percentage) spent in high-drag configuration for each cycle and time spent to span the maximum relative distance using different multiplication factors.

Factor	**Cross-Section [cm^2]**	**Lifetime [yrs]**
1.5	91.58	2.607
1.75	101.0	2.234
2	104.7	2.145
2.5	106.7	1.992
3	110.9	1.886
3.5	112.0	1.863
4	112.6	1.840
4.5	113.6	1.817

Table 4.2 Useful cross-section values and consequent orbital lifetime calculated using different multiplication factors.

To increase the factor means that the acceleration given as an input increases as well. However, there is a limit also in terms of the impulse given, since a maximum relative velocity

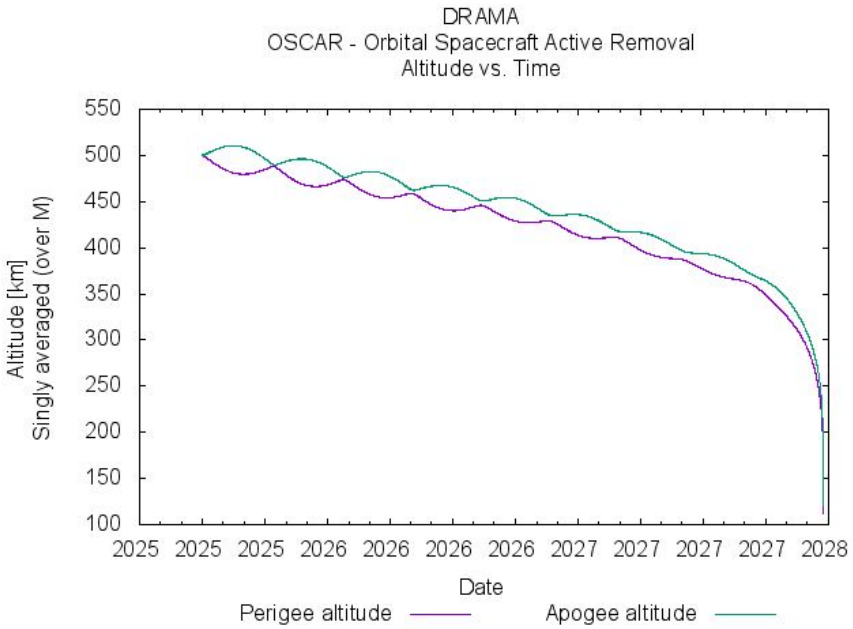

(a) Attitude vs. Time for Architecture 1

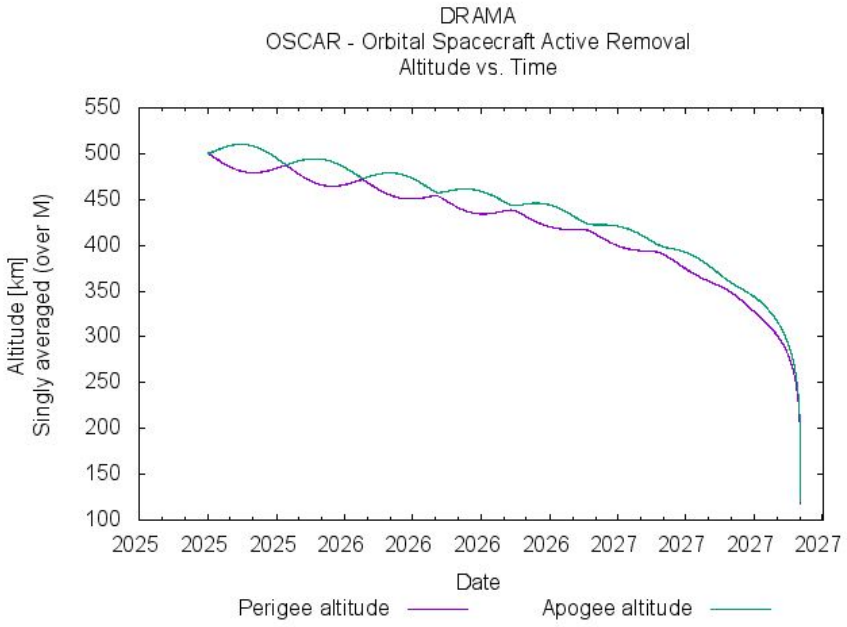

(b) Attitude vs. Time for Architecture 2

Fig. 4.9 Difference in the orbital lifetime of two different mission concepts using the DRAMA - OSCAR tool.

of 10 cm/s is given as a first stopping condition before closing the panel to reach the low-drag configuration again.
The impact of the change in the multiplication factor is shown in figure 4.10. For simplicity, but also for coherence all these simulations have been processed using the same maximum distance, causing reasonably different values in the overshoot. For the same reason, the stop condition in the minimum distance has been avoided for the purpose, since the goal here is to compare the same simulations with just different high-drag configurations. It is evident that after a certain value, the control doesn't work. The reason for this behavior relies on the stopping condition given on the relative velocity given as a requirement. Indeed, a very fast movement of the body affects the purpose of the mission and also increases the complexity of the control actions taken.

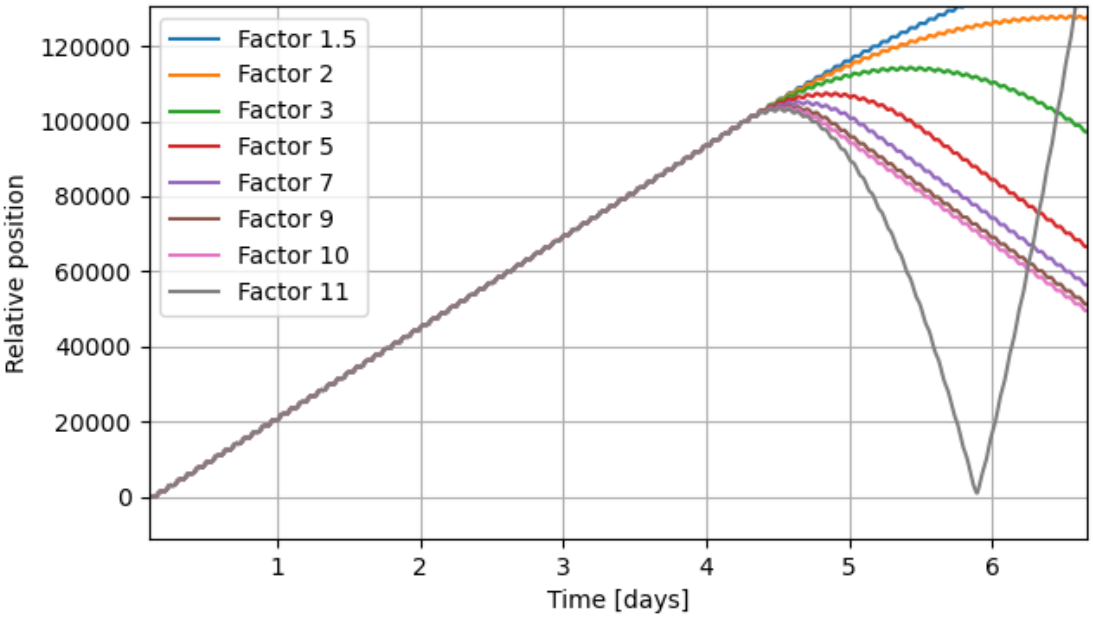

Fig. 4.10 Relative position of FirstQube and SecondQube considering different high-drag factors

Finally, figure 4.11 shows the increase of the pendency of the relative velocity curves, relative to the change in the multiplication factor given for the control.

The first time the satellites skip the control action is within the simulation constructed with a multiplication factor of 11. The pendency of the curve shows that the relative velocity is almost instantaneously brought to the maximum value after almost 4 days. This happens again after almost 28 days within a simulation considering a factor value of 9. Reasonably, the control starts to become risky starting with a factor of 5, as can be seen from the graphs.
A consideration needs to be made in the time step used: for processing time reasons this analysis was made considering a time step of 60 seconds, which affects the calculation of the relative velocity, and the control together with it. Reasonably, a smaller time step permits a better check addressing this control action. As proof, a shorter simulation has been made propagating the

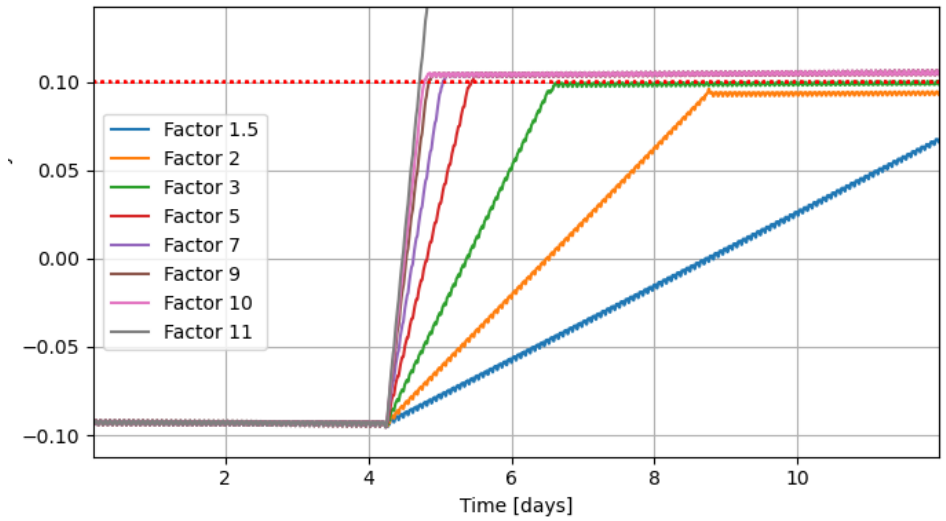

(a) Overshoot for factor 11

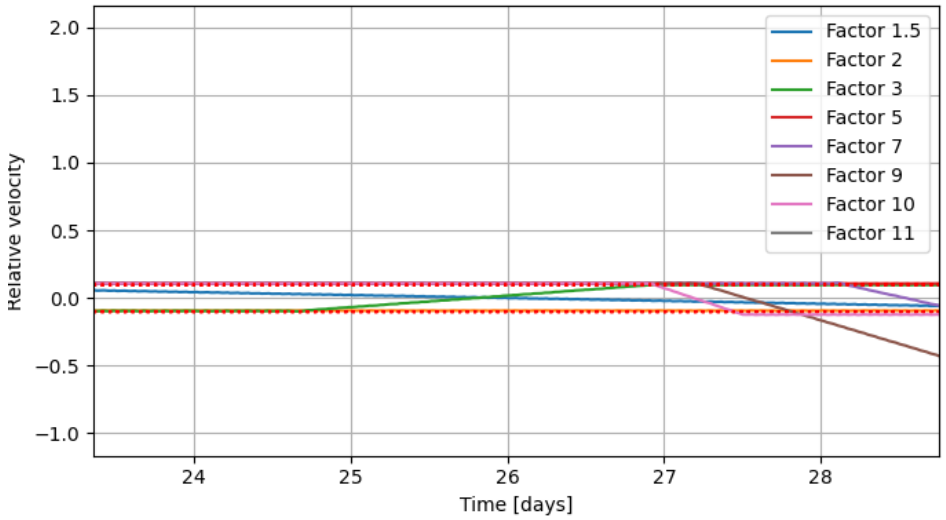

(b) Overshoot for factor 9

Fig. 4.11 Relative velocity avg of FirstQube and SecondQube considering different high-drag factors

orbit with a 10-second time step. Figure 4.12 shows the control skipping a control action for the first time with a minor factor than before.

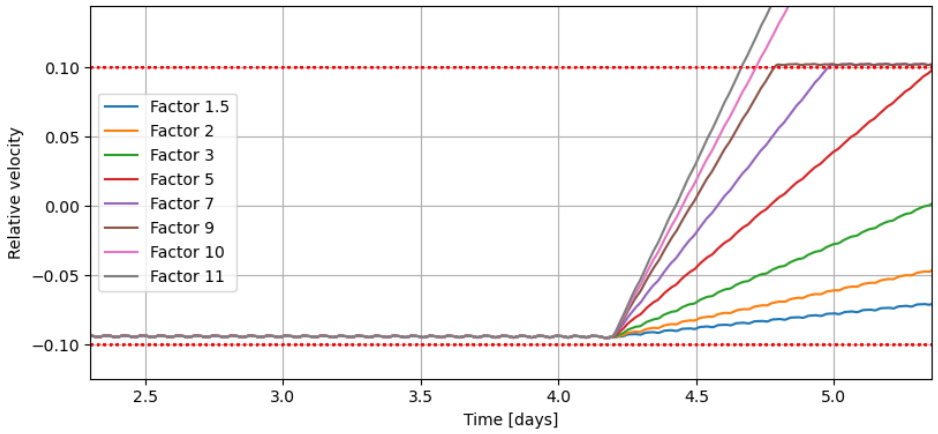

Fig. 4.12 Relative velocity of FirstQube and SecondQube considering different high-drag factors with a reduced time step size.

4.2.4 Multiplication Factor Study: Solar Panels Aperture Angle Limit

This multiplication factor is translated into a specific angle of deployment of the solar panel. These angles have been found using a reverse engineering methodology, i.e. starting from the cross-section evaluated, depending on the time spent in that configuration, finding the relevant disposition right after. It was possible to link these results to a specific configuration using CROC models. Figure 5.9 shows the mission high-drag configuration chosen with its aperture angle of approximately 17 degrees.

Table 4.3 shows all the corresponding aperture angles to all the different multiplication factors used for this analysis. It is evident, that the geometrical limit corresponding to an angle of 90 degrees corresponds to a factor a little bit higher than 4.5, which is also the highest value used for this study.

Factor	**Cross-Section [cm^2]**	**Aperture Angle [deg]**
1.5	111.97	11
1.75	130.64	15
2	149.30	17
2.5	186.62	25
3	223.95	37
3.5	261.27	45
4	298.60	56
4.5	335.59	69
5	373.25	-

Table 4.3 Multiplication Factors vs. Aperture Angles of the Solar Panels.

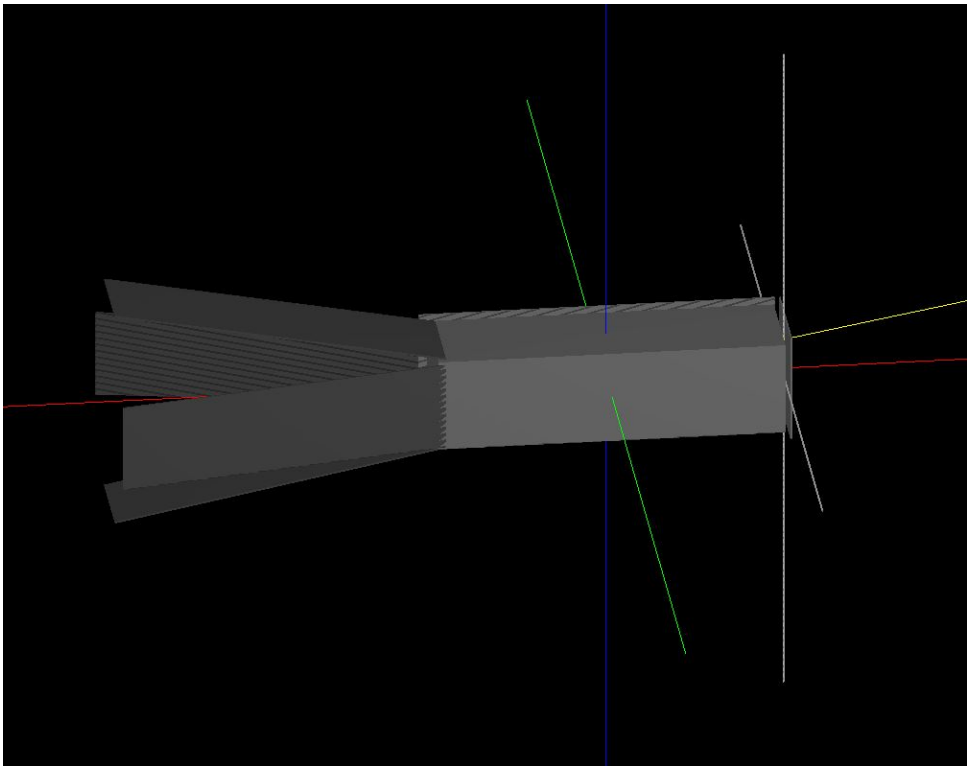

Fig. 4.13 DRAMA-CROC model with an aperture angle of 17 degrees corresponding to a multiplication factor of 2.

Single points are highlighted in figure 4.14 to specify the corresponding cross-section in two different graphs showing the increasing trend of the cross-section with respect to the multiplication factors, as well as the decreasing trend of the orbital lifetime.

4.3 Numerical validation for Relative Navigation

4.3.1 Perturbated Model Validation

The idea here is to demonstrate the relative navigation, using an analytical method, which is also precise but should be less time-consuming in terms of processing time. The main goal is also to understand the benefits of such a model.
To do so, a test involving two orbiting satellites flying in near-circular orbit was constructed to validate the model retrieving the relative navigation output. Indeed, the motion is described using the relative orbital elements, and both Earth's oblateness and differential drag are addressed in it. This work consists of a reproduction of some results addressed on the *Mission analysis and guidance and control for the SpEye inspection CubeSat* used for proximity operations demonstration for a CubeSat mission [16]. The reference orbits are computed via numerical integration at a 10-second time step. The dimensional reference vector ($a\delta\alpha^{ref}$) is calculated step by step. The modeled vector ($a\delta\alpha^{model}$) is instead derived using the state transition matrices.

(a) Cross-Section vs. High-Drag Factor

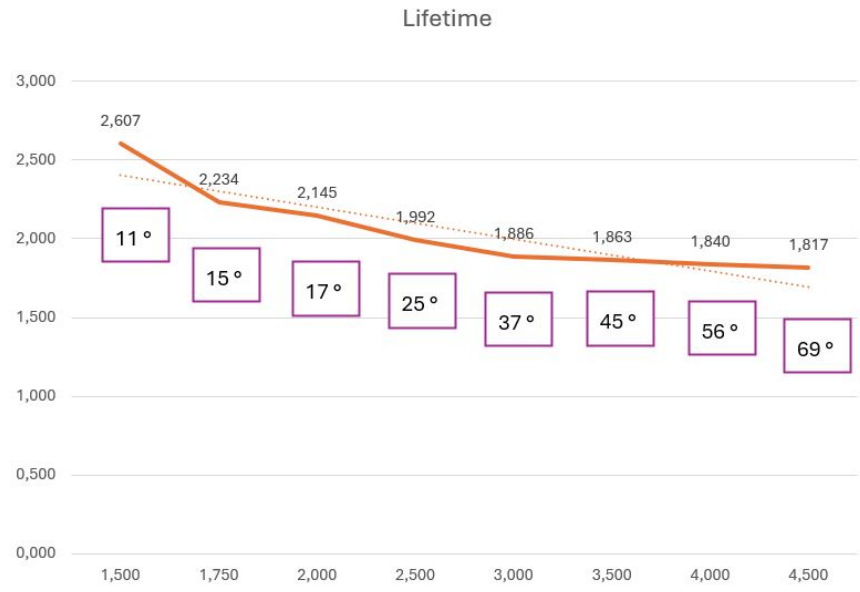

(b) Lifetime vs. High-Drag Factor

Fig. 4.14 Solar Panels Aperture Angles values corresponding to each cross-section and orbital lifetime value.

Chaser orbit					
SSO	h = 500 km	e = 0.001	$\Omega = f(t_0, LTAN)$	$\omega_0 = 0$	$M_0 = 0$
Relative orbits					
$a\delta a_0[m]$	$a\delta\lambda_0[m]$	$a\delta e_{x0}[m]$	$a\delta e_{y0}[m]$	$a\delta i_{x0}[m]$	$a\delta i_{y0}[m]$
0	5000	30	250	-10	300

Table 4.4 Absolute and relative orbits initial conditions for the simulation across the reference paper [**?**]

Table 4.4 shows the initial conditions used for the analysis. To fit the paper's results the chaser is injected in a 500 km high Sun-Synchronous Orbit (SSO) of eccentricity 0.001. The scenario studied consists of a mean along-track separation of 5 km and an almost parallel relative inclination/eccentricity vector configuration.

The analytical solution modeled is retrieved from the reference solution as follows:

$$a\delta\alpha(t)^{model} = \Phi(t,t_0)a\delta\alpha_0^{ref} \tag{4.6}$$

This means that to reduce initialization errors, the model starts by retrieving the state at the beginning of the epoch from the numerical propagation of motion, i.e. the reference. At this point, the motion is entirely constructed by using the relative parameters of the chaser concerning the target.
Considering that the drag acceleration has only effects in the along-track direction, an empirical model for the satellite perturbation can be defined as follows:

$$\mathbf{d}_{\text{drag}} = \begin{pmatrix} 0 \\ Acos(nt) + Bsin(nt) + C \\ 0 \end{pmatrix} \tag{4.7}$$

plus, addressing to the acceleration a general harmonic expression in the along-track direction [16]. Using the least square method through the *scipy.optimize* library, retrieving the acceleration from the propagation analysis, the coefficients are calculated, where A and B are the amplitudes of the once-per-orbit periodic part and C is the mean value of the perturbation acceleration. Finally, the mean variations of some in-plane elements, which complete the relative state in Relative Orbital Elements (ROEs), consist of:

$$\begin{aligned} a\delta\dot{a} &= \frac{2}{n}C \\ a\delta\dot{e}_x &= \frac{1}{n}A \\ a\delta\dot{e}_y &= \frac{1}{n}B \end{aligned} \tag{4.8}$$

To be more precise, these coefficients can be re-computed every time the orbit changes significantly, but this test is not the case, so they will stick to their initial value.

The complete state is finally defined as:

$$\zeta = (a\delta\alpha,\ a\delta\dot{a},\ a\delta\dot{e_x},\ a\delta\dot{e_y}) \tag{4.9}$$

The STM matrix, considering the relative motion, described by the HCW equation (seen in Chapter 2), subject to the J2 perturbation is computed by summing the following matrices:

$$\Phi_{HCW}(t,t_0) = \begin{bmatrix} 1 & 0 & 0 & 0 & 0 & 0 \\ -\frac{3}{2}ndt & 1 & 0 & 0 & 0 & 0 \\ 0 & 0 & 1 & 0 & 0 & 0 \\ 0 & 0 & 0 & 1 & 0 & 0 \\ 0 & 0 & 0 & 0 & 1 & 0 \\ 0 & 0 & 0 & 0 & 0 & 1 \end{bmatrix} \tag{4.10}$$

$$\Phi_{J2}(t,t_0) = \begin{bmatrix} 0 & 0 & 0 & 0 & 0 & 0 \\ -\frac{21}{4}(3cos(i)^2-1)(\eta+1) & 0 & 0 & 0 & -\frac{3}{2}\gamma sin(2i)(3\eta+4) & 0 \\ 0 & 0 & 0 & -\phi' & 0 & 0 \\ 0 & 0 & 0 & \phi' & 0 & 0 \\ 0 & 0 & 0 & 0 & 0 & 0 \\ \frac{21}{4}sin(2i) & 0 & 0 & 0 & 3\gamma sin(i)^2 & 0 \end{bmatrix} \tag{4.11}$$

where $\eta = \sqrt{1-e^2}$, $\gamma = \frac{J2}{2}\frac{R_{earth}^2}{a^2\eta^4}$ and $\phi' = \frac{3}{2}\gamma(5cos(i)^2-1)$.
The last state transition matrix accounting for the joints effect of J2 and differential drag, is:

$$\Phi_{d-drag}(t,t_0) = \begin{bmatrix} dt & \frac{2}{n}sin(u-u_0) & \frac{2}{n}(1-cos(u-u_0)) \\ -\frac{3}{4}ndt^2 & -\frac{3}{n}(1-cos(u-u_0)) & -3dt+\frac{3}{n}sin(u-u_0) \\ \frac{sin(u-u_0}{n} & dt+\frac{cos(u-u_0)sin(u-u_0}{n} & \frac{sin(u-u_0)^2}{n} \\ \frac{1-cos(u-u_0}{n} & \frac{sin(u-u_0)^2}{n} & dt-\frac{cos(u-u_0)sin(u-u_0}{n} \\ 0 & 0 & 0 \\ 0 & 0 & 0 \end{bmatrix} \tag{4.12}$$

becoming:

$$\tilde{\Phi}_{d-drag}(t,t_0) = \Phi_{d-drag}(t,t_0) + \begin{bmatrix} 0 & \mathbf{0}_{1x2} \\ -\frac{21}{8}(3cos(i)^2-1)ndt^2 & \mathbf{0}_{1x2} \\ \mathbf{0}_{3x1} & \mathbf{0}_{3x2} \\ \frac{21}{8}\gamma sin(2i)ndt^2 & \mathbf{0}_{1x2} \end{bmatrix} \tag{4.13}$$

By augmenting the vector containing the with the latter time derivative quantities, the linear STM model addressing differential drag is the following:

$$\zeta(t) = \begin{bmatrix} \Phi_{HCW}(t,t_0) + \Phi_{J2}(t,t_0) & \tilde{\Phi}_{d-drag}(t,t_0) \\ \mathbf{0}_{3x6} & \mathbf{I}_{3x3} \end{bmatrix} \zeta_0 \tag{4.14}$$

A change of variable between the relative orbital element state and the Cartesian state (δx, δy, δz, δvx, δvy, δvz) is computed starting from matrix $T(t)$, computing the state vector in the RTN reference frame:

$$\delta \mathbf{x} = T(t) a \delta \alpha \tag{4.15}$$

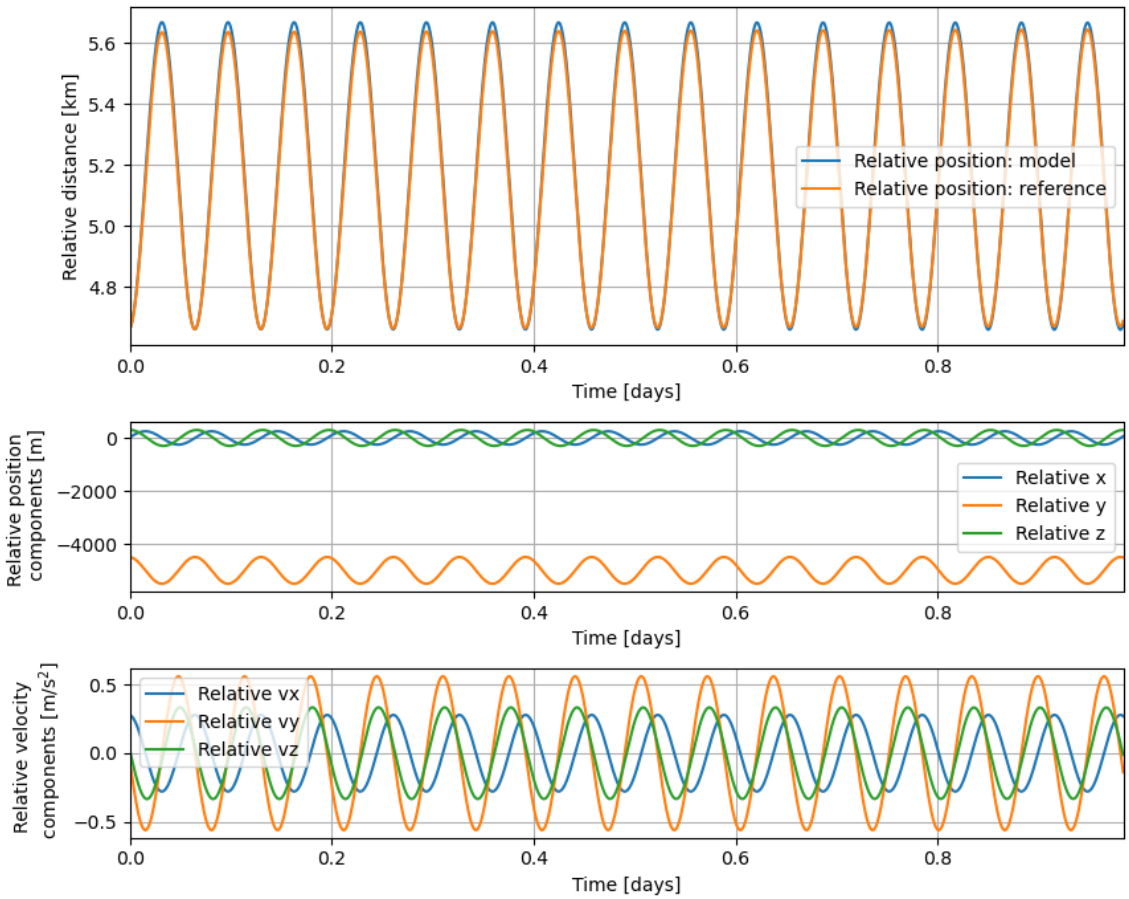

Fig. 4.15 Relative state trend over 15 orbits addressing both the model and the reference values

Figure 4.9 shows the relative state calculated from the model and the reference values overlapping almost perfectly, within an error.
The error in the model is highly dependent on the time step chosen for the motion propagation, and so is the drift from the initial mean value. In particular, figure **??** shows that, while the trend of the mean error stays mostly the same, the actual osculating error is higher for higher steps, for a maximum error staying under 70 meters for a time step of 1 minute and under 20 meters for a time step of 0.1 seconds.

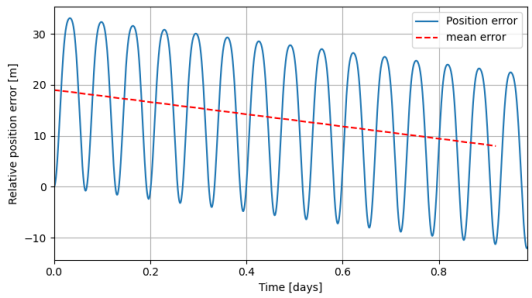

(a) State error: 0.1 second time step

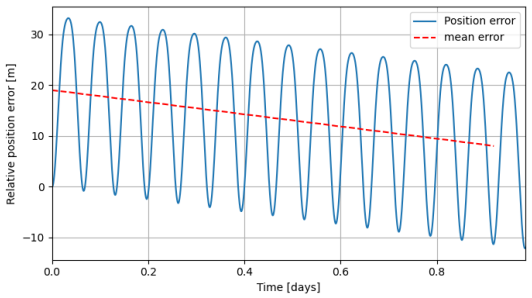

(b) State error: 1 second time step

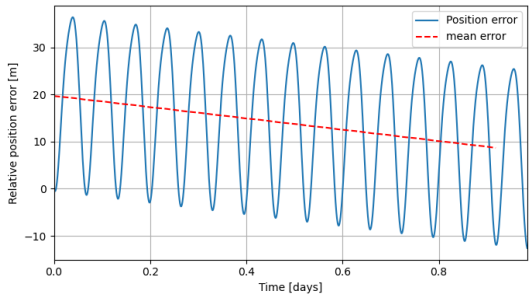

(c) State error: 10 seconds time step

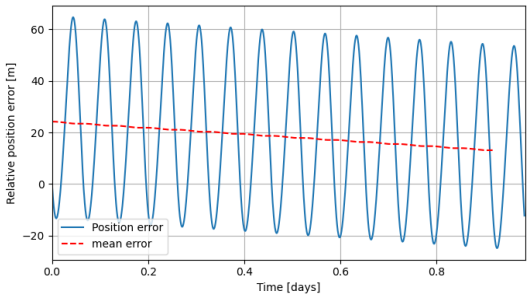

(d) State error: 60 seconds time step

Fig. 4.16 Error trend over 15 orbits using different step size

Finally, the modeling error studied to validate the model is the difference between the ROEs extracted from the vector $\zeta(t)^{model}$ and the reference value $a\delta\alpha^{ref}$. This error calculated using the initial conditions presented, with the two satellites moving at a mean along-track separation of 5000 m for 15 orbits, is shown in figure 4.21. By comparing the modeled ROEs with the reference directly from the osculating absolute elements, the numerical validation of the approach is judged validated with a maximum error affecting $a\delta\lambda$, depending on the time step chosen, considering the satellite under the effect of both J2 perturbations and atmospheric drag, the general set of perturbations considered for the simulation.

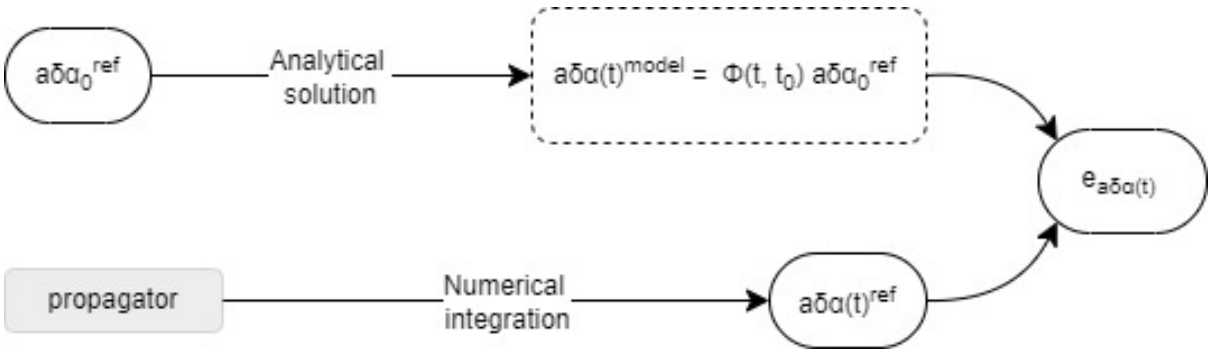

Fig. 4.17 Modeling error from reference values: Absolute and Relative Navigation precision analysis

Using the osculating Kepler elements calculated with the propagator as an initial state input, the modeled state then evolves through the STM and the equations described above. the modeling error is meant to be the difference between the ROEs extracted from $\zeta(t)^{model}$ and

the reference values $a\delta\alpha^{ref}$, using the mean values as explained in the flow chart in figure 4.17. The latter derives directly from the numerical propagation using Tudat.
For this case, the numerical values of the initial additional parameter required for the analytical model are obtained through numerical fitting of the reference simulated data over the time of the epoch considered, and the constants evaluated for the case are:

$$\begin{aligned} A &= -4.3922e-09 \\ B &= -4.2285e-09 \\ C &= -9.0298e-09 \end{aligned} \tag{4.16}$$

The model results are within the accuracy of the meter, with higher discrepancies in the mean relative longitude and the mean eccentricity values.

4.3.2 Relative Navigation Demonstration for Twin-Sat mission

After the validation of the model, the Relative Navigation tool was ready to be used in the Twin-Sat simulation phases. At this point, two considerations had to be taken into account to proceed:

- Is the model accurate within the distance maintained by the satellites during the overall simulation epoch?
- What kind of impact does this have in terms of processing time?

After validating the model, the simulation was modified adding here, as in the demo simulation tested, a comparison of the model and the reference values retrieved from the absolute parameters.
The idea is to insert the model inside the actual simulation environment constructed using Tudat and evaluate what kind of output it gives using different time steps, similarly as before.
The main idea then was to evaluate how much the error is growing toward the overall distance maintained by the satellites during their cycles. In order to do so, analyses have been done taking into consideration, not only the simulation orbits but also all the distance spans that the two satellites proceed on during their motion.

Figure 4.20 shows the error in the relative position, similarly as it has been done during the validation test for the model. The error and its mean values increase with the relative distance, but it decreases overall with the decrease of the time span used for the case. In this example, the 0.1 seconds case has been avoided due to computational time, but three cases have been studied to better evaluate its response. The graphs show an evident reduction in the error, causing on the other hand a higher computational complexity, i.e. longer processing time.
Again, the modeling error defined as the difference between the ROEs and the reference values

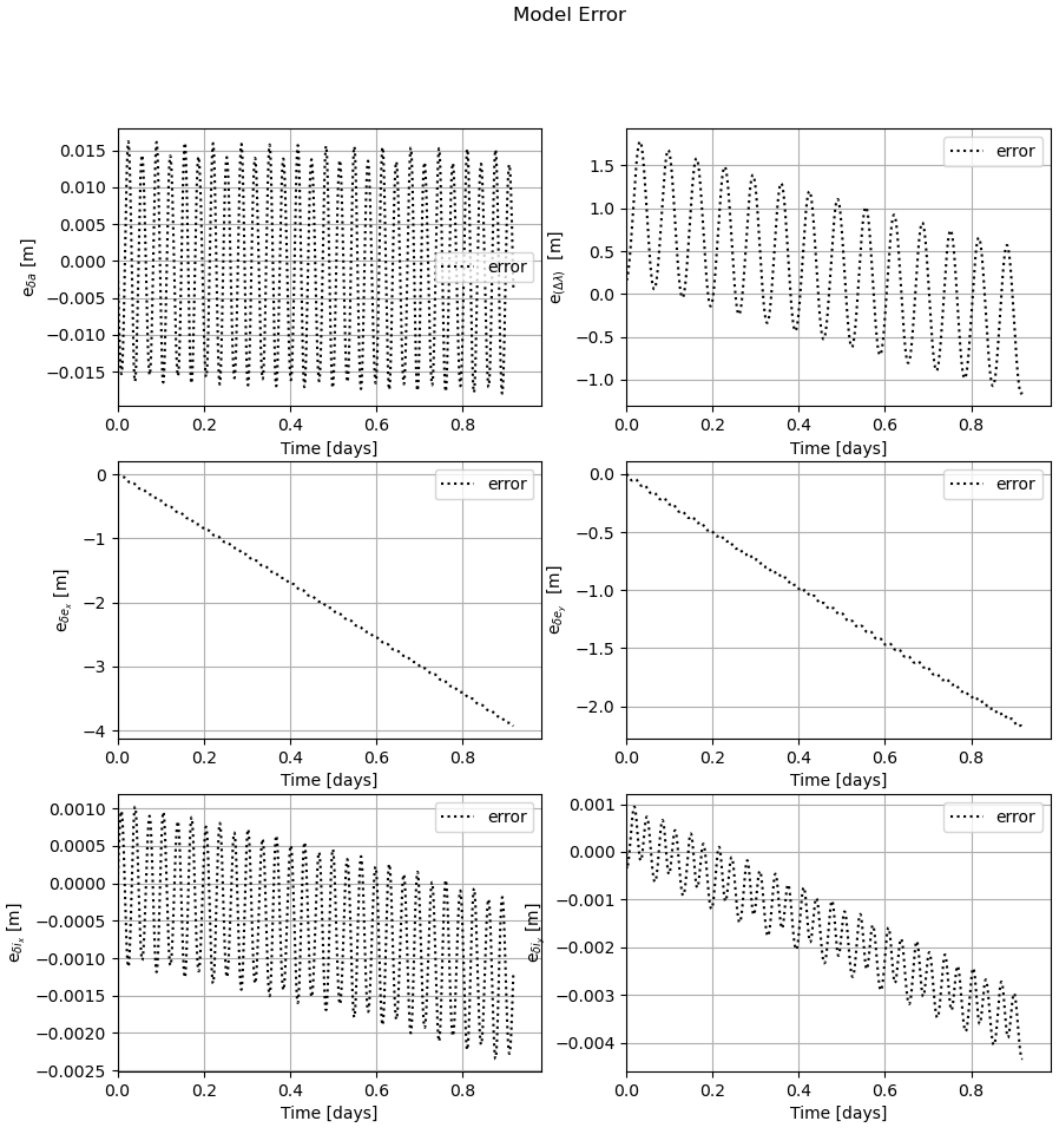

Fig. 4.18 Modeling error over 15 orbits of the test simulation

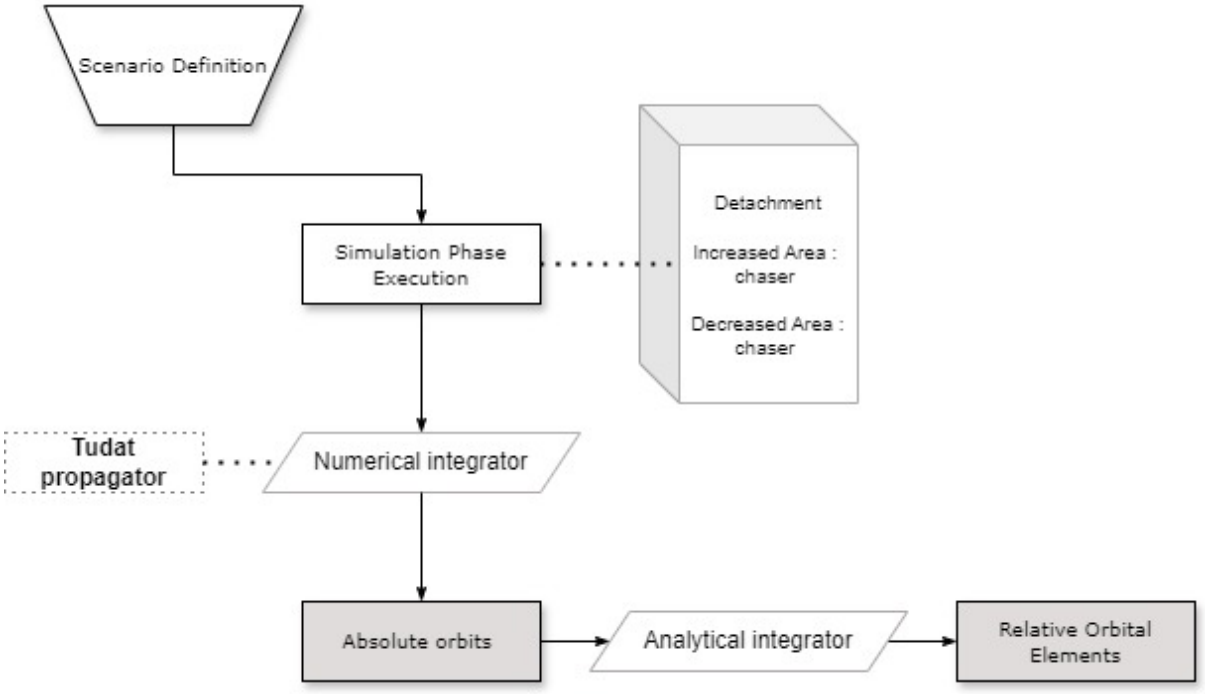

Fig. 4.19 Simulation phase's flowchart for retrieving absolute and relative orbits

from the absolute navigation propagation has been evaluated. Figure 4.20 shows the trend of the error, which again affects the mean eccentricity components and the mean along-track separation reasonably considering the increase of the relative distance.
Overall the model is considered valid since this value is calculated to be always within the 0.1% of the reference, in the worst-case scenario.

To answer the second question, it is necessary to study the computational time of both methods. Firstly, the processing time to retrieve the absolute parameters, and secondly, the processing time of the latter.
Using the relative Cartesian state is a common way to parameterize the orbit, obtained by a combination of the individual state vectors. Again, the fundamental equations are linearized in order to obtain the familiar Clohessy-Wiltshire equations of relative motion. These equations lead to a new matrix, which permits to obtain the Cartesian state directly from the ROEs. So, when the simulation process is used using the propagator, the absolute state and the consequent orbital elements are directly computed, under the assumptions of a Keplerian two-body motion, a circular orbit of the deputy, and a small distance separation compared to the chaser's orbit radius.

4.3.3 Processing Time Analysis

As introduced before, one of the main issues of the methods used for propagating the orbit of one satellite can be its processing time, usually very time-consuming.
One of the goals of this chapter was to show the amount of time needed for the propagation using

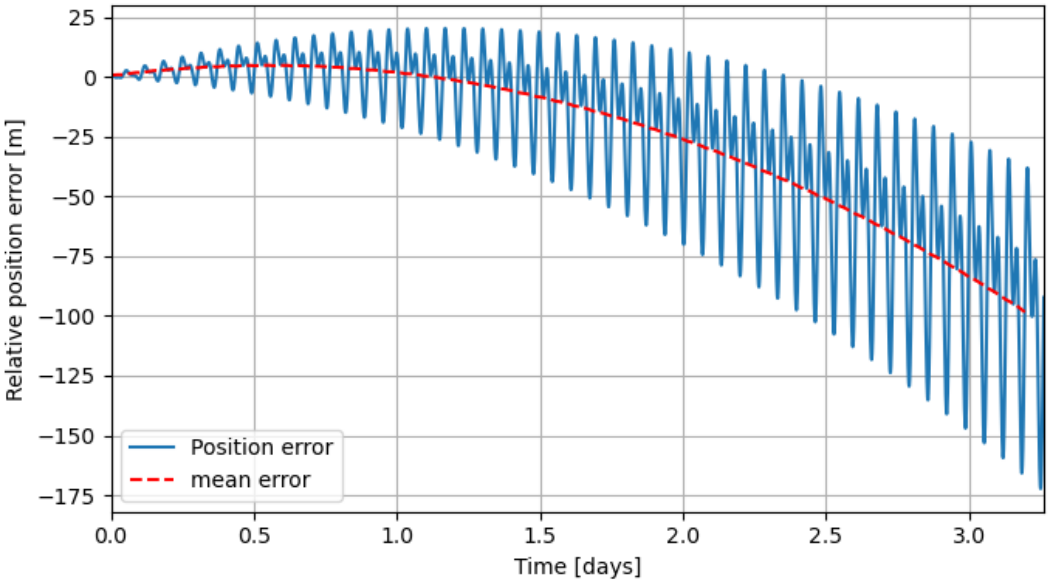

(a) State error: 1 second time step

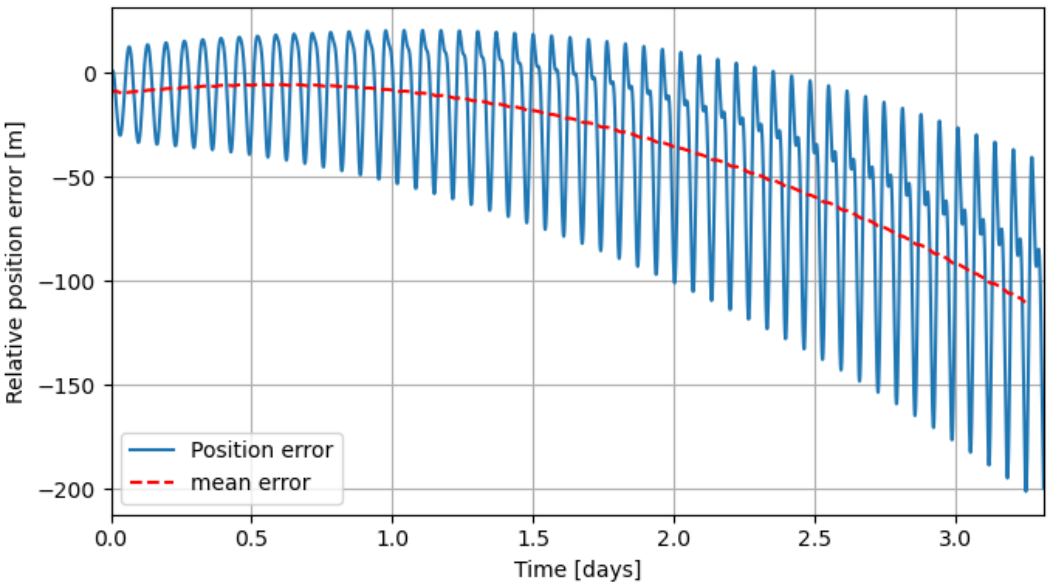

(b) State error: 60 seconds time step

Fig. 4.20 Error trend over the 100 km distance span using different step size

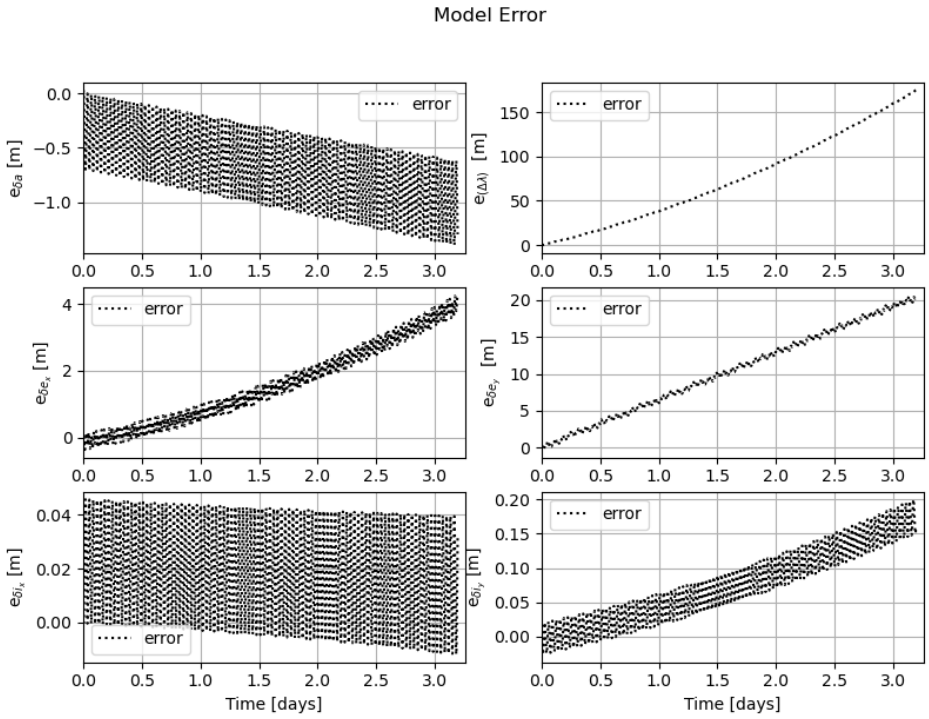

(a) Modeling error using a 1 second time step

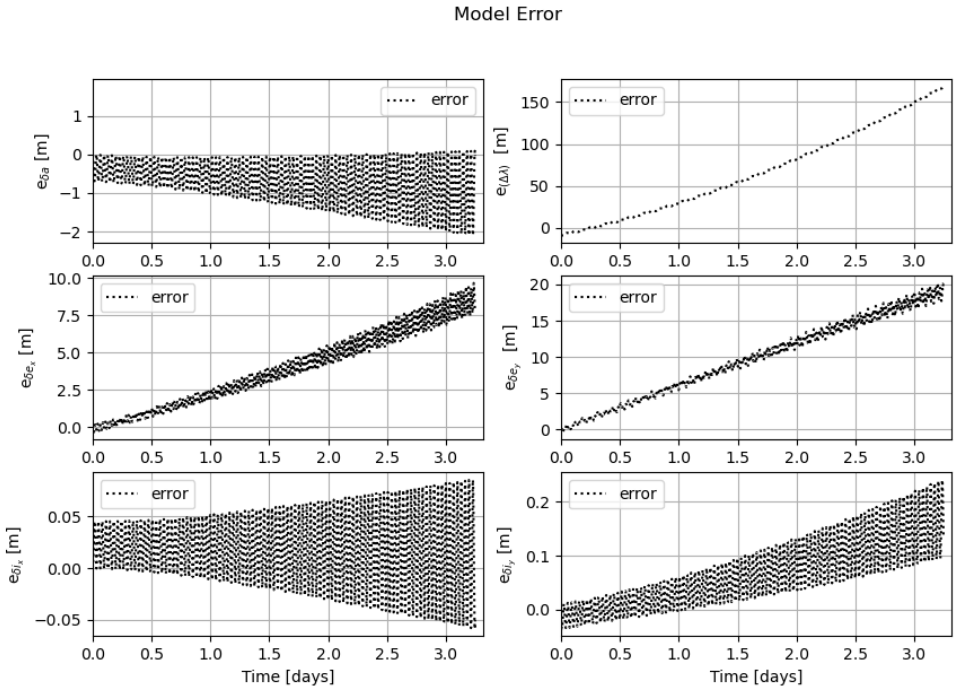

(b) Modeling error using a 60 seconds time step

Fig. 4.21 Modeling error trend over the 100 km distance span using different step size

different time steps. Table 4.5 shows the results of the same simulations previously described over a couple of orbit propagations, using different time steps from 0.1 seconds up to 1 minute.

Time step [sec]	Elapsed time: numerical [sec]	Elapsed time: analytical [sec]
60	0.32	0.05
10	0.78	0.23
1	5.93	4.99
0.1	65.48	659.45

Table 4.5 Processing time for a simulation epoch of one week using different time steps for the integration using the numerical method for the calculation of the orbit.

The amount of time necessary increases faster and almost proportionally with the time step used, from less than a minute up to more than 1 hour and a half, for a one-week simulation.
However, using higher time steps doesn't really affect the simulation results, for this type of orbit, as it happens for the analytical method retrieving the relative parameters. In the previous section, it has been shown in fact how much the osculating error, more than the mean one, drifts from the real value. One of the results of the previous analysis showed that a reduction of the time step under 1 second doesn't really show particular differences, which makes the higher computational cost in this case unnecessary.
The processing time of the analytical method is more difficult to evaluate precisely since the model is not made to be used continuously. Moreover, despite the Tudat propagation, this model can be further improved and the processing time consequently reduced. Furthermore, in this model, for inspection reasons, a lot of computed results used to have valuable results and to compare the models, would be unnecessary when using it within the scope of a mission. In particular, the calculation of the orbital elements could be avoided and the ROEs vector can be directly used to retrieve the parameters when necessary. Within the scope of this thesis, a comparison of the absolute and relative parameters has been important for the validation of the model.
To conclude, a dynamical propagation using the STM matrices drops down the computational cost, but can also increase depending on the data to process, considering what was stated before about the nature of the analysis made. Moreover, it can be more intuitive to directly use a relative model, together with the advantage of needing less computational memory.

Chapter 5

GNSS Simulation Emulator

This chapter serves as an evaluation of the GNSS receiver's accuracy in positioning measurements using multiple hardware-in-the-loop (HIL) simulations. The Skydel Software is introduced along with the setup employed for these evaluations. The study examines the receiver's accuracy and identifies various types of errors. Additionally, Keplerian parameters of the observable are reconstructed to better understand the sources of error. Finally, an orbit estimation method is introduced and implemented to further validate the findings.

5.1 Global Navigation Satellite System Basics

5.1.1 Evolution of Satellite Navigation

In a broad sense, navigation encompasses the processes of monitoring and controlling the movement of a craft or vehicle from one location to another. Navigation pertains to the field of study that focuses on determining a vehicle's position, velocity, attitude, and angular rate.
Examples of navigation methods include beacon navigation, radio navigation, visual navigation, terrain navigation, celestial navigation, satellite navigation, and inertial navigation.
Satellite navigation technology refers to the provision of three-dimensional positioning and time information services to users via radio navigation signals broadcasted by satellites [17]. This technology represents a form of non-autonomous navigation, necessitating the integration of the user's equipment with other external instruments or systems to facilitate navigation functions.
During the final phase of navigation's evolution in the 1960s, the introduction of astronautic technology and microelectronics significantly led to higher precision of spatial reference frames, time-frequency references, and orbit determination. In 1957, the Soviet Union launched its first artificial satellite, and the Americans discovered the correlation between satellite orbits and the Doppler shift curve of radio signals. Consequently, the Navy Navigation Satellite System (NNSS), commonly known as Transit, emerged in 1958, underscoring the superiority of satellite navigation. The GPS officially commenced in 1994, approximately two decades prior to the

European Galileo system, and a year before the Soviet GLONASS.
The fundamental function of satellite navigation is to provide users with Position, Navigation and Timing (PNT) services. Satellites continuously acquire and broadcast data, while users consistently receive these broadcast signals.

- *Positioning* involves determining the user's location through measurements, receiving radio navigation signals from satellites, and calculating the satellite's spatial position at the time based on ephemeris information and the distance between the satellite and the user, including pseudo-range and carrier phase.
- *Navigation* entails guiding crafts or individuals, encompassing the collective sciences and technologies associated with this process.
- *Timing* is based on pseudo-range delay, satellite clock information, and the user's clock difference in positioning solutions, which can be converted to UTC time when referencing GNSS standard time.

Overall, PNT functions enable the establishment and maintenance of temporal and spatial references for users both on Earth and in space.

5.1.2 Fundamentals of Satellite Navigation

When defining a specific type of satellite navigation, the selection of measurement, positioning, and multiple-access methods is crucial [18]. Measurement begins with the acquisition of signals emitted by the satellite. Two primary methodologies are employed: Doppler velocity measurement and spread spectrum ranging measurement.
A Doppler shift measurement technique considers an altimeter receiving signals from the satellite, measures the Doppler frequency shift according to the carrier phase difference and accumulates the number of Doppler cycles over a period of time:

$$f_d(t) = \frac{\Phi(t+T) - \Phi(t)}{T} \tag{5.1}$$

This shift is integrated to subsequently calculate the change in distance between the user and the satellite. Given that the user's velocity is known, their position can be determined. The satellite's position in the Earth-Centered, Earth-Fixed (ECEF) frame is provided as a message and denoted as (X_n, Y_n, Z_n) at the n-th time point, while the user's position, denoted as (x, y, z),

can be calculated accordingly:

$$\begin{cases} \Delta\Phi_{12} = \sqrt{(X_2-x)^2+(Y_2-y)^2+(Z_2-z)^2} - \sqrt{(X_1-x)^2+(Y_1-y)^2+(Z_1-z)^2} + \varepsilon_1 \\ \Delta\Phi_{13} = \sqrt{(X_3-x)^2+(Y_3-y)^2+(Z_3-z)^2} - \sqrt{(X_1-x)^2+(Y_1-y)^2+(Z_1-z)^2} + \varepsilon_2 \\ \Delta\Phi_{14} = \sqrt{(X_4-x)^2+(Y_4-y)^2+(Z_4-z)^2} - \sqrt{(X_1-x)^2+(Y_1-y)^2+(Z_1-z)^2} + \varepsilon_3 \end{cases} \tag{5.2}$$

where ε_i is the measurement noise.

The position method of GNSS is a geometric three-ball intersection, where the radius is the distance user-satellite and the position of the user is the intersection of those balls. Considering positions and clock biases of the satellites as known data $(x_i, y_i.z_i, \delta t_{s,i})$, the position and the clock bias of the user are computed because selected as the unknown data $(x, y, z, \delta t_u)$.

The pseudo-range is defined as the difference between the signal-receiving t_r time and the signal-transmitting time t_t:

$$\rho_i = c(t_r - t_t) \tag{5.3}$$

At this point, a set of four equations is constructed, knowing that the set of positions and clock biases of the satellites are given as messages, while the user's variables $(x, y, z, \delta t_u)$ are calculated using the pseudo-range as follows:

$$\begin{cases} \sqrt{(x_1-x)^2+(y_1-y)^2+(z_1-z)^2} = \rho_1 - c(\delta t_u - \delta t_{s,1}) \\ \sqrt{(x_2-x)^2+(y_2-y)^2+(z_2-z)^2} = \rho_2 - c(\delta t_u - \delta t_{s,2}) \\ \sqrt{(x_3-x)^2+(y_3-y)^2+(z_3-z)^2} = \rho_3 - c(\delta t_u - \delta t_{s,3}) \\ \sqrt{(x_4-x)^2+(y_4-y)^2+(z_4-z)^2} = \rho_4 - c(\delta t_u - \delta t_{s,4}) \end{cases} \tag{5.4}$$

In the GNSS positioning then more than four signals from four different satellites are needed in order to adjust the clock biases and calculate the fourth variable of the system. To do so, the signals are distinguished with a multiple-access method (Time Division Multiple Access (TDMA), Frequency Division Multiple Access (FDMA), Code Division Multiple Access (CDMA)).

The main independent satellite navigation systems have their own time-frequency systems by setting the atomic clock groups, associated with each other through Coordinated Universal Time (UTC), a time system based on International Atomic Time (TAI).

The ephemeris parameters include a reference time, the six Kepler elements, and a set of correction coefficients used to calculate the orbit by the formula. Precise orbit determination and time synchronization are crucial to ensure the accuracy of such a system.

5.1.3 Errors Sources

An introduction of the type of errors encountered while sending a signal is given to better understand the insight of the error in the output of the simulation built for the case. The accuracy of the GNSS positioning is influenced by various source of errors that accumulates: satellite errors, atmospheric errors, and receiver errors. Being these:

- *Clock drifts*. For cost and dimensional reasons, while the atomic clock on GNSS satellites requires very high precision, the clock in the GNSS receiver is usually less accurate. For instance, a 1 microseconds error translates into a 300 meters error in the position, being the satellite moving at almost the speed of light.
- *Orbit drifts*. Similarly to the satellite clock, even a slight change in the orbit computed can cause a major positional error. Usually, the ephemeris broadcast of each satellite is updated every 2 hours for the error correction of the clock and the orbit parameters.
- *Ionospheric delay*. The ionosphere exists between 50 and 1000 km above sea level, containing ions affecting radio signal transmission, depending on the solar activity, daytime, season, and location.
- *Multipath error*. The satellite signal can be reflected from surfaces, such as water, walls, and buildings, which introduces mistakes in the computation of the signal
- *Diluition of Position (DOP)*. DOP is a measurement of the quality of the geometric spread across the sky.

5.2 GNSS Signal Emulator

5.2.1 Skydel Simulation Software

Previous simulations utilized the open-source GPS-SDR-SIM software. In contrast, Safran's Skydel GNSS software offers greater flexibility, scalability, upgradability, and cost-efficiency compared to traditional FPGA-based simulators [19]. Skydel is also compatible with all major GNSS constellations and frequencies, including GPS, GLONASS, Galileo, BeiDou, QZSS, and NavIC.
The primary goal of a GNSS simulators is to generate an RF signal that reproduces the Live-Sky signal at the GNSS receiver's RF input connector. It generates a digital signal composed of millions of IQ samples per second. This digital signal is subsequently converted into an analog signal and then into RF.
IQ data is extremely useful for the following reasons:

- Playback. It can be used as a recording

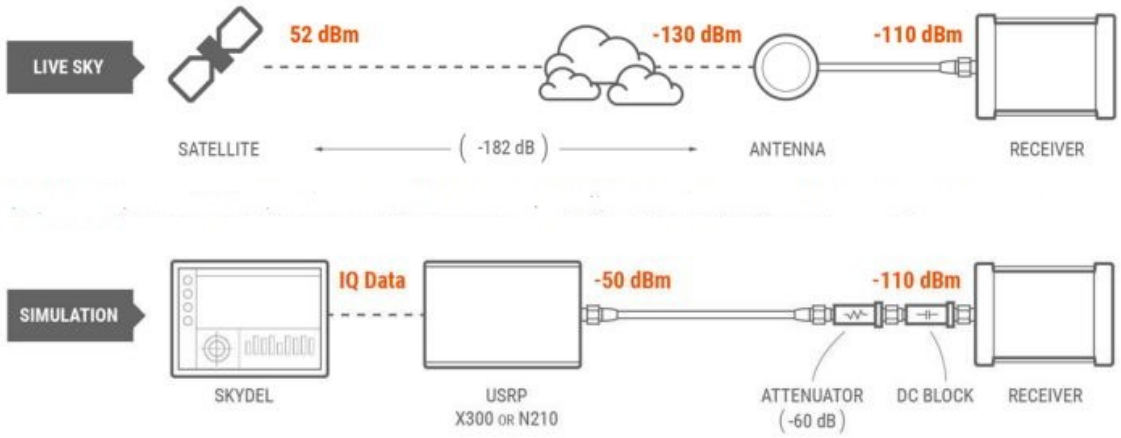

Fig. 5.1 Propagation of real GNSS signal from satellite vs. simulated GNSS signal from Skydel tot he GNSS receiver

- Spoofing. It can be used as a spoofed signal along with a jamming transmitter.
- Software-in-the-loop. The IQ file can be sent to a software-defined GNSS receiver without having to go through digital to analog and analog to digital.
- Research. The IQ file can be processed, modified, and combined with other IQ files.
- CRPA. Users can create multiple IQ files, one for each element of the CRPA.

Skydel, using a computer setup, generates real-time I/Q samples representing the baseband signals. These samples are transmitted over a transport link, such as Ethernet or USB, and queued in the SDR buffer. The SDR retrieves the samples from the buffer at a consistent rate and converts them to RF. If the SDR has multiple outputs, the signals are combined into a single RF cable. The RF signal is then attenuated before passing through a DC Block and reaching the GNSS receiver under test.
The Settings, Receiver, and Map Tabs feature a horizontal divider that allows the display window to be divided as desired. The top portion of the window shows content based on the selected Main Window Tab, while the bottom portion provides subtabs for views of Constellations, Deviation, Spectrum, Performance, and Status Log.

Running a simulation on Skydel

For the scenario of interest, there are two primary options for generating the output: an NMEA file or a CSV file. The TwinSat scenario is created and imported using the *Track Playback* tab, but Keplerian parameters can be as well defined directly to generate orbit predictions using the *Earth-Orbiting Spacecraft* option.
Skydel uses the ECEF geographic coordinate system but it can also convert LLA using the WGS84 ellipsoid model, so then inserting a track it is possible starting from LLA or ECEF/ECI

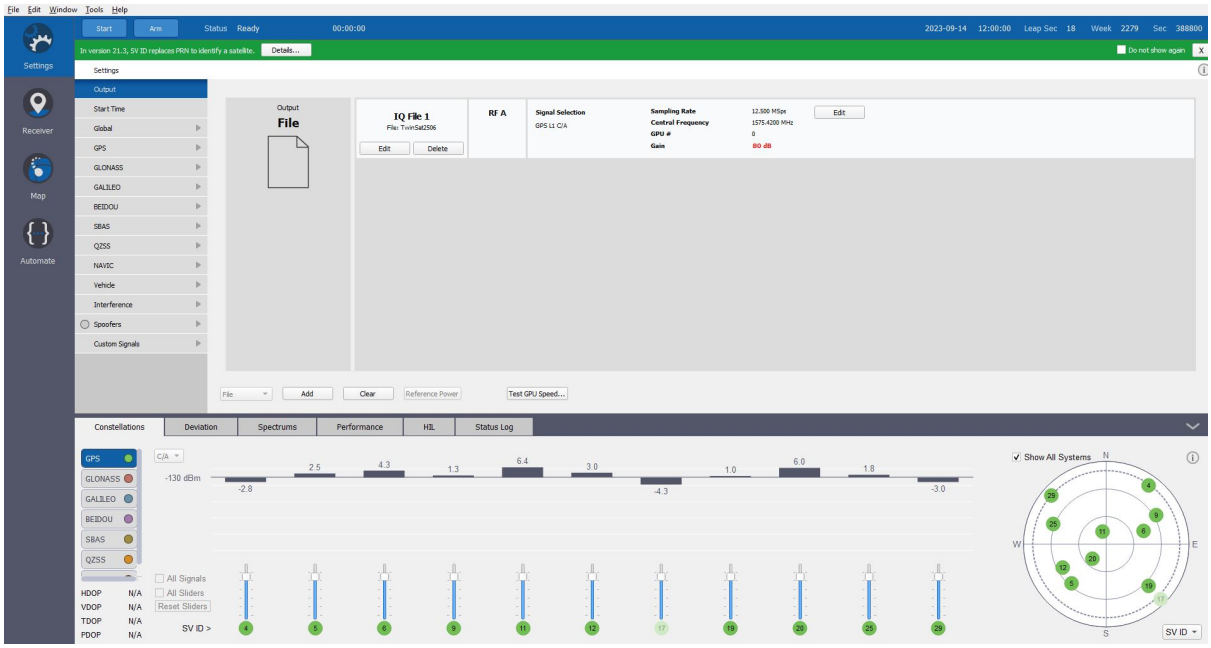

Fig. 5.2 Settings home page of Skydel showing the tabs and the "File" mode for the simulation.

data when launching a simulation. Figure 5.8 shows how to configure the file for the Track Playback mode.

In the Start Time tab, users can set the GPS time and determine the duration of the simulation. Ensuring control over the simulation start time is essential when evaluating GNSS receivers. Consistent start times across different test runs are often necessary to maintain identical GNSS satellite geometry for comparison purposes. GNSS receivers may reject locking onto a simulated signal if their internal clocks suggest an incorrect time, serving as a defense mechanism against spoofing. There are three methods available to manage the simulation's start time:

- Specify a custom time
- Use the computer system time
- Use the time from a timing receiver

The current Leap Seconds (LS) value and the date for the next leap second (LSF) can also be specified. The LS value helps the receiver convert GPS system time to UTC time, with NMEA data marked using UTC timestamps. If the receiver and simulator use different LS values to calculate UTC time, it can complicate the comparison of NMEA output, particularly in the receiver deviation graph.
During the simulation, the message *Streaming RF* will appear along with the elapsed time. Pressing the Stop button will halt the simulation, while the Pause button will slow the vehicle to a stop, though the simulator will continue to stream Radio Frequency (RF).
At the bottom of the settings tab, a sky view with power sliders is available, which can be adjusted as needed or reset to normal settings if necessary.

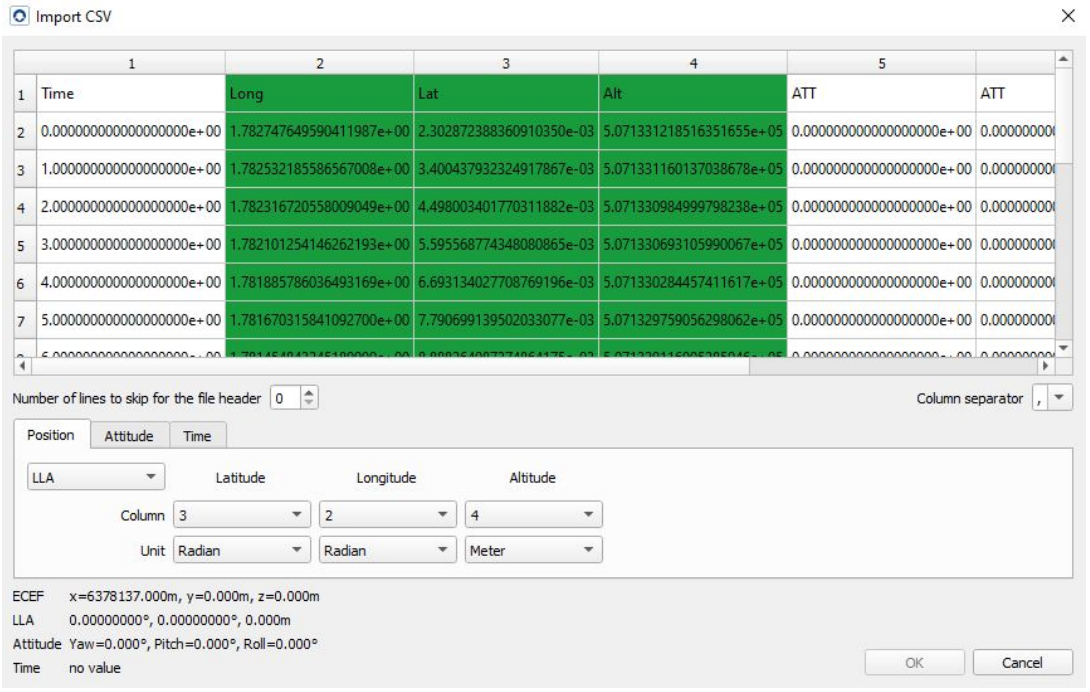

(a) Track Playback option to test spaceborne receivers.

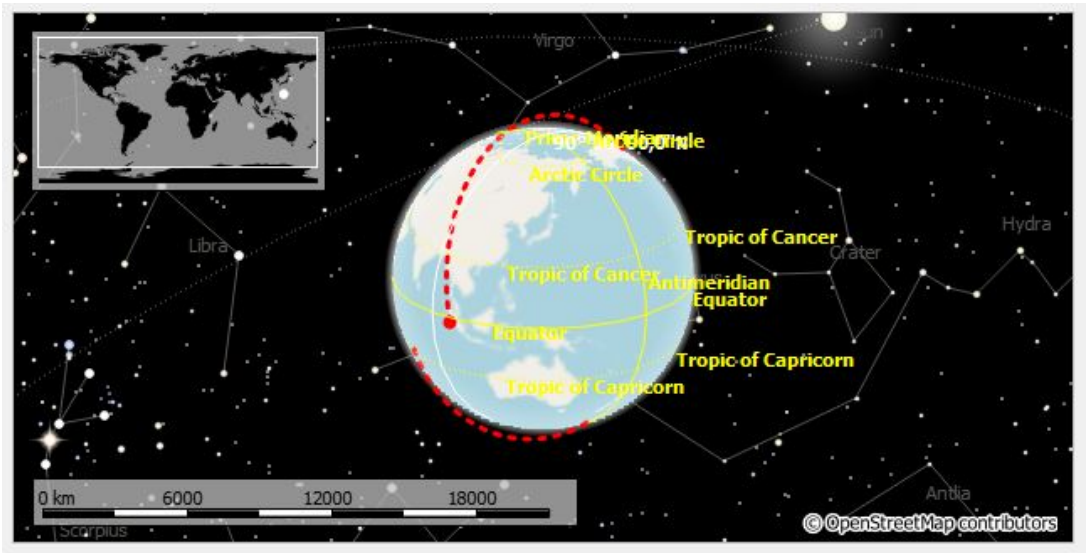

(b) Track reproduced from the .csv file generated to be used for the simulation.

Fig. 5.3 Track Playback mode Settings

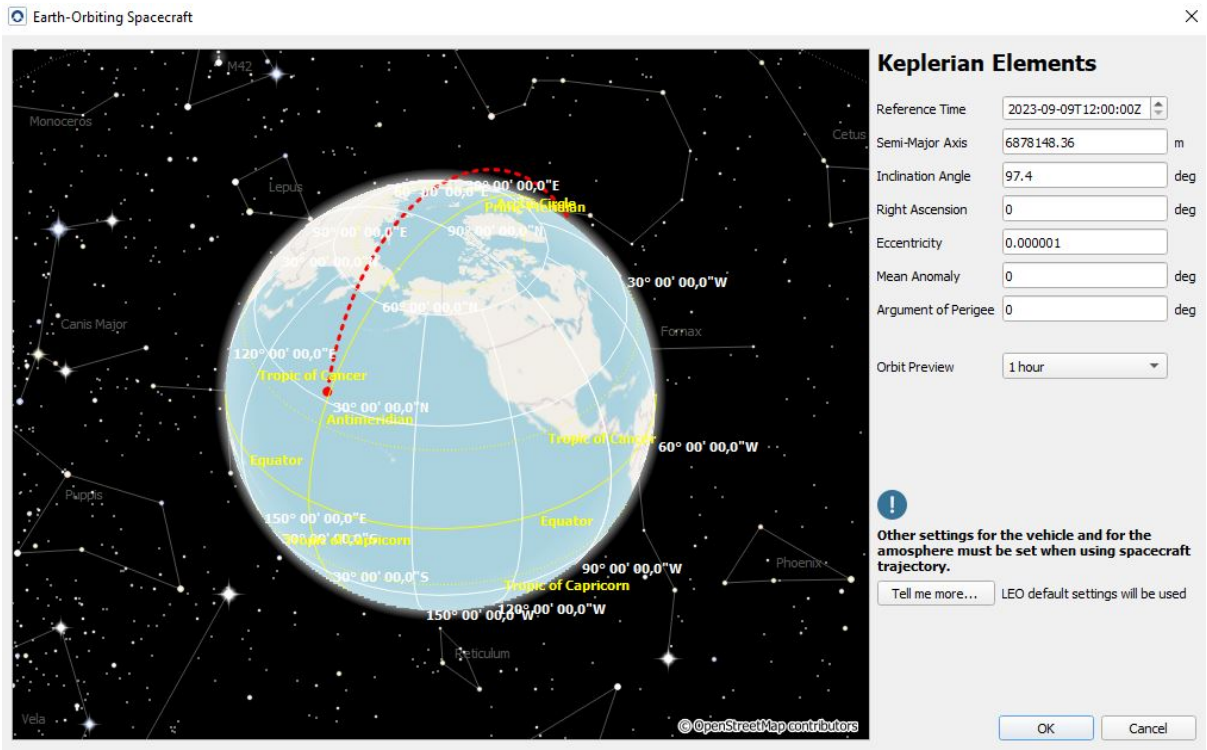

Fig. 5.4 Earth-Orbiting Spacecraft trajectories generation option to test spaceborne receivers.

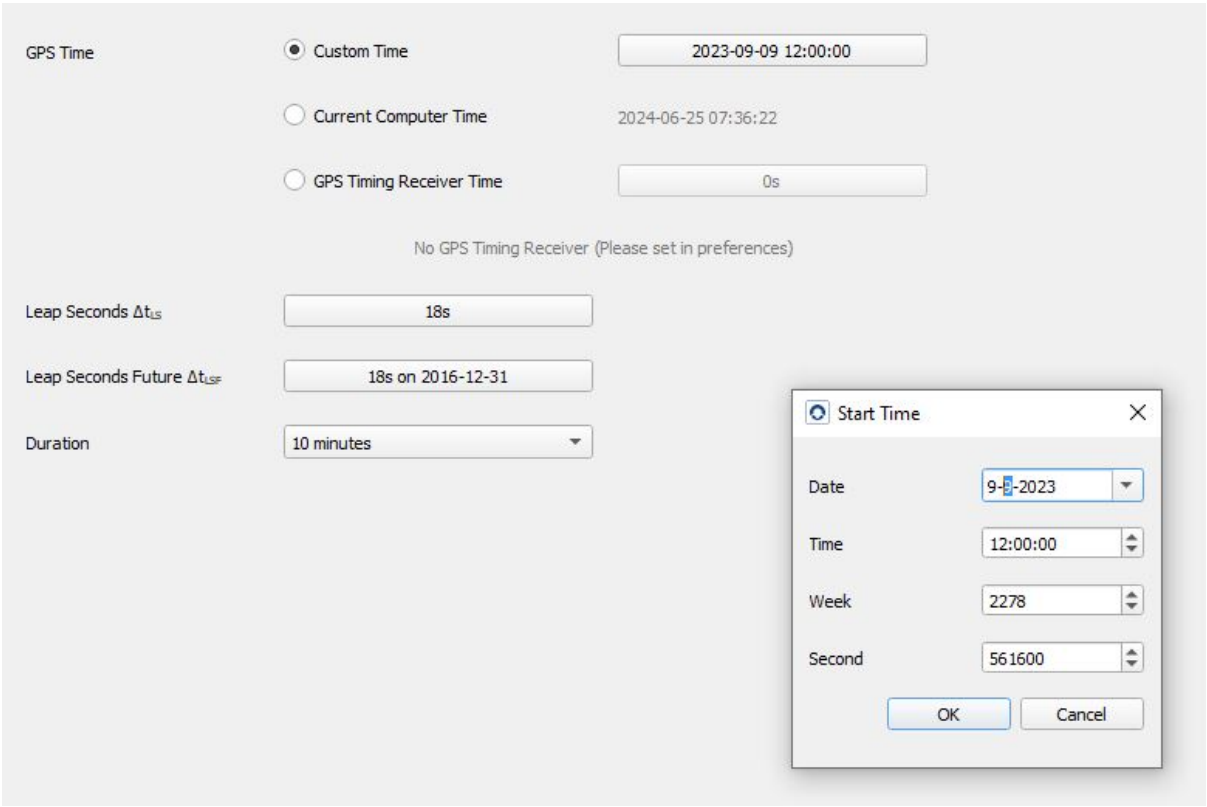

Fig. 5.5 Start Time Settings

When the simulation starts, Skydel begins saving data to the specified file. When saving data to IQ files, the GPU's performance does not need to pass the performance test. Skydel generates the file as quickly as possible, which can be faster or slower than real-time depending on the GPU and hard drive used.

IQ File Data

The IQ file uses the extension IQ and contains the raw 16-bit IQ samples in binary format. The file has no header. The first 2 bytes in the integer value for I, and the following 2 bytes are the integer value for Q. The pattern simply repeats I, Q, I, Q, etc. as depicted in figure 5.6

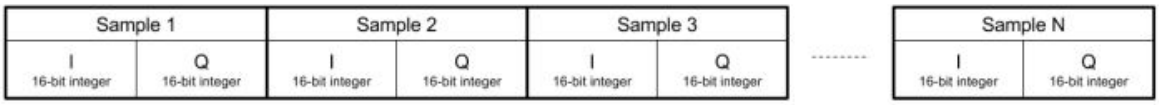

Fig. 5.6 IQ File Data Format

This file uses the extension XML and is consistent with the GNSS SDR Metadata Standard. It contains multiple fields describing how the IQ file should be read including the sampling rate and center frequency of the signal.

Simulation Output Type

A proper setup of the output settings is a key component of a successful simulation. There are several options:

- Anechoic Chamber. It uses up to 16 X300 SDRs to transmit GNSS and jamming signals inside an anechoic chamber.
- DTA-2115B.
- DTA-2116.
- File. The IQ data is saved to a file on the computer's hard drive.
- None. RF is not generated and IQ is not saved, but raw logging data is saved instead.
- NoneRT. Similar to None but runs in real time.
- X300.

The Signal Selection dialog box allows users to choose the signals to be generated for each output. This selection will update the ideal sampling rate and disable any code types

incompatible with the current selection.
After finalizing the signal selection, the GPU's performance can be tested. A score below 1.00 indicates that the GPU lacks the performance necessary to generate the signals in real-time.

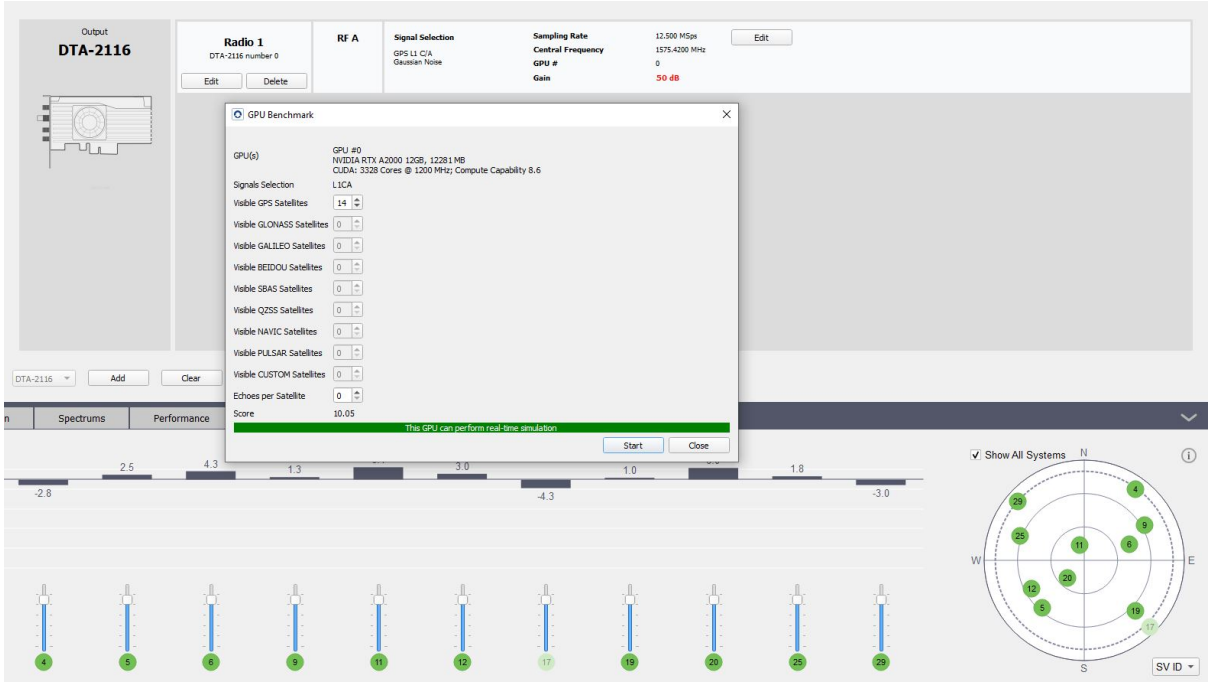

Fig. 5.7 Signal Selection window.

The simulation made in this work was made using in a first the File mode, retrieving the IQ data, and later the DTA-2116, for real-time outputs and overall faster and more efficient solutions.

5.2.2 Hardware Set-up

Since a software-only version of Skydel was purchased, it is necessary to give an introduction to the Software-Defined Radio and all the required RF accessories.

Software-Defined Radio

The choice of the SDR depends on the simulation requirements, considering characteristics such as central frequency range, output power level, community support, etc. The radio used for the purpose is the Dektec DTA-2116.

Initial simulations were also made by using another old radio less precise and adaptable to the software used. This was the USRP B200 software-defined radio developed by Ettus, with a platform containing a frequency coverage from 70MHz - 6GHz.

RF Accessories

Other RF accessories are required to connect the SDR to the GNSS receiver, such as:

- **Attenuators**. The RF signal power level output by the SDR is much stronger than the real live sky signal when it reaches the GNSS receiver's antenna. Consequently, Safran strongly recommends using attenuators between the SDR and the GNSS receiver to avoid damaging the GNSS receiver.
- **DC-Block**. The DC-Block is a single component that prevents the DC voltage from traveling back from the GNSS receiver to the SDR. Typically, GNSS receivers will provide DC voltage (5V or 12V) to the antenna in order to power the antenna's amplifier. However, when using a simulator, this DC voltage is useless and could damage the SDR.

GNSS Receiver

The SkyTraq PX1122C GNSS Receiver, a dual-frequency (GPS L1/L2C) receiver, is installed. It is an Real Time Kinematics (RTK) receiver designed to achieve centimeter-level accuracy for precision guidance and relative positioning applications [3]. This receiver is capable of providing raw measurements for performing carrier phase RTK processing.

5.2.3 Simulation Process

The process followed to run simulations is now described:

1. *Generation of the track file*. A CSV file is generated from the dynamical propagation of the scenario, for a period of one orbit and inserted into the Skydel software.
2. (a) *Skydel Software on File mode*. The simulation is launched and IQ data are saved to be processed in a second step.
   (b) *Skydel Software on DTA-2116 mode*. The simulation is launched and the NMEA file is generated real time in one single step.
3. *Generation of the NMEA file*. To visualize the data while monitoring the Skytrack receivers in real-time, NAvSpark GNSS Viewer software is used. This software displays the NMEA standard messages to be saved and further processed/filtered.

   The viewer displays all the useful information saved on the NMEA file:

   - Positioning data: Date, Time, Latitude, Longitude, Ellipsoidal Height, Direction, Speed, Horizontal Dilution of Position (HPOP).
   - The number of satellites in view and the quality of the signal in terms of Signal-to-Noise Ratio (SNR).

(a) SkyTraq PX1122C GNSS Receiver installed on its board (c).

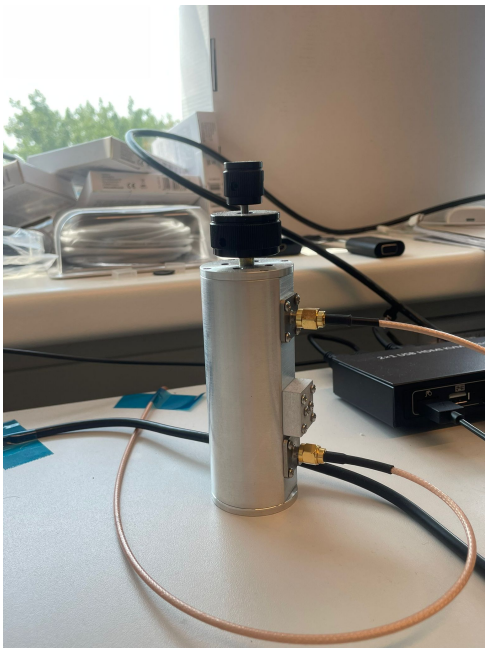

(b) Decktec DTA-2116. Software-Defined Radio mounted on its board (c).

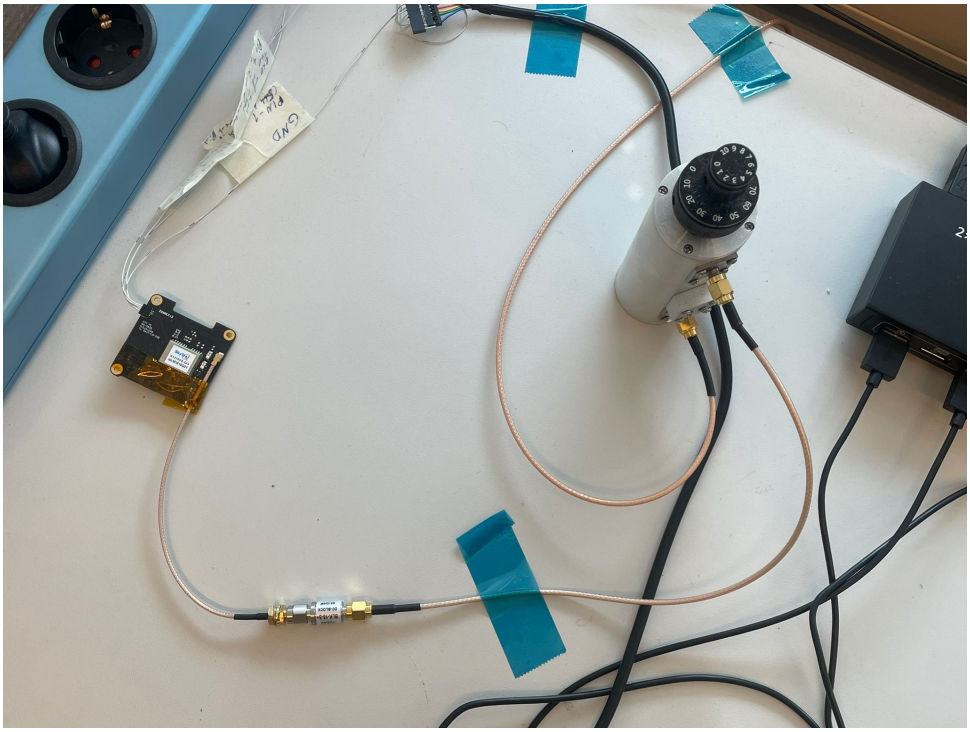

(c) Harware setup mounted with its receiver, radio, and DC-Block.

Fig. 5.8 Track Playback mode Settings

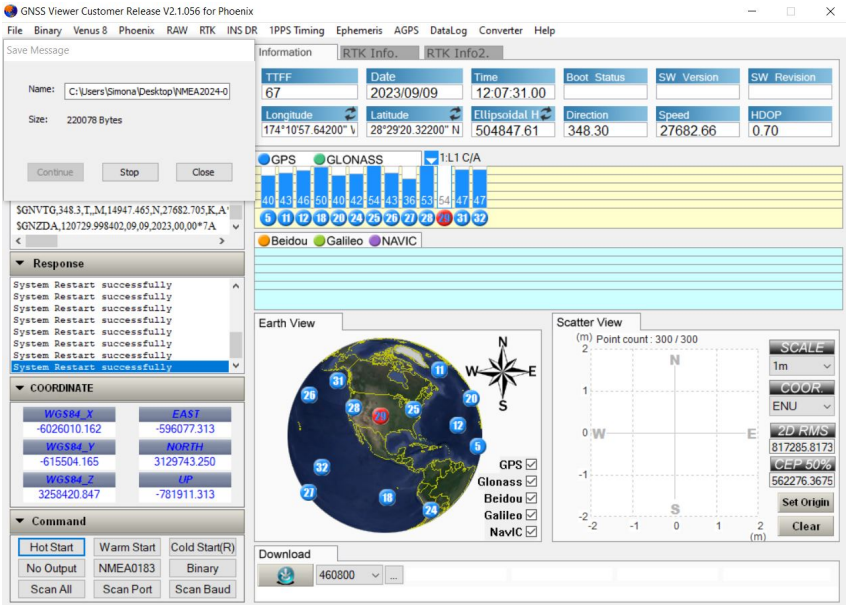

Fig. 5.9 GNSS Viewer Software interface and real-time downloads of the NMEA message.

- Time to First Fix (TTFF) and accuracy of the position fix.

As mentioned before, the open-source GPS-SDR-SIM software was used for this type of simulation, before a real-time radio was available. On the GNU Radio Command Prompt, the following file is launched for the National Aeronautics and Space Administration (NMEA) message to be generated: **gps-sdr-sim-uhd.py**.
When launching the new set-up using the DTA-2116 mode, a map is available showing the simulator moving across the Earth in real-time during the simulation, which also comprehend an interface that is much more user-friendly.

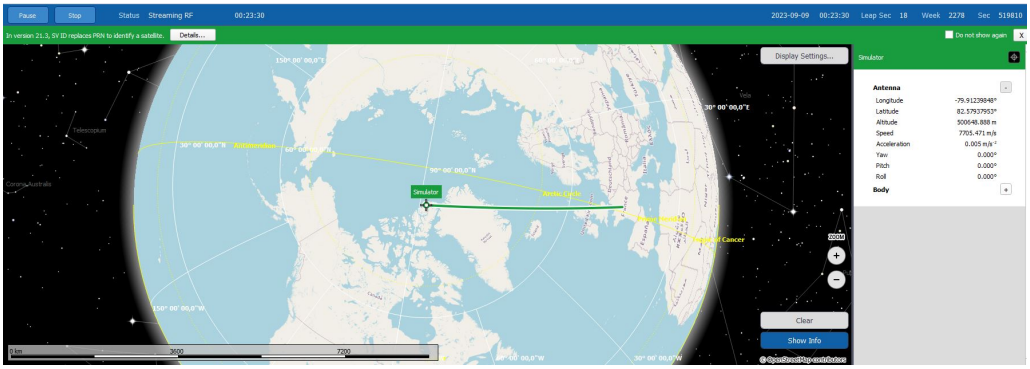

Fig. 5.10 Map tab showing the simulator in real-time during the Streaming RF.

After running the simulation the NMEA message is saved and needs to be processed and filtered, in a few steps:

1. The locked raw of the NMEA message is filtered and the useful raws are translated into a file containing Latitude Longitude Altitude (LLA) state at the specific time.

2. The LLA state is converted into ECEF coordinates using the World Geodetic System (WGS). being this the WGS84, then ECI coordinates using the correct rotational model of the Earth.

3. ECI coordinates are converted to RSW coordinates to have a better insight into each component and the actual motion.

Each of these conversions is used and compared to the actual real data from the propagation of the satellite, which is also the same model used to import the track into Skydel to run the simulation.

5.2.4 Simulation Results

The NMEA file is filtered removing all the unnecessary data saving just the strings containing locked receiver data. The output file contains strings of Time, Longitude, Latitude, and Altitude. A final simulation was performed for a duration of 1 hour (any duration limit concerns directly the hardware available for the simulations). Figure 5.16 shows the overlapping of the ground tracks (real vs the simulated one) constructed from the LLA real state versus the observed status.

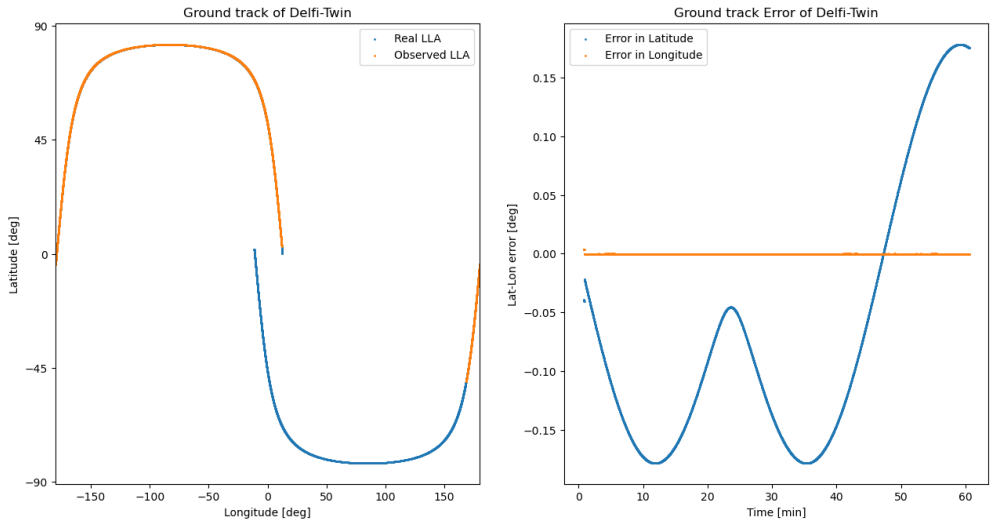

Fig. 5.11 GroundTrack of the satellite: real and observed data. GroundTrack errors over time for a simulation of 1 hour.

Any discrepancy in altitude is due to the different reference types used: Tudat refers to geodetic altitude, while Skydel provides geographic coordinates. The ECEF real state is imported into Skydel, and the simulation runs with the given track, showing relatively low error in both the ECEF and ECI reference frames. The overall error is on the order of tens of meters. As expected, the lowest error is observed along the Y axis, both in the ECEF and ECI frames, with

a maximum error of less than 7 meters, while other components show errors up to almost 60 meters.

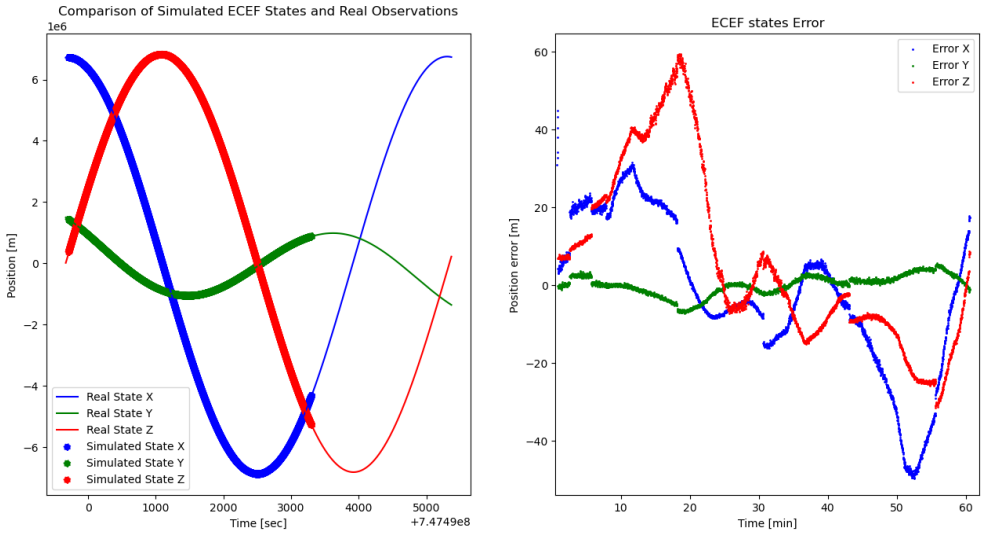

Fig. 5.12 ECEF real status vs simulated status on the right. Position error over time for a simulation period of 1 hour.

To gain a better understanding of the output and identify which components were subject to the highest errors, the RSW state was plotted and compared. The second component, the cross-track component, proved to be more accurate. As expected, higher errors were observed in the radial and, most significantly, the along-track components. Consequently, the Keplerian parameters displayed very accurate values, except for the true anomaly and argument of perigee. The argument of perigee may also be affected by the low eccentricity of the constructed orbit.

Finally, the Keplerian parameters were reconstructed from the simulated orbit, allowing for comparison. The errors affecting the semi-major axis and eccentricity exhibit a reasonably consistent behavior, as does the RAAN. However, the error in inclination seems to stabilize at the equator and reaches its maximum at the poles. There are various reasons this could happen: GNSS simulators use mathematical models to emulate the propagation of satellite signals, which may have limitations or approximations that introduce more noise in the inclination at the poles; additionally, even in a Hardware-In-The-Loop (HIL) environment, the geometry of the simulated satellites can influence measurement accuracy.
Overall, the receiver appears to be quite accurate in calculating the satellite position. The sources of error may stem from the imprecise clock used and the antenna, which posed challenges during the setup and creation of the simulations.

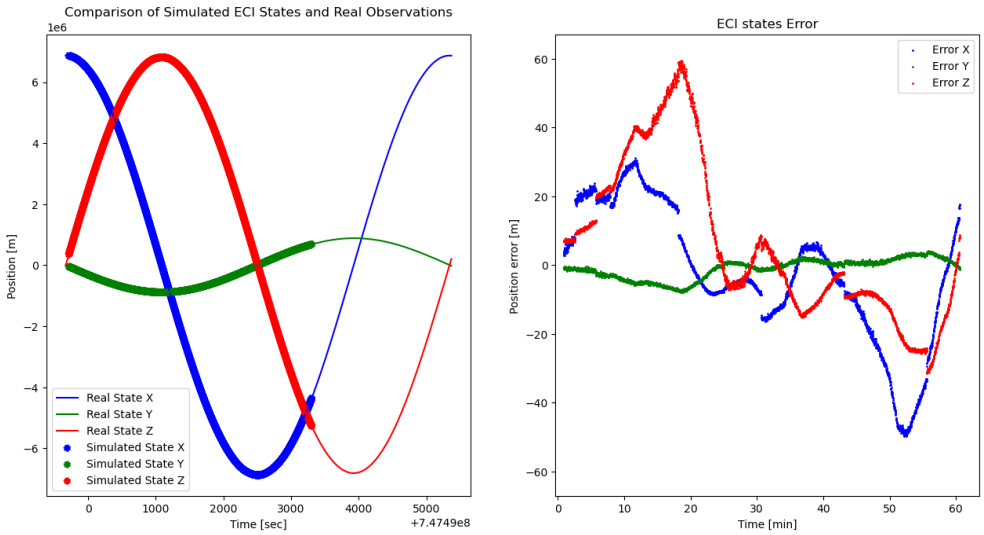

Fig. 5.13 ECI real status vs simulated status on the right. Position error over time for a simulation period of 1 hour.

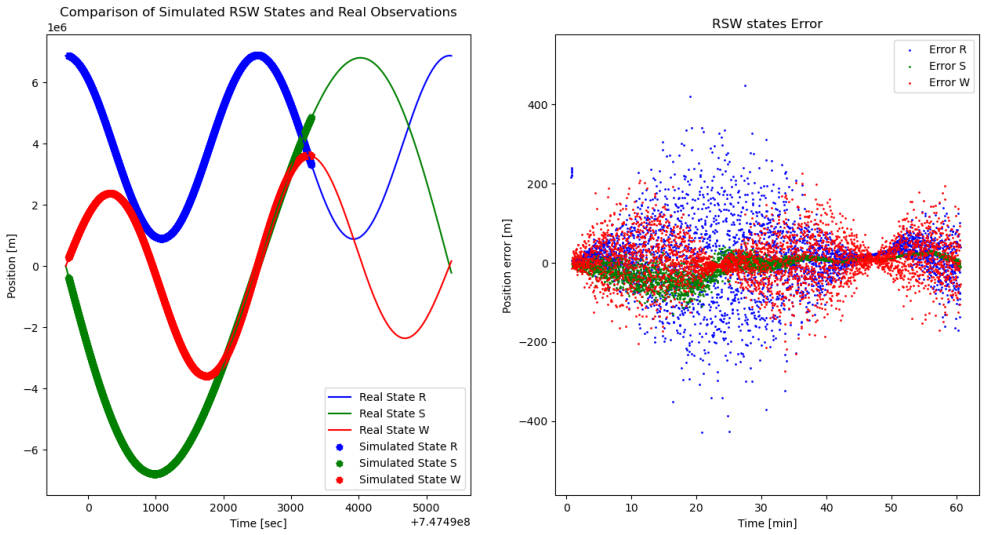

Fig. 5.14 RSW real status vs simulated status on the right. Position error over time for a simulation period of 1 hour.

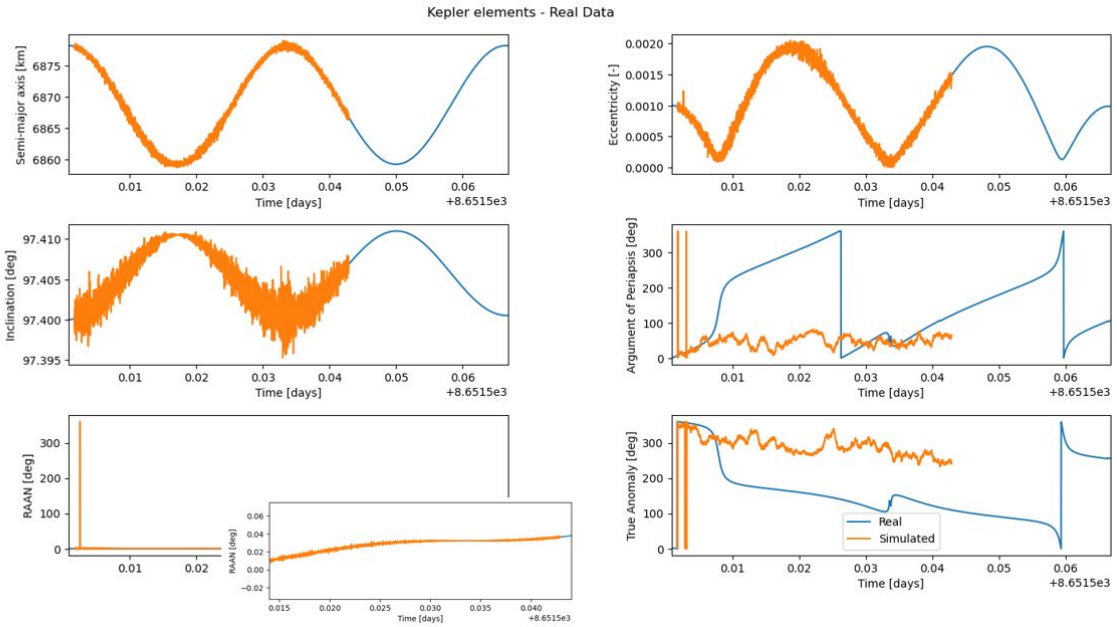

Fig. 5.15 Orbital parameters over time. Zoom into the RAAN to better see the overlapping of the real versus the simulated data.

5.3 Orbit Estimation

This paragraph outlines the steps to establish an orbit estimation routine, emphasizing the comprehensive estimation of a spacecraft's initial state during its orbital propagation, utilizing data from the TwinSat orbit itself.

To determine the orbit of a spacecraft and its associated constants and parameters is an application of estimation theory: a model is constructed based on initial conditions and dynamic parameters to predict the spacecraft's path in orbit. This process involves adjusting selected independent parameters until the computed measurements closely match actual observations. The solution is achieved by minimizing errors in the estimated parameters, aiming for convergence.

An essential metric for assessing orbit determination accuracy is the sum of squared differences between computed and actual measurements across all observations. This measure helps gauge how closely the model predictions align with real-world data, thereby refining the accuracy of orbital predictions and parameter estimates.

The track given to the simulation orbit is also generated in this part, to avoid modeling errors and differences in the simulation scenario. In fact, the problem of letting Skydel create the track is indeed the model that it uses to propagate the orbit. For that reason, the option used for the simulation was the generation of the track file directly from Tudat, as widely explained in the simulation process.

Again, the integrator used is the RKF78 with a fixed time step of 1 second.

5.3.1 Simulation Process

To define the observation model, the various bodies together with the spacecraft and whatever is necessary for the type of observation to perform, must be defined. After that, some Tudat packages can be used to perform the wanted analysis:

- *Link Ends and Observation Model Setup*. The link ends defined are set as the various reference points that are required, which in our case is the spacecraft orbiting with respect to the Earth. In this work, real data generated from the GNSS software will be loaded into Tudat and used inside the estimation to create the observation simulators and generate the computed observations from which the residuals are computed.
- *Observation Creation.* Simulating the observation requires a definition of the time at which the observation is to be simulated, as well as the definition of the model used.
- *Estimation Settings.* The full estimation performs an iterative differential correction of the estimated parameters until convergence is reached.
- *Performing Estimation*. The main results of the estimation are characterized by the residual vector of the iteration that had the lowest residual and the values of the parameters at the iteration that had the lowest residual as well.

5.3.2 Simulations Results

The iterations performed demonstrate a rapid decrease in residuals and quick convergence. Previous simulations exhibited errors in the modeling of observation data, as indicated by sinusoidal residual histories, which have since been corrected. As a result, the current distribution is more sparse and centered around zero, as also seen in the error plots of the positions across all reference frames studied (figure 5.11, figure 5.13, and figure 5.14).

Lastly, figure 5.17 shows a histogram with a Gaussian shape, indicating that the simulation was performed correctly. Ideally, a perfect Gaussian with zero mean would serve as proof of a valid estimation. To conclude, the orbit has been reconstructed with a final residual of less than 20 meters.

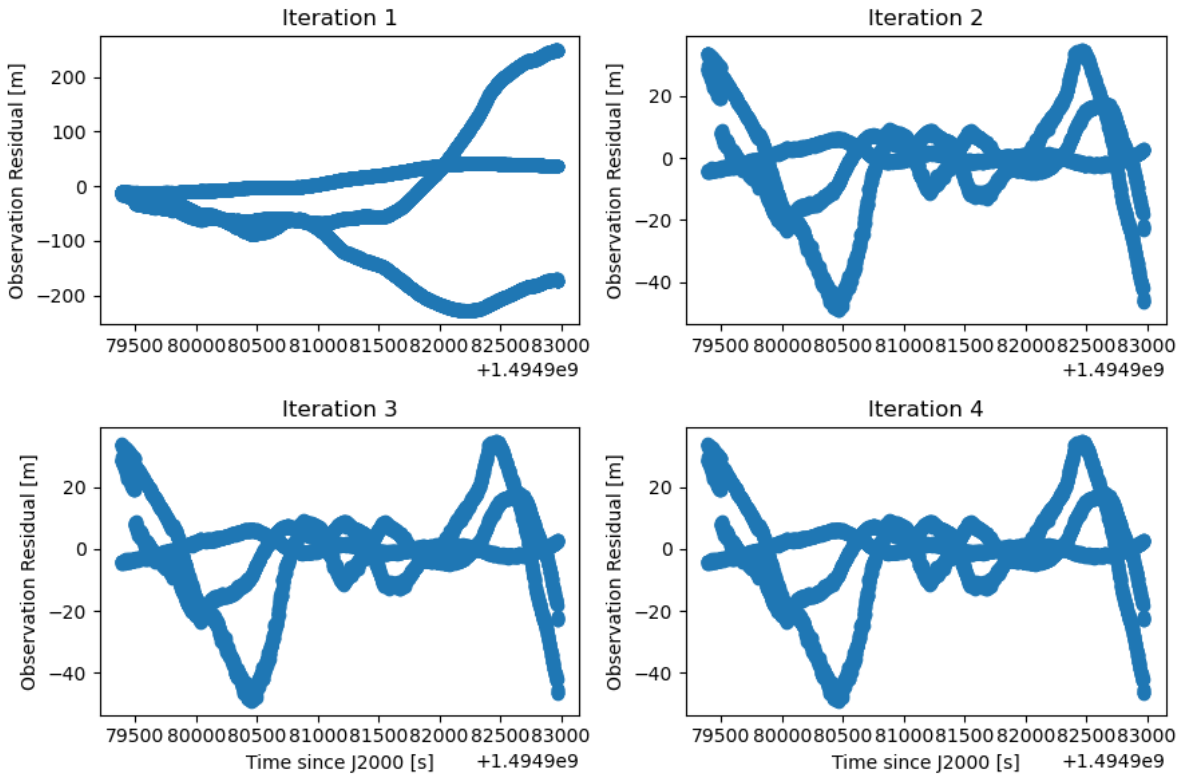

Fig. 5.16 Residual histories over 4 iterations.

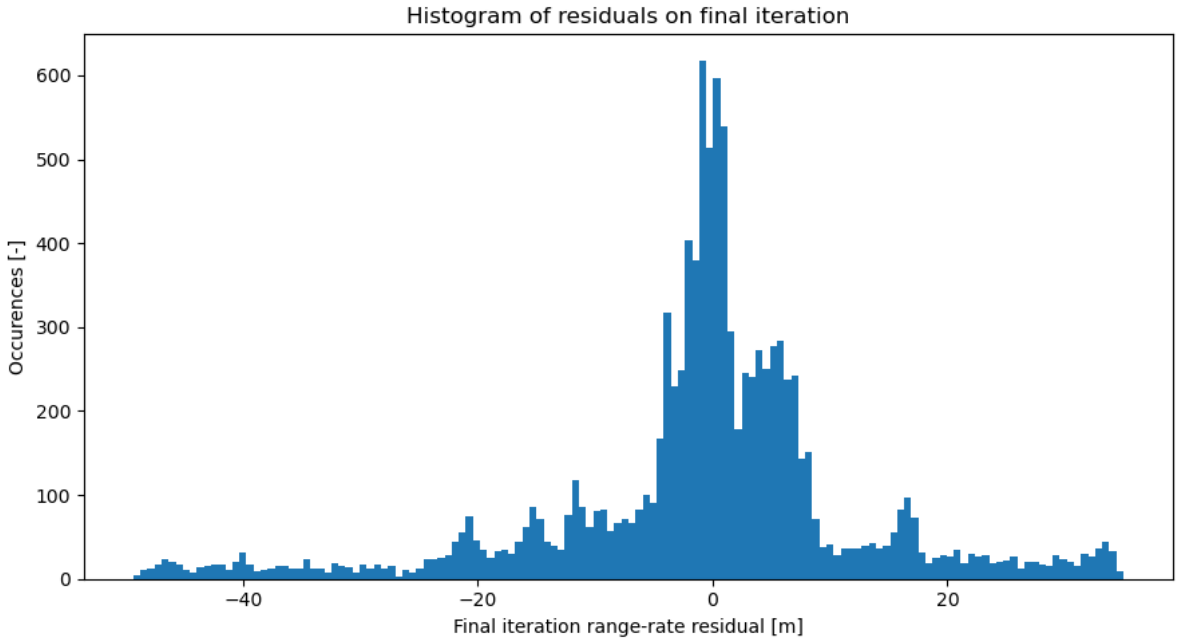

Fig. 5.17 Histogram of the residual history showing a Gaussian shape.

Chapter 6

Conclusions

In this chapter, a final overview is presented, including the key results of the research work. Additionally, ideas for future work and further improvements are discussed, serving as guidelines for the continuation of the Twin-Sat mission definition of the Delfi Project.

6.1 Conclusions and Future Work

In this thesis, a previously analyzed mission design was further developed, inspected, and elaborated on various aspects.

Particularly, the different mission phases were analyzed to both validate the provided mission requirements [3] and to define additional ones through further studies. The analyses considered the existence of two identical and independent 3P PocketQubes. These are launched as a single spacecraft and separated in orbit via a spring mechanism.
At this point, the separation phase was defined by revisiting the separation velocity requirements and direction of separation. The point of mission separation was subsequently decided. Despite ensuring safety for the FCA, the mission architecture that involved the conjunction of the satellites before reaching the maximum distance again was deemed risky. The final architecture includes a condition of minimum distance for performing subsequent control actions, leading to a reduction in satellite lifetime that is both acceptable and valid, thus exceeding two years.

An important part of this work involves analyzing the satellite's cross-section using ESA's DRAMA tool. Specifically, the variation of an orbital lifetime with changing cross-section in a high-drag configuration of the satellite was studied, as well as secondary but equally relevant aspects regarding the experienced acceleration and the relative velocity limit imposed in satellite control. Furthermore, specific configurations of the satellite were defined concerning the different multiplication factors relative to the high-drag configuration: a specific aperture angle of the solar panels was indeed defined. This differential acceleration is the basis of the satellites'

orbital control.
The analyses were conducted by defining a series of propagation sequences using TuDAT, the tool developed by TU Delft.

The second part of the thesis delves into the relative navigation of the two satellites. A comparison between the numerical method for satellite motion propagation and an analytical one was carried out. Specifically, an initial test was performed with the satellites at a fixed distance. The model was validated by considering the error in relative position calculation and the ROEs, using model data from analytical propagation and reference data from numerical calculation at different time step sizes. The model's accuracy was then studied by evaluating this error for a distance equal to the maximum distance traveled by the satellites, which will always maintain the defined distance for CPO. The results of these analyses suggest that, although processing time does not significantly impact the mission's purpose, the convenience of a model that directly provides relative parameters can be highly useful and reduce the required computational memory. Moreover, this will lead to further analysis of the strategy to use for the orbit reconstruction.

The final part of the thesis is experimental and deals with the use of GNSS simulation software to test the accuracy of navigation hardware. Several GNSS signal emulation analyses were conducted, and the process by which the comparison between simulation outputs and real data is made is defined. The final simulation carried out stated an acceptable low error in the calculation of the satellite motion and the Keplerian parameters were reconstructed, in order to have a better insight into the types of error. The final simulation provides an hour of data and very accurate results.
To conclude, a process for parameter estimation was developed: the residual history also helped find different sources of errors in the multiple simulations that were performed. In the end, the orbit reconstruction led to a residual lower than 20 meters and the Gaussian shape of the histogram of the residuals served as proof.

Just as this work built upon previous research related to the definition of the Twin-Sat mission, it will also serve as a reference point for future iterations. Many aspects have been thoroughly explored, and others will undoubtedly lead to further study phases, all aimed at the ultimate success of the mission.
Concerning the differential drag control, some interesting points to further study would be:

- The analysis of strategies for orbit maintenance using the orbital dynamics of the satellites.
- The implementation of the actual mechanism of solar panels used for the control and, subsequently, a study of the coupling of the mechanical system, with particular reference to control readiness and its effect in terms of collision avoidance.

- A focus on the attitude of the satellites, considering their modeling and, if necessary, implementing stabilization measures. This involves examining the satellite's attitude and the effects of drag on it.

Regarding the testing of the accuracy of the receiver, it would also be important to:

- Perform more simulations, all long at least one orbital period in order to analyze what's happening in all the different points within an orbit. Simulations using different orbital geometries, or different setups, will also help to go through what is the limit of the actual receiver.
- Further improve the orbit estimation strategy, to see whether the residual can still drop down.

References

[1] *NASA Systems Engineering Handbook*. NASA, 2020.

[2] ESA Space Debris Office. *ESA's Annual Space Environment Report*. 2023.

[3] C. Marianna. Mission and system design of a formation-flying picosatellites cluster: A technology demonstration mission for space situational awareness improvement. Master's thesis, Politecnico di Torino, Delft University of Technology, 2023.

[4] NASA. *State-of-the-Art - Small Spacecraft Technology*. Small Spacecraft Systems Virtual Institute, 2024.

[5] 65 authors from the Astronautic Community. *Space Mission Engineering - The New SMAD*. Microcosm Press, 2011.

[6] Alba Orbital, TU Delft, and Gauss Srl. The pocketqube standard, 2018. [Online] Accessed: Apr 6, 2024. Available at: https://www.albaorbital.com/pocketqube-standard.

[7] TU Delft. Delfi program. [Online] Accessed: Apr 6, 2024. Available at: https://www.tudelft.nl/lr/delfi-space/delfi-program.

[8] S. Radu, S. Uludag, S. Speretta, J. Bouwmeester, E. Gill, and N. Chronas Foteinakis. The first pocketqube of delft university of technology. In *Proceedings of 69th International Astronautical Congress: Bremen, Germany*, pages Article IAC–18–B4.6B.5. International Astronautical Federation, IAF, 2018.

[9] Marco D'Errico Editor. *Distributed Space Missions for Earth System Monitoring*. Springer, Microcosm, Inc., El Segundo, CA, 2013.

[10] ESA. Proba missions. [Online] Accessed: Apr 7, 2024. Available at: https://www.esa.int/Enabling_Support/Space_Engineering_Technology/Proba_Missions.

[11] Gill E. Persson S., Jacobsson B. Prisma - demonstration mission for advanced rendevous and formation flying technologies and sensors. 2005. Swedish Space Corporation, Sweden; German Aerospace Center (DLR), Germany.

[12] Hajiyev C. Erkec T. Y. The methods of relative navigation of satellites formation flight. In *Int. J. Sustainable Aviation*, pages Vol. 6, No. 4, pp.260–279, 2020.

[13] Laura Rocchio. Peering homeward, 1972. [Online] Accessed: Apr 8, 2024. Available at: https://explorer1.jpl.nasa.gov/stories/laura-rocchio/.

[14] TU Delft. Tudat space. [Online] Accessed: May 6th, 2024. Available at: https://docs.tudat.space/en/latest/.

[15] ESA Space Debris Office. *DRAMA - Final Report. Upgrade of ESA's Space Debris Mitigation Analysis Tool Suite*. 2014.

[16] Yu Nakajima Colombo C. Capuano V. Saggiomo F. Leccese G. Natalucci S. Borelli G., Gaias G. Mission analysis and guidance and control for the speye inspection cubesat. 2024.

[17] Peng Li Yansong Meng Jun Xie, Haihong Wang. *Satellite Navigation Systems and Technologies*. 2021.

[18] George H. Born Bob Schutz, Byron Tapley. *Statistical Orbit Determination*. 2010.

[19] Safran. *Skydel, Software-Defined GNSS Simulator. User Maanual*. 2023. [Online] Available at: https://safran-navigation-timing.com/document/user-manual-skydel-software-defined-gnss-simulator/.